TECHNISCHE UNIVERSITÄT MÜNCHEN

Fakultät für Elektrotechnik und Informationstechnik

Lehrstuhl für Biologische Bildgebung

Assessment of hybrid FMT-XCT for respiratory and cardiovascular small animal imaging applications

Xiaopeng Ma

Vollständiger Abdruck der von der Fakultät für Elektrotechnik und Informationstechnik der Technischen Universität München zur Erlangung des akademischen Grades eines

Doktor-Ingenieurs

genehmigten Dissertation.

Vorsitzender: Prof. Dr. Marc Tornow

Prüfer der Dissertation:

1. Prof. Vasilis Ntziachristos, Ph.D.

2. Prof. Dr. Bernhard Wolfrum

3. Priv.-Doz. Dr. Moritz G. F. Wildgruber

Die Dissertation wurde am 20.06.2016 bei der Technischen Universität München eingereicht und durch die Fakultät für Elektrotechnik und Informationstechnik am 30.12.2016 angenommen.

Abstract

Respiratory diseases are important cause of illness and death all over the world. Asthma and lung cancer are two important respiratory diseases. Cardiovascular disease (CVD) is a leading cause of mortality and morbidity in developed countries. Atherosclerosis is the usual cause of CVD. More and more attention has been drawn to studies related to respiratory diseases and different cardiovascular pathologies with optical imaging method. Optical imaging has many advantages over other molecular imaging modalities; these are being cost-efficient, free of ionizing radiation and multiplexing.

Traditional standalone fluorescence molecular tomography (FMT) imaging suffers from ill-posedness during the reconstruction due to scattering of light in living tissue. By incorporating anatomical information from X-ray computed tomography (XCT) , the hybrid FMT-XCT system not only provides anatomical/molecular merged information, which helps analyzing the biological process, in addition the incorporated priori anatomical information also improves the accuracy of FMT inversion. This work focus on the investigation of the potential of FMT-XCT imaging modality in the quantification and detection of three representative respiratory and cardiovascular diseases: asthma, atherosclerosis and non-small cell lung cancer (NSCLC).

The three different biological diseases happen in the thorax region, which contains three important organs apart from muscle: bones, the heart, and the lungs. The lungs account for largest part of this region. The first longitudinal biological study was a quantitative evaluation of asthma related inflammation and remodeling. With DRA-challenged (dust mites, ragweed, and aspergillus species) mice as the mouse model,

three different time points or groups were chosen for imaging comparison: these are six weeks of DRA exposure, nine weeks of exposure, and nine weeks of exposure followed by three weeks of rest. Two fluorescence imaging agents: Prosense680 and MMPSense680 were applied during the experiments: Prosense680 for first and second time point, MMPSense680 for third time point. Reconstruction results from FMT-XCT for these three times showed that FMT-XCT could resolve elevated fluorescence intensity and MMP expression elevation. Biological H&E staining of mice also further confirmed the asthmatic inflammation and remodeling characteristics for this mouse model.

Second application focused on the atherosclerosis mouse model. The hybrid FMT-XCT system was used to visualize quantification of neutrophils, which accumulate in the plaques of an atherosclerotic aortic arch region. Fluorescence agent, Neutrophil Elastase 680 FAST, was used to track neutrophils activity at the early stages of atherosclerosis. Quantification results of FMT-XCT were compared with *ex vivo* cryoslicing findings, which also demonstrated that the hybrid system could resolve neutrophils accumulation. Since the fluorescence signal from the interested region aortic arch was low, an optimized reconstruction method was developed by setting one untargeted wavelength as a background reference, the targeted wavelength reconstruction results were subtracted proportionally from this reference signal. The phantom experiments and the atherosclerosis mouse model proved that this optimized background subtraction method could improve the accuracy and quality of FMT-XCT reconstruction.

The last application was performed by using a NSCLC mouse model. Four study groups were set up with distinct purposes: the first group was a baseline imaging group, with no treatment of the LLC mouse, to monitor the growth rate of this cancer model; the second group was treated with the integrin inhibitor cilengitide to test the sensitivity of IntegriSense 680; the third and fourth groups were each treated with a chemotherapy medicine separately (one with the anti-angiogenesis compound Avastin, and one with an MEK-inhibitor). Every mouse in each group was FMT-XCT-imaged at three different time points: before initial treatment, after three days of treatment, and after either six days or one week of medication. Comparisons of each group demonstrated the same result: that the FMT-XCT imaging was a useful tool for tracking tumor growth and monitoring medication therapy efficacy.

FMT-XCT quantification results of every mouse in all applications were compared against gold-standard cryoslicing results, and exhibited pronounced consistency between the *in vivo* findings and the *ex vivo* validations. Some of the quantification

results were also confirmed by biological staining. Statistical analysis of FMT-XCT also presented the quantification capability of the hybrid imaging system. All these findings enhance the role of FMT-XCT in preclinical study of cardiovascular and respiratory diseases.

Contents

1 Introduction

1.1 Pre-clinical noninvasive imaging modalities

Noninvasive *in vivo* imaging of small animals is a widely used tool for current preclinical molecular imaging research. The aim of noninvasive imaging is to visualize the expression and/or activity ofspecific molecules in corresponding biological processes, and, therefore, to provide a longitudinal method to monitor the distribution of these molecules *in vivo* [1-4]. Noninvasive imaging has several applications: early disease detection, diagnosis, and for monitoring therapy or treatment. Many new imaging modalities or technologies have been constantly developed to address these aspects. In principle, different noninvasive imaging techniques work similarly: each provides anatomical or functional information based on the interaction between molecules inside a living body and different energy particles, like X-rays, photons, sounds, or positrons [5]. Standalone small animal imaging systems can be classified into two main strategies of development [6]. The first strategy is transforming clinical imaging modalities into small animal imaging, such as X-ray computed tomography (XCT), positron emission tomography (PET), magnetic resonance imaging (MRI), ultrasound (US), or single-photon emission computed tomography (SPECT). The second strategy is developing new imaging modalities, like bioluminescence tomography (BLT), fluorescence molecular tomography (FMT), or optoacoustic imaging [6].

Anatomical techniques (e.g., XCT, MRI, and US) mainly provide morphological/structural information about a specimen with a high spatial resolution. X-ray computed tomography involves shining the X-rays on the body and detecting

the attenuated X-rays on the other side. The detected X-rays are used to reconstruct the attenuation of X-rays by different biological materials. Hundreds of projections are collected by rotating the scanning source and detectors of the device for a later three-dimensional reconstruction to visualize the density distribution of tissues. For an *in vivo* study, a small-animal CT (or Micro-CT) is used to investigate different diseases in a mouse model having high spatial resolution of the order of 0.05-0.2mm [7-9]. Fast acquisition time, depth of penetration, and cost-effectiveness are attractive features of Micro CT. One of the limitations of Micro CT is the low contrast between different soft tissues when compared with an MRI image. Therefore iodinated agents, or other CT contrast agents, are employed to increase the contrast [10]. Another limitation of Micro-CT is that it cannot detect diseases until tissue structural changes are large enough [2]. A third drawback of Micro-CT is the ionizing radiation dosage placed on the small animals prohibiting longitudinal studies.

Magnetic resonance imaging (MRI) technology on the other hand works in the radio frequency (RF) region of electromagnetic (EM) spectra. First, the machine creates a uniform magnetic field surrounding the specimen; this magnetic field can align magnetic dipoles/protons —for example, hydrogen atoms in water —within the body. Secondly, the RF coils in the device emits specific radiofrequency (RF) pulses to excite the nuclear alignment. Relaxation of the protons to their baseline orientation produces radio waves, which are recorded and translated into an MRI image depending on the proton density and tissue relaxation times [10, 11]. Three obvious advantages of MRI over other imaging techniques include: MRI creates excellent high resolution spatial information, MRI does not use ionizing radiation, and it has the ability to provide anatomical and functional information [12]. Using specialized MRI pulse sequences, one can obtain physiological or functional information; for example, diffusion-weighted (DW) MRI can improve lesion detection in oncological studies [13]. One main limitation of MRI —apart from its high cost —is its poor sensitivity with other molecular imaging techniques; however, many models of disease research still widely use MRI [14].

Ultrasound (US) molecular imaging uses a transducer to send out high-frequency sound waves. These waves then propagate through tissue, scatter tissue, or reflect tissue components. The transducer detects reflected sound waves and converts them into electrical signals, which are utilized to form an image according to the intensity and time delay of the received waves [15]. Traditionally, US modality has been used as an anatomical imaging technique. Contrast agents, called microbubbles (which are gas-filled liquid emulsions), are used to enhance contrast of the blood, because microbubbles do not leave the vascular area [16]. By targeting certain markers to the

microbubble agents, like antibodies, US can image angiogenic processes or inflammation. Tardy et al. discovered that vascular endothelial growth factor receptor 2 (VEGFR2) targeted microbubbles were useful for imaging prostate cancer in rats [11, 17, 18]. The strengths of US include its cost-effectiveness, absence of ionizing radiation, and satisfactory temporal resolution [12]. Ultrasound molecular imaging still has limitations: it requires coupling gel, and high US frequency waves can damage microbubbles [19].

Positron emission tomography (PET) imaging begins with injecting short-lived radionuclides—called imaging agents, like ^{18}F-FDG (fluodeoxyglucose)—into small animals. The radionuclides decay and emit positrons, these positrons will annihilate with electrons in surrounding tissues. This annihilation action produces two gamma rays of 511 keV that are emitted in 180°. A closed ring of detectors surrounds the test subject to record the gamma rays, and this is converted to electrical signals for further processing on a computer. Then, a three-dimensional reconstruction of these radionuclides' distribution can be displayed for diagnosis [20]. Positron emission tomography imaging plays an important role in clinical diagnosis, especially for cancer staging [21]. A miniaturized PET imaging scanner also has been used for investigating the mechanisms of many different disease models with a spatial resolution of 1-2 mm [22-25].

Like PET imaging modality, single-photon emission computed tomography (SPECT) is another nuclear medicine based approach, but with a different basic principle. SPECT employs distinctive nuclides or tracers, like ^{99m}Tc and ^{123}I, which decay by emitting only one single gamma ray with different energies. The imaging process resembles PET because it introduces a radioisotope into the test human or animal. The hardware for a SPECT scan also differs from PET by utilizing a gamma camera that rotates around the specimen and captures gamma rays from various positions. Lead or tungsten collimators are placed in front of the gamma camera to exclude useless photons [26, 27]. Small-animal SPECT is also available for *in vivo* research in many biological areas [28-31]. Both PET and SPECT modalities can provide physiological information with a high sensitivity and a limitless penetration depth. Apart from cost-effectiveness of SPECT compared to PET, another advantage of SPECT is in its multiplexing capability, which can track or image different bio-molecular targets simultaneously. The reason behind this is that PET records two gamma rays with precisely the same energy (511 keV), while SPECT is able to image gamma rays with diverse energies [12]. Both standalone radionuclide imaging modalities have two disadvantages: they use ionizing radiation, and they are incapable of offering an anatomical reference frame in tomography [32].

Optical imaging refers to technologies that rely on photon-tissue interactions and physical phenomena to generate images revealing physiological information about tissues. The next section presents a more detailed discussion.

The information garnered from these imaging modalities also divides them into two categories: anatomical/ morphological and molecular/ functional [2]. For example, XCT, US, and MRI primarily offer anatomical information, and PET, SPECT, or optical imaging mainly presents molecular information. Multimodal imaging systems aim to integrate these two techniques in order to examine structure and function simultaneously without any specimen movement. The most famous hybrid strategy is to integrate one of the radionuclide imaging modalities with CT, which is known as PET/CT or SPECT/CT [33-35]. Except their wide clinical use, novel preclinical PET/CT or SPECT/CT imaging demonstrates the enormous opportunities available for researching small animal models for human diseases or therapy monitoring [36-40]. Recent advancements in integrating MRI with PET or SPECT offers better image contrast among soft tissues and functional imaging [41-43]. Other hybrid molecular imaging technologies to measure multiple molecular targets simultaneously exist, including optical/PET [44], optical/SPECT [45], optical/MRI [46], and even tri modalities design for small animal research [47, 48].

Optoacoustic (OA) imaging is new emerging hybrid technique that combines the advantages of both optical imaging and acoustic imaging, and is based on optoacoustic effects. Short-pulsed laser beams are delivered into biological tissue, the tissue absorbs the laser energy, and will result in local thermal expansion. Differential absorption of the laser energy results in varied thermal expansion, and generates ultrasound waves. The system employs arrays of ultrasound transducers to capture the waves, which are later utilized to reconstruct absorption coefficient distribution of the tissue under investigation. Optoacoustic imaging has the ability to provide optical contrast at ultrasonic resolution [49-51]. Noninvasive OA imaging plays an important role in biological cancer research and many other aspects [49, 50].

1.2 Noninvasive optical imaging and fluorescence imaging

Optical *in vivo* imaging is based on the interaction between photons and tissues, and involves two main physical characteristics: absorption, in which a photon's energy transfers into the tissue's internal energy, and scattering, wherein light is diverted

from its path. The difference between scattering and absorption is its effect on light energy: scattering only changes the direction of propagation and does not alter light energy, but absorption reduces light energy (which is required for imaging) [52-54]. Since absorption is wavelength-dependent, selecting one wavelength window with the least tissue absorption is the only way to overcome the loss of signal intensity involved. Usually, blood contains oxygenated hemoglobin and deoxygenated hemoglobin, and water within the tissue dominates light absorption. Fortunately, the whole optical spectrum contains a window — called the "optical window"—where the absorption properties of blood is much higher compared to that of water and hence is suitable for *in vivo* optical imaging [6, 55], as shown in Figure 1.1. The approximate wavelength of this window spans from 650 nm to 900 nm, and is called the near-infrared (NIR) window. Another important characteristic of this NIR window is that, within it, tissue scattering is almost stable and much stronger than the absorption [55].
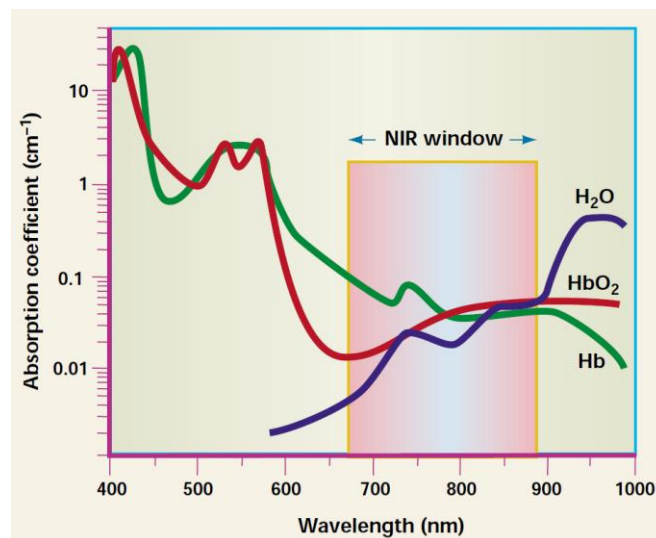
Figure 1.1. Near-infrared (NIR) window in tissue (Figure reproduced from [56]).

Optical imaging within the NIR window can be classified into two types: non-fluorescence-based imaging and fluorescence-based imaging [5]. There are three main non-fluorescence-based imaging technologies: bioluminescence imaging, optical coherence tomography (OCT), and photoacoustic imaging. Bioluminescence imaging relies on the enzymatic oxidation reaction of luciferase with the corresponding luminogenic substrate [12]. Different types of luciferase enzymes are introduced through the transfection of genes. These enzymes produce light, which then interacts with the injected substrate [57]. The photons emitted travel through tissue, and are captured by a high sensitivity charge coupled device (CCD) camera for generate luminescence distribution. One of the most widely used bioluminescence imaging

enzymes is called Fluc (North American firefly luciferase). Fluc emits light with a spectrum wavelength of 630-640nm and interacts with a substrate named D-luciferin, oxygen, ATP, and magnesium as cofactors in tissue [58]. Optical coherence tomography utilizes coherence interferometry to image the scattering tissue [59, 60], and can be used for imaging structures *in vivo* with a high resolution of 2-15μm at a depth of 1-3mm [5]. There are other new non-fluorescence-based optical imaging modalities, like Cerenkov luminescence imaging [61], but they will not be exhaustively discussed here.

Understanding fluorescence-based noninvasive imaging begins with the definition of fluorescence. Certain molecules absorb light at a particular wavelength and emit light at longer wavelengths and lower energy after a short fluorescence dwelling time. Excitation light and emission light refers to these two distinct wavelengths of light, and they enable fluorescent signal detection and imaging [5]. Although fluorescence imaging suffers from penetration depth as well as high auto-fluorescence (which affects sensitivity), it remains a valuable and versatile modality because of its low cost, multiplexing, and high-sensitivity [12]. The physical process for fluorescence involves four important components with regard to *in vivo* molecular imaging: an excitation light source at a particular wavelength (specific filters in front of a white light source can produce this), emission filters to remove the excitation light or the auto-fluorescence light, a fluorescence probe, and a scientifically cooled CCD camera sensitive to NIR wavelengths.

Fluorescence probes are key to molecular imaging, and can be divided into two rough categories: targeted and non-targeted [62]. Near-infrared non-targeted probes are non-specific, and are typically used for perfusion or vascular leakage imaging. Indocyanine Green (ICG) is one of the most recognized non-targeted fluorescence probes, and is already used in clinical applications [63, 64]. A new non-targeted probe, known as Quantum Dots (QD), which has a 2-8 nm diameter core and a size-dependent fluorescence emission [62]. *In vivo* application of QD is found in the literature [65, 66]. Non-targeted probes suffer from background noise, which is a huge drawback in using these for imaging. The targeted probes can be further classified into two groups: active and activatable ones. Conjugating the fluorochrome to a ligand, such as peptides, proteins, or antibodies, forms typical active probes. These ligands bind with specific markers at the cell surface. Active probes are typically used for tumor tracking [67]. An activatable probe contains two identical or dissimilar fluorochromes, which are joined by an enzyme linker. These probes do not emit any fluorescence signal due to quenching effect. Specific enzymes in the body tissue can cleave the linker and release the fluorochromes for fluorescence emission. Activatable

probes, therefore, are suitable for imaging enzyme activity [68-70]. Apart from all of the probes described, another type of indirect fluorescence imaging molecules is fluorescence proteins (FPs). Here, an encoded reporter gene is integrated into the sequence of a cell and translated into fluorescent proteins inside of living tissue to emit a fluorescence signal suitable for imaging [71].

(a)   (b)
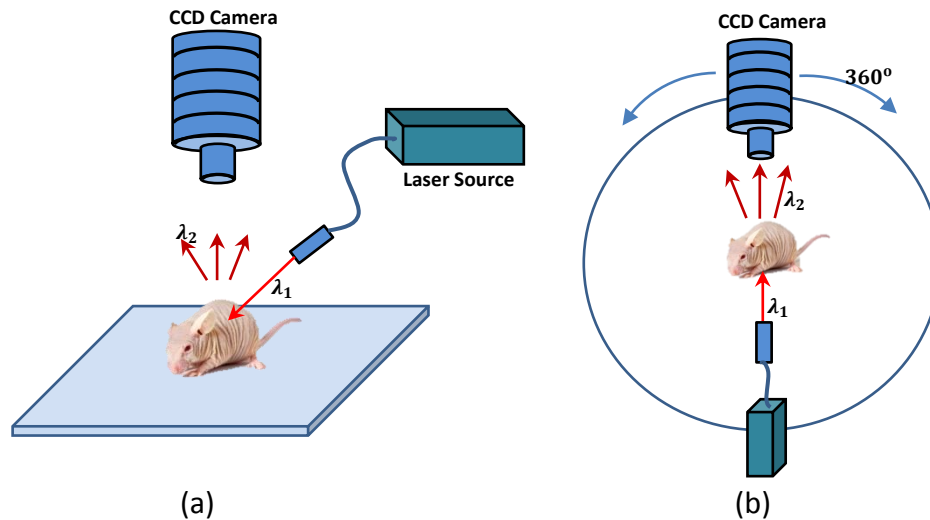
Figure 1.2. Principles of fluorescence reflectance imaging and fluorescence molecular tomography. (a) Epi-illumination mode. (b) Trans-illumination mode (without 360° rotation) and fluorescence molecular tomography (with 360° rotation and reconstruction afterwards)

As shown in Figure 1.2, two types of NIR fluorescence imaging modalities exist for performing *in vivo* animal studies: fluorescence reflectance imaging (FRI) and fluorescence molecular tomography (FMT). The FRI systems, which are also called planar two-dimensional imaging systems, can be organized into an epi-illumination mode and a trans-illumination mode [72, 73]. In epi-illumination mode, the excitation source is placed alongside the detector (with filters in front of it) on the side of test animals. A trans-illumination mode setup places the source and the detector on opposite sides of the sample. Trans-illumination images enjoy higher sensitivity, especially for the deeply seated fluorophores, when compared with epi-illumination images, but they require a longer time to produce because the background noise from the excitation wavelength [72]. Although planar fluorescence imaging has been demonstrated to be a powerful technique for many biological applications [74-76], it still suffers from a lack of depth resolution [6].

Fluorescence molecular tomography (FMT) is a novel imaging technique that enables three-dimensional quantification of fluorescence probe location and distribution

relatively deep within animal tissue. FMT data collection involves placing the living test animal in the center of an FMT system, when excitation light illuminates the sample, the signal is collected by CCD cameras at excitation and emission wavelengths for image reconstruction. The second part is the mathematical modeling of the light propagation, and the inversion algorithms. Distinct from the planar fluorescence imaging modality, FMT utilizes focused NIR laser light to illuminate the animals. Generated source-detector pairs for each measured excitation/emission set are then used for FMT inversion [71, 77, 78]. Preclinical applications for the FMT imaging modality includes monitoring tumor location [79], integrin receptor expression imaging [80], visualization of antitumor treatment [81], and quantification of pulmonary inflammation [82].

The inversion presents a disadvantage for FMT imaging, because the light scattering in living tissue results in the inverse problem becoming ill-posed and difficult to find the closed form solution [83, 84]. Further, FMT has the ability to provide functional information like radionuclide imaging, hence can provide images with poor spatial resolution (mainly due to light scattering). A hybrid combination of FMT imaging with anatomical imaging modalities like XCT becomes an attractive option. A hybrid FMT-XCT system not only provides anatomical/molecular merged information, which helps analyzing the biological process, but the incorporated priori anatomical information from a CT also improves the accuracy of FMT inversion and provides higher resolution, sensitivity, and deeper penetration comparing with standalone FMT [85-87].

1.3 Objects and outline

The goal of this thesis is to investigate the applicability of the newly developed hybrid FMT-XCT system for different *in vivo* respiratory and cardiovascular imaging applications. The investigation is focused on imaging the thorax region. Three representative non-invasive biological experiments were conducted to demonstrate the performance of the FMT-XCT system and inversion strategies. The first one is to quantify asthmatic inflammation and remodeling using two different fluorescence probes and in a special asthmatic mouse model. The second application is related to a commonly encountered cardiovascular disease: atherosclerosis. In this context a new background subtraction method for FMT-XCT inversion was developed and validated on this particular mouse model. The last demonstration is focused on non-small cell lung cancer (NSCLC) research. Epi-illumination fluorescence imaging modality—named

cryoslicing—and histological methods were chosen to verify the quantification of FMT-XCT tomography results.

The whole thesis is structured as follows. Chapter 2 elaborates the light propagation scheme in biological tissue, referred to as the forward model; two typical phantom experiments were performed to validate our FEM-based forward model code. Chapter 3 covers all hardware and software components of the hybrid FMT-XCT system, including: the finite element method for the light propagation, regularization and LSQR based solver for image reconstruction in FMT-XCT, FMT-XCT hybrid motivation (regularization matrix (Laplacian) built based on segmented XCT image), FMT-XCT data collection, and post processing. A cylindrical phantom experiment also ensured that every aspect of the FMT-XCT system functioned perfectly. An additional XCT evaluation experiment of nodule progression tracking for the lung tumor mouse model proves the high-quality performance of standalone XCT modality. Chapter 4 presents asthma-related inflammation and remodeling quantification by the FMT-XCT system with subsequent cryoslicing and histological validation. Chapter 5 explains the quantification of neutrophils from the process of longitudinal atherosclerosis study with the FMT-XCT system as well as an optimized inversion method using two - wavelengths FMT data. Cryoslicing and histology was used to validate the results. Chapter 6 elaborates another longitudinal study of the NSCLC disease mouse model using the FMT-XCT system. After concluding the performance of FMT-XCT tomography from these three typical respiratory and cardiovascular *in vivo* studies, new ideas about future development, optimization, and application of the FMT-XCT system are reasoned in Chapter 7.

2 Forward model of FMT

2.1 Introduction

The mathematical basis of FMT-XCT reconstruction comes from modeling light propagation in biological tissue. FMT reconstruction involves two steps: the forward model and the inversion [84]. In the forward model, the excitation light source and all optical properties are known in order to predict the propagated light at specific measurement locations. With the inversion, both the optical parameters of biological tissue and the output light distribution are known, and then the fluorescence distribution is estimated. The quality of FMT reconstruction depends strongly on the accuracy of the forward model. Therefore, this chapter will introduce the forward model of light propagation in tissue, and the implementation of forward model using numerical finite element method (FEM) will be explained. An iterative method, biconjugate gradient stabilized (BICGSTAB), will also be explained and implemented to solve the forward model. To verify the accuracy of the forward model, two different shapes of tissue-like phantom experiments with a home-built BBQ imaging system will be conducted.

2.2 Radiative transfer equation and diffusion approximation

The well-known radiative transfer equation (RTE, or the Boltzmann equation) can accurately model photon propagation in biological tissue. Succinctly, the RTE

describes how a beam of light loses energy by divergence, absorption, and scattering away from the beam, and gains energy both from light sources in the medium and scattering directed toward the beam [88]. The RTE in the time-domain is written as:

$$\frac{1}{c}\frac{\partial L(\boldsymbol{r},\boldsymbol{s},t)}{\partial t} + \nabla L(\boldsymbol{r},\boldsymbol{s},t)\cdot \boldsymbol{s} + (\mu_s + \mu_a)L(\boldsymbol{r},\boldsymbol{s},t) = \\ \mu_s \iint_{4\pi} L(\boldsymbol{r},\boldsymbol{s},t)f(\boldsymbol{s}\cdot \boldsymbol{s}')d\Omega' + Q(\boldsymbol{r},\boldsymbol{s},t) \tag{2.1}$$

In Equation 2.1, $L(\boldsymbol{r},\boldsymbol{s},t)$—called radiance and expressed in $[Wm^{-2}sr^{-1}]$—is defined as the average power flux density per unit normal area per unit solid angle per unit time. Here, c is the speed of light in the medium, expressed in $[m\ s^{-1}]$. Each μ_s and μ_a, both expressed in $[m^{-1}]$, are the optical scattering coefficient and absorption coefficient, respectively. $Q(\boldsymbol{r},\boldsymbol{s},t)$ $[Wm^{-2}sr^{-1}]$ is the light source. Scattering phase function, $f(\boldsymbol{s}\cdot \boldsymbol{s}')$, represents the probability of a photon scattering from the direction $\boldsymbol{s}$ into direction $\boldsymbol{s}'$. If the phase function is uniform in the medium, then it is called isotropic scattering medium. If not, the medium is anisotropic.

Unfortunately, because the RTE is an integro-differential equation, it is computationally complex and difficult to solve analytically. Typically, one chooses numerical methods to solve it; however, it is still memory and time consuming (as RTE has six degrees of freedom) to find a solution for large tissue volumes through numerical methods. By satisfying some specific conditions, simpler approximations to RTE can be derived. One of the most commonly used approximations in optical tomography is the diffusion approximation (DA) [88]. First, the P1 spherical harmonics approximation of radiance is given as:

$$L(\boldsymbol{r},\boldsymbol{s},t) = \frac{1}{4\pi}\Phi(\boldsymbol{r},t) + \frac{3}{4\pi}J(\boldsymbol{r},t)\cdot \boldsymbol{s} \tag{2.2}$$

Where $\Phi(\boldsymbol{r},t)$ is called fluence rate (or photon density) and defines the energy flow per unit area per unit time, and $J(\boldsymbol{r},t)$ is called current density (or photon flux), which defines the net energy flow per unit area per unit time, both are written as:

$$\Phi(\boldsymbol{r},t) = \iint_{4\pi} L(\boldsymbol{r},\boldsymbol{s},t)d\Omega \tag{2.3}$$

$$J(\boldsymbol{r},t) = \iint_{4\pi} \boldsymbol{s}L(\boldsymbol{r},\boldsymbol{s},t)d\Omega \tag{2.4}$$

Further, by introducing Fick's law of diffusion, which describes the diffusion process of photons in a scattering medium, one can get:

$$J(r,t) = -D(r)\nabla\Phi(r,t) \tag{2.5}$$

In equation 2.5, the space-dependent variable $D(r)$ is referred to as the diffusion coefficient, which is given as:

$$D(r) = \frac{1}{3[\mu_a(r) + \mu_s'(r)]} \tag{2.6}$$

Here, the μ_s' is called the reduced scattering coefficient, defined by:

$$\mu_s' = (1 - g)\mu_s \tag{2.7}$$

In this definition, g represents the anisotropy coefficient of the media. For isotropic media, $g = 0$, and for biological tissue application, $g \approx 0.9$.

By substituting Equation (2.2) and (2.5) into the RTE Equation (2.1), one obtains the diffusion equation in the time domain:

$$\nabla \cdot [D(r)\nabla\Phi(r,t)] - \mu_a(r)\Phi(r,t) = \frac{1}{c}\frac{\partial\Phi(r,t)}{\partial t} - q_0(r,t) \tag{2.8}$$

By applying a Fourier Transformation onto Equation (2.8), one acquires the diffusion equation in the frequency domain:

$$\nabla \cdot [D(r)\nabla\Phi(r,\omega)] - \mu_a(r)\Phi(r,\omega) = \frac{j\omega}{c}\Phi(r,\omega) - q_0(r,\omega) \tag{2.9}$$

When $\omega = 0$, diffusion equation (DE) of continuous wave (CW) domain (or steady state) is written as:

$$\nabla \cdot [D(r)\nabla\Phi(r)] - \mu_a(r)\Phi(r) = -q_0(r) \tag{2.10}$$

The DE derivation uses two approximations: one is the first order (P1) spherical harmonics approximation of radiance ($L(r,s,t)$), and the other one is that the

fractional change in photon flux is trivial over one mean free path. These two approximations can be translated into one condition: $\mu_s' \gg \mu_a$, which states that the reduced scattering coefficient is far greater than the absorption coefficient, so the photons in media can sufficiently scatter before being absorbed.

When near-infrared light propagates through the biological tissue, it is enough to satisfy this condition. For example, from reference [89], at the near-infrared window, the absorption coefficient of human forearm is around 0.1, $\mu_a \approx 0.1 \; cm^{-1}$. On the contrary, the reduced scattering coefficient is around 10, $\mu_s' \approx 10 \; cm^{-1}$.

For developing accurate forward model, boundary conditions must be applied. Light propagation at the air-tissue boundary interface can be accurate described with the Robin boundary condition [90]. This condition is index-mismatched, which means the photons leaving the tissue edge are equal to the fluence rate at the boundary multiplied by a factor of internal reflection. This relationship can be expressed as:

$$\Phi(\boldsymbol{r}) + 2DA\hat{n} \cdot \nabla\Phi(\boldsymbol{r}) = 0 \tag{2.11}$$

In Equation (2.11), the value of A depends on the mismatch of relative refractive index between air and tissue. A can be defined as [90]:

$$A = \frac{1 + r_d}{1 + r_d} \tag{2.12}$$

Where,

$$r_d = -1.440 n_{rel}^{-2} + 0.710 n_{rel}^{-1} + 0.668 + 0.063 n_{rel} \tag{2.13}$$

and n_{rel} is the relative refractive index mismatch between tissue and air. For a typical tissue-air boundary, A is a fixed number (A $\approx$ 2.74).

2.3 Forward model: finite element method

A diffusion equation is a complex partial differential equation, and there are three methods to solve it [91]. Firstly, an analytical model using Green's function can be used. The Green's function method is only accurate to solve the forward problem

when the optical source and the geometry are simple, such as a slab or an infinite half-space. Notably, DE can be solved analytically using a Kirchhoff approximation, Jorge Ripoll et al. tried to solve the DE with an analytical function in an arbitrary geometry medium [92]. The second method is a statistical modeling technique, also called a Monte Carlo method [93]. Monte carlo scheme simulates the physical propagation process of a large number of random photons, and does not have diffusion approximations or geometry limitations. Because of its accuracy in simulating light propagation in biological tissue, it is considered the gold standard (and equivalent to solving the RTE). One crucial drawback hindering wider use of monte carlo in optical tomography is the computational time associated with monte carlo, since it calculates every photon within tissue. The last method is the numerical modeling methods. To solve the DE with an arbitrary geometry with inhomogeneous distribution of optical properties, one of the best numerical modeling methods is the finite element method (FEM) [94].

The first step of the FEM is to discretize the region Ω into N_e elements (in this thesis, we choose tetrahedral as one element) ($\Omega_1, \Omega_2, \dots \Omega_{N_e}$) and N_v vertex nodes ($V_1, V_2, \dots V_{N_v}$). Based on this discretization, the photon density $\Phi(\boldsymbol{r})$ is approximated with a piecewise polynomial interpolation function:

$$\Phi(\boldsymbol{r}) \approx \sum_{i=1}^{N_v} \emptyset_i \psi_i(\boldsymbol{r}) \tag{2.14}$$

Here, $\psi_i(\boldsymbol{r})$ is the basis function and $\emptyset_i$ represents nodal value of $\Phi(\boldsymbol{r})$ on tetrahedral vertex V_i. The DE (2.10) can be rewritten as a weak form equation using the Galerkin approach to obtain $\Phi(\boldsymbol{r})$ [95]：

$$\int_\Omega \psi(\boldsymbol{r})[\nabla \cdot D(\boldsymbol{r})\nabla - \mu_a(\boldsymbol{r})]\Phi(\boldsymbol{r})d\Omega = -\int_\Omega \psi(\boldsymbol{r})q_0(r)d\Omega \tag{2.15}$$

After integration by parts and including the Robin boundary condition, the equation (2.12) can be modified to the following matrix equation:

$$[\mathrm{K} + \mathrm{C} + \mathrm{F}]\Phi = Q \tag{2.16}$$

or

$$\mathrm{A}\Phi = Q \tag{2.17}$$

15

$$A = K + C + F \tag{2.18}$$

where

$$
\begin{cases}
K_{ij} = \displaystyle\int_\Omega D(\boldsymbol{r})\nabla\psi_i(\boldsymbol{r}) \cdot \nabla\psi_j(\boldsymbol{r})d\Omega \\[2mm]
C_{ij} = \displaystyle\int_\Omega \mu_a(\boldsymbol{r})\psi_i(\boldsymbol{r})\psi_j(\boldsymbol{r})d\Omega \\[2mm]
F_{ij} = \dfrac{1}{2A}\displaystyle\int_{\partial\Omega} \psi_i(\boldsymbol{r})\psi_j(\boldsymbol{r})d\partial\Omega \\[2mm]
Q_{ij} = \displaystyle\int_\Omega q_0(\boldsymbol{r})\psi_i(\boldsymbol{r})d\Omega \\[2mm]
\Phi = [\Phi_1, \Phi_2, \ldots, \Phi_{N_v}]^T
\end{cases}
\tag{2.19}
$$

Equation (2.17) is a linear equation solved for unknown variant Φ. The matrix A, also known as a stiffness/mass matrix, is built up by three components, K, C, and F. Matrices K, C, and F are symmetric, sparse, and positive-definite, with the same size $N_v \times N_v$, which means stiffness matrix A is also positive-definite and symmetric. In equation (2.19), Ω is whole tissue volume and $\partial\Omega$ denotes tissue surface.

2.4 Biconjugate gradient stabilized method

The conjugate gradient (CG) [96] method, invented by Hestenes and Stiefel, is one of the well-known algorithm for the numerical solution of a linear equation, which is often implemented as an iterative method. The conjugate gradient method is most applicable when the matrix is sparse and large, and is too computationally complex for a direct inversion, such as the Cholesky decomposition. This method is an orthogonal projection technique in Krylov subspace; it is the most widely used iterative method for solving a linear system of equations like Eq. (2.17).

The solution Φ^* for Eq. (2.17) is also the unique solution x^* of minimization of the quadratic test function:

$$f(x) = \frac{1}{2}x^\top A x - x^\top b \tag{2.20}$$

Here, b = Q. The iterative method to find the solution x^* is to choose an initial guess x_0 first, then, for each further step, walk along a gradient direction so that $f(x_{k+1}) < f(x_k)$. Different strategies are proposed for choosing the gradient direction p_k and step length a_k to find next closer solution:

$$x_{k+1} = x_k + a_k p_k \qquad (2.21)$$

For the CG method, the conjugate direction and the step length is given by:

$$\begin{cases} a_k = \dfrac{r_k^\mathsf{T} r_k}{p_k^\mathsf{T} A p_k} \\ p_{k+1} = -r_{k+1} + \beta_k p_k \end{cases} \qquad (2.22)$$

Where $k = 0,1,2,\dots$ and

$$\begin{cases} \beta_k = \dfrac{r_{k+1}^\mathsf{T} r_{k+1}}{r_k^\mathsf{T} r_k} \\ r_{k+1} = r_k + a_k A p_k \end{cases} \qquad (2.23)$$

For start of the iterative loop, $r_0 = A x_0 - b$ and $p_0 = -r_0$.

The biconjugate gradient stabilized method—also known as BiCGSTAB—is a variant of the CG method developed by H. A. van der Vorst [97] in 1992. It is also an iterative method for the numerical solution of nonsymmetric linear systems and yields much faster and smoother convergence than the normal CG method or other CG variants like conjugate gradient squared (CGS). The BiCGSTAB method has two different types: preconditioned BiCGSTAB and unpreconditioned BiCGSTAB. A preconditioner is useful to accelerate the convergence of this method with form $K = K_1 K_2 \approx A$. The BiCGSTAB algorithm is given as [97]:

1. $r_0 = b - A x_0, \ p_0 = r_0$
2. For $j = 0, 1, 2, \dots$
3. $a_j = \dfrac{(r_j, r_0)}{(A p_j, r_0)}$
4. $s_j = r_j - a_j A p_j$
5. $\omega_j = \dfrac{(A s_j, s_j)}{(A s_j, A s_j)}$
6. $x_{j+1} = x_j + a_j p_j + \omega_j s_j$
7. $r_{j+1} = s_j - \omega_j A s_j$

8. $\beta_j = \frac{(r_{j+1}, r_0)}{(r_j, r_0)} \times \frac{a_j}{\omega_j}$

9. $p_{j+1} = r_{j+1} - \beta_j(p_j - \omega_j A p_j)$

10. End

2.5 Forward model validation

Forward model accuracy is vital in FMT-XCT reconstruction. Therefore, verification of the FEM-based forward model code written is taken up. Comparing the simulation results with controlled experiment results with a slab and cylinder phantom achieves this verification.

2.5.1 System setup
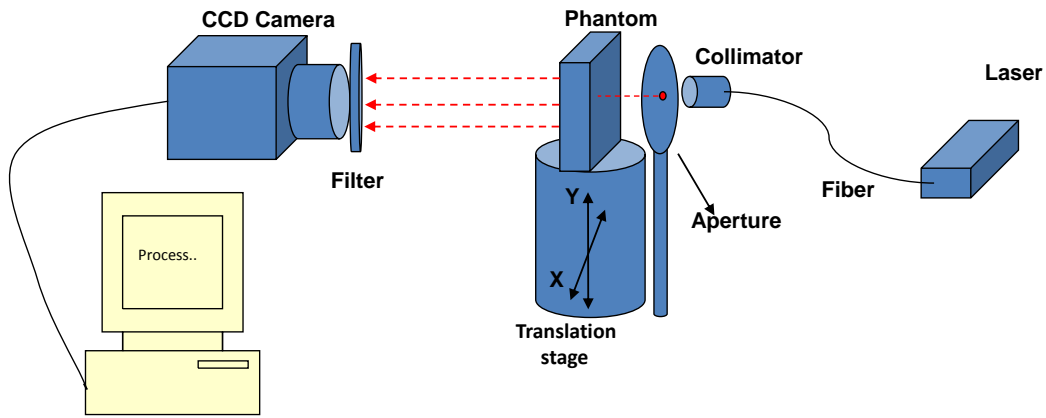
Figure 2.1. Schematic diagram of the trans-illumination BBQ imaging system.

To verify the FEM-based forward modeling code, a trans-illumination BBQ imaging system was built (Figure 2.1). The laser source used in this setup is an energy-tunable diode laser (B&W Tek Inc., Newark DE) operating at 670 nm. The laser was fiber-coupled into a collimator, which (Thorlabs, Dachau, DE) helps in aligning the laser light propagation in a specific direction, as well as an aperture to ensure that the laser shining point is as small as possible. After entering the collimator the light rays travels parally, which spread slowly as they propagate through the tissue. The laser beam was focused onto the surface of the phantom that was positioned on a translation

stage and was able to be scanned in the x-y direction. A scientific CCD camera (Princeton Instruments, Inc. Trenton, NJ) was cooled to -70 centigrade, this camera with a Nikkor 50 mm f/1.2 photographic lens (Nikon Corp., Japan) was placed on the opposite side of phantom to collect trans-illuminated photons. A neutral density (ND) filter (Chroma Technology Corp., Rockingham, VT) was positioned in front of the lens to reduce the transmittance of light evenly over the entire spectrum. To obtain a tiny light spot, the distance between aperture and phantom ought to be minute and the aperture size should also be small; here, the size of the spot was around 1 mm. The entire system was enclosed in a black box to keep out ambient light. The collected images was saved and analyzed by computer with an Intel (R) Core (TM) 2 Duo CPU @3.00 GHz and 8 GB RAM.

The source laser's output power stability was tested prior to verification of forward model, since stability would directly influence any results. The BBQ system acquired a series of phantom figures (60 figures) over the time the laser light was on. For each figure, one fixed region (400 pixels) was chosen and a mean value of this region was calculated for comparison. Every parameter of data collection of the BBQ system was constant: the aperture size was 2.8, integration time of the CCD camera was 20 seconds, etc. Stability test results are plotted in Figure 2.2. Figure 2.2 (a) shows the average pixel value of all figures without laser power changes. Figure 2.2 (b) displays the average pixel value by changing the power after some time. From (a) and (b), a clear result that emerges is that the laser power stabilizes about five minutes after turning it on. Figure 2.2 (b) also shows that after the laser stabilizes (five minutes later), the laser power remains almost stable even after one changes it.
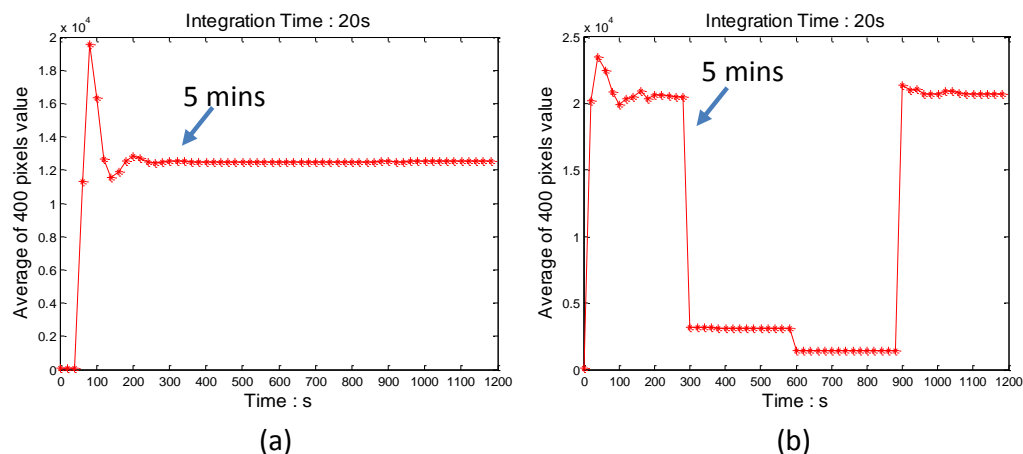

(a)　　　　　　　　　　(b)

Figure 2.2. Laser power fluctuations over time.

The verification in this setup used a silicon phantom. To build a slab homogeneous silicon phantom with a volume of 200 ml, 100 ml of Ecoflex 0030 Part A and 100 ml of Ecoflex 0030 Part B (Smooth-On, Inc., Easton, USA) were mixed together. The optical properties (absorption coefficient μ_a and scattering coefficient μ_s) of the phantom were controlled by mixing two different pigments: Silc Pig white pigment (Smooth-On, Inc., Easton, USA. 13mg per 1.0/cm μ_s) and Silc Pig black pigment (Smooth-On, Inc., Easton, USA. 1.3mg per 0.1/cm μ_a) into the phantom. First, the premeasured amounts of black and white pigments were added into the 100 ml Part A in a falcon tube. Then, Part B was added into the same tube. Third, that tube was put into a centrifuge for around 10 minutes to remove the air bubbles in the phantom. After waiting for 12 hours, the silicon phantom with specific optical parameters ($\mu_a = 10$/m, $\mu_s = 1000/m$) was made. Figures 2.3 (a) and (d) show the real phantom.

The entire imaging procedure included several steps. The first requirement was to set up the system and focus the camera. The camera aperture was set as 2.8, which is the smallest, meaning smallest depth of field (DOF). The second task was to set up the imaging parameters by using the commercial software Winview (Princeton Instruments, Inc. Trenton, NJ), where the integration time was 0.5s. The laser power was set as 0.1 mA. This step involves taking a direct image of the laser without a phantom between the laser and the camera to find the source position as an original coordinate. All attempts were made to make this original position in the middle of imaging area. Third, a grid paper (as shown in Figure 2.3 (a)) was put on the phantom and phantom was placed in between them. Initially a white image was captured. The grid paper image was used for calculating the ratio of the CCD camera pixels and real distance. Fourth, the grid paper was removed and imaging parameters were adjusted (the laser power was set as 0.9 mA, and the integration time was kept at 30 s). During this step, a completely dark imaging environment was maintained. After waiting five minutes, acquisition of the first image began. Finally, by moving the translation stage, different source-positioned images were captured for FEM-based forward model code validation.

For simulating the FEM-based forward model, the code was based on solving a linear equation (2.17) using the BiCGSTAB method developed by the programming language MATLAB. For each phantom in the experiments, the meshing was generated by using an FEM module from the CGAL library [98]. The mesh library is able to generate tetrahedral meshes for many volumes; each pixel in the volume space is assigned a number representing its position. In the simulation, the optical parameters are also the same as compared with the real silicon phantom ($\mu_a = 10$/m, $\mu_s = 1000/m$).

2.5.2 Verification experiment 1: slab silicon phantom

To verify the forward model code, two experiments were performed. Firstly a silicon slab homogeneous phantom was used. Figure 2.3 shows the phantom information: (a) displays the real phantom, sticking on a grid paper; (b) illustrates the schematic figure of the phantom, which also labels its size, $21.2\text{mm} \times 45.4\text{mm} \times 48.5\text{mm}$; (c) presents the mesh used for the code simulation. The mesh was built with 69,984 nodes and 38,7172 tetrahedral elements with an average edge length of 1 mm. Figure 2.3 (d) presents the real phantom marked by the relative light source and detector locations. The blue dots and numbers indicate the laser source, which was illuminated from the other side of the phantom. Red dots show the 529 detector points chosen from the real phantom to calculate the trans-illuminated light intensity compared with the corresponding simulation results.
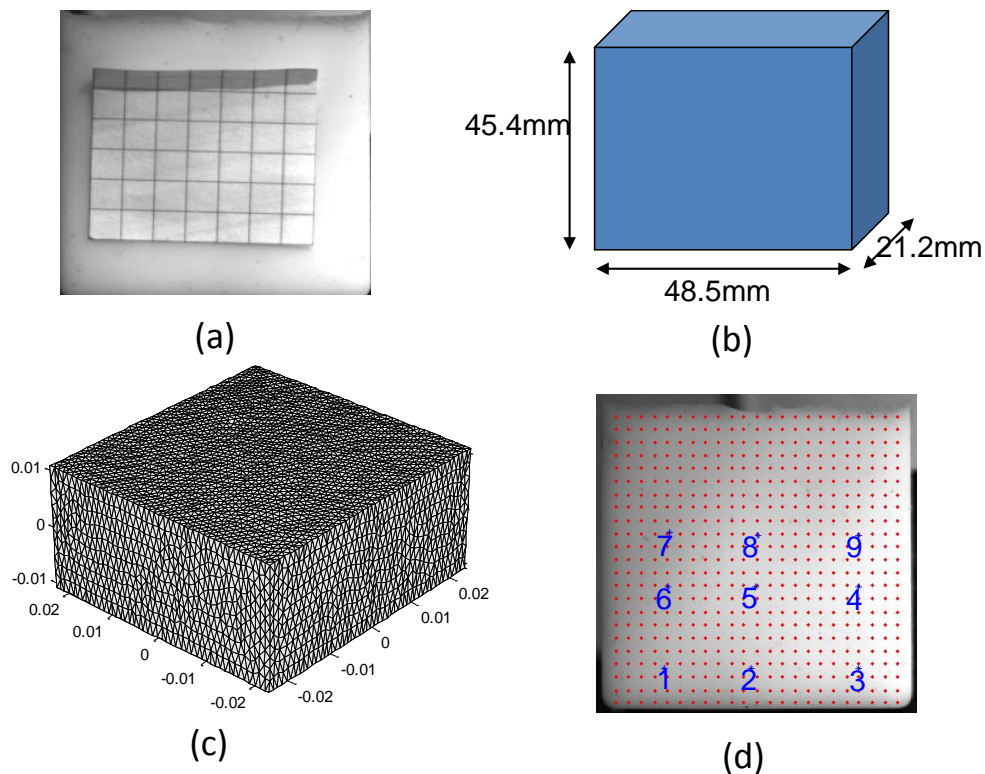

(a)

(b)

(c)

(d)

Figure 2.3. Slab silicon phantom used in FEM forward model code validation. (a) is the real phantom stick with a white grid paper. (b) is the schematic figure of the real phantom. (c) is the mesh used for the FEM forward model simulation. (d) is the real phantom painted with red detector points and blue light source points.

Figure 2.4 exhibits the results of verification using the slab homogenous silicon phantom. Figure 2.4 shows two results from two different laser illumination locations, respectively. The first illumination location was almost in the middle of the phantom. The location is illustrated in Figure 2.4 (a) by a white dot and pointed out with a black arrow. The actual location is located by the other side of the phantom. Figure 2.4 (a) and (b) shows the experimental image and the simulated image, respectively. They appear exactly the same. Figure 2.4 (c) shows the intensity profile from both images after being normalized to their respective maxima. Red stars in Figure 2.4 (c) are normalized light intensity from the experimental image. On the other hand, the blue stars are normalized intensity from the code-simulated image. The simulated observation matches very well with the experimentally measured data. To make sure the code also worked well if the laser was located around the phantom's corner, one laser location was also chosen to test the boundary condition, shown in Figure 2.4 (d)-(f). The laser's relative location is shown in Fig. 2.4 (d) by a white dot, which is near the boundary of the phantom. Figure 2.4 (d) and (e) show the experimental and simulated intensity images, respectively. The two images look similar to the casual eye. The pixel-by-pixel intensity profile plot in Fig. 2.4 (f) also demonstrates that the simulated image fits well with the experimental one. One interesting finding from figure 2.4 (d) is that the center of intensity ring does not match with the source location. This is because of the boundary condition. Therefore, the intensity ring's center is a slightly off from the laser source location.
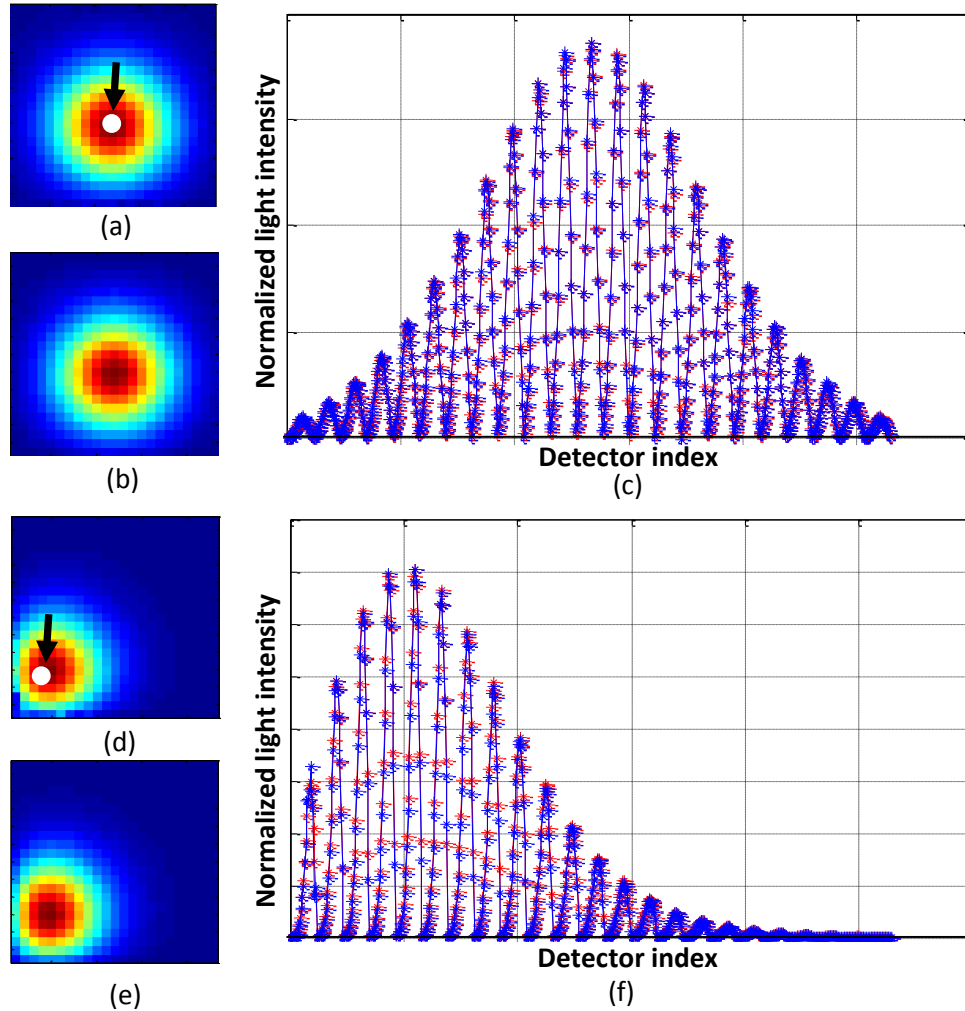
Figure 2.4. FEM-based forward model validation using slab phantom measurements with two different laser point location: (a)-(c) validation results by laser point located in the middle of phantom (white dot shown in (a) pointed by black arrow) illuminated from the other side of the phantom. (a) is the pseudo-colored intrinsic image from physical experiment. (b) is the pseudo-colored code simulated signal image. (c) is the two images' normalized signal intensity profile. Red stars in (c) are intensity from phantom experiment, blue stars from code simulation, respectively. (d)-(f) are validation results with laser pointed at another location (white dot in (d)).

2.5.3 Verification experiment 2: cylinder silicon phantom

The slab homogeneous silicon phantom is easy for the FEM-based forward model code to simulate. To validate the robustness and flexibility of the code, a second experiment with a cylinder silicon phantom was also performed. The same procedure described in Section 2.5.1 guided this phantom setup. Details about the phantom

(Figure 2.5 (a)) show the actual phantom positioned on a translation stage, with a grid paper on it. Figure 2.5 (b) illustrates the size of the phantom, which is 67 mm in length and with a diameter of 29 mm. The cylindrical mesh used for the simulation is shown in Figure 2.5 (c). The mesh was generated by code CGAL, with 7,599 nodes and 46,816 tetrahedral elements. Red dots in the figure show the detectors used in the simulation for comparison with the real experimental results.
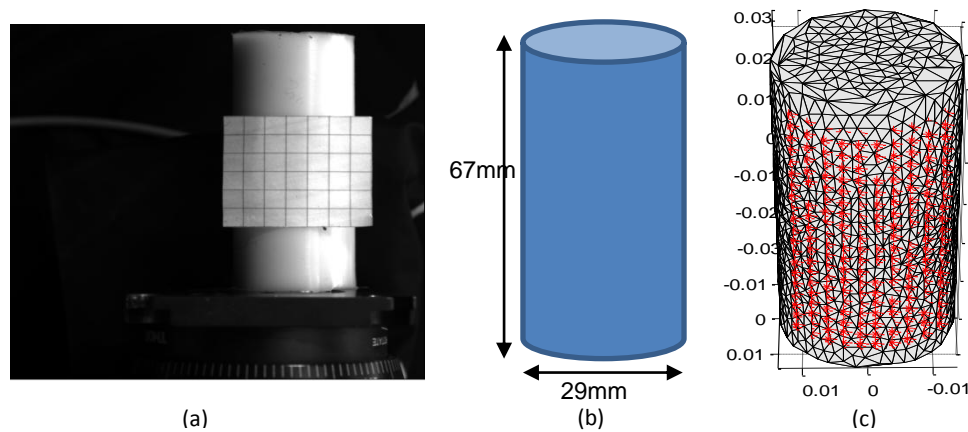

(a)   (b)   (c)

Figure 2.5. Cylinder silicon phantom used for forward model verification. (a) is the real phantom pasted with white grid paper. The schematic figure, (b), shows the dimension of the real phantom. (c) is the mesh generated by CGAL. Red dots on the surface are detectors.

Figure 2.6 compares the physical experimental image and the FEM code-generated image when using a homogeneous cylinder phantom with two different locations of illumination. Figures 2.6 (a)-(c) show the results of the first laser point, which lies exactly on the surface center of the cylinder phantom, where 2.6 (a) locates this with a black dot. Figure 2.6 (a) illustrates the intrinsic image of the physical experiment. The pseudo-colored intensity map is symmetrical because the laser illuminates the surface center and the phantom is homogeneously symmetrical. The pixels closer to the boundary have a higher intensity value because the boundary region has a thinner size. Figure 2.6 (b) shows the image achieved by the forward model simulation code, which, to the naked eye, depicts an extremely similar intensity distribution as Figure 2.6 (a). To quantify the difference between the two different results, the normalized light intensity comparison is displayed in Figure 2.6 (c). Both image's pixel intensities were normalized by maximum values from each image. Red dots in Figure 2.6 (c) represent the relative intensity values of each pixel from the experimental image after normalization. Blue dots in the same figure indicate the corresponding normalized pixel intensity from the simulated image. The plot in Figure 2.6 (c) is also symmetric

since the pixel intensity is ordered vertically. Figure 2.6 (c) also reveals that the image from the code simulation matches completely with the experimental image. By changing the laser illumination point from the surface midpoint to the right (closer to the boundary), the same comparison results can be found in Figure 2.6 (d)-(f).
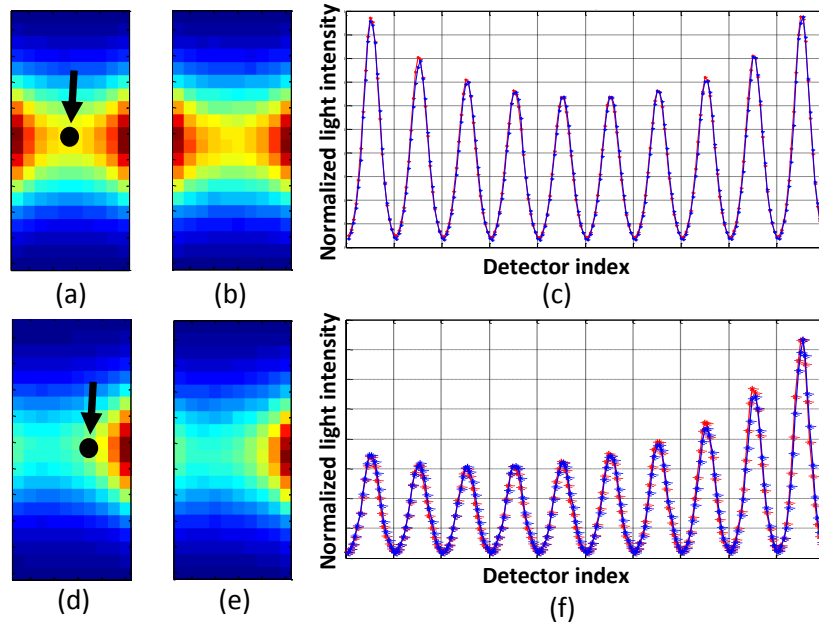

(a)   (b)   (c)

(d)   (e)   (f)

Figure 2.6. FEM-based forward model verification using a cylinder homogeneous phantom with two laser illumination locations. (a)-(c) show validation results from first laser source illuminated from the middle of the phantom (big black dot in (a) pointed by a black arrow). (a) is the pseudo-colored intrinsic illumination image from physical experiment. (b) represents the pseudo-colored simulated image from the FEM forward model code. (c) compares the normalized light intensity profile between the experimental image and the simulated image. Red stars in (c) are intensity values from the physical phantom experiment. Blue stars are from the code simulation. (d)-(f) show the corresponding comparison results from second laser source illuminated from one location closer to the boundary (also marked by a black dot in (d)).

Table 2.1. Code simulation consistency validation. E = experiment. S = simulation.

		Center	Left	Right	Difference
Slab	Max(E)	11421	11109	11109	0.18%
	Max(S)	3.5583e-07	3.5314e-007	3.5160e-007	0.22%
	Ratio	3.2097e+010	3.1458e+010	3.1712e+010	0.4%
Cylinder	Max(E)	4882	7053	6950	1.47%
	Max(S)	2.352e-07	3.466e-007	3.480e-007	0.38%
	Ratio	2.0757e+010	2.0344e+010	1.997e+010	1.85%

To test the consistency of the FEM forward model code, two symmetrical laser illumination points—a left one and a right one symmetrical to the surface center of each phantom—were chosen to image and analyze. The results are presented in Table 2.1. The parameter used for comparison is the maximum intensity value of each acquired image. From Table 2.1's slab phantom group data, the intensity difference between the left source and right source of experimental is 0.18%. The corresponding difference from the code simulation is 0.22%, which is small and comparable to the physical experiment's result. This number also means that the physical experiment worked well. On the other hand, for the homogeneous cylinder phantom case, the intensity difference between the two symmetrical laser sources is 1.47% for the experimental image. The difference from the simulation is 0.38%, which is negligible and demonstrates that the simulation code is practicable. The disparity from the experiment is a little higher and may result from the actual experimental process, since it is challenging to calibrate two perfectly symmetrical laser points that are also on the same plane parallel with the CCD plane. Time cost of the forward model code was also tracked throughout the whole experiment. Of course, this time cost depended on the mesh size, accounting for nodes, and elements. For both phantoms, over 95% of time was consumed on computing the FEM matrix A (size of $N_v \times N_v$) and calculating the sparse preconditioner matrix for the BiCGSTAB method.

2.6 Conclusion

This chapter focused on the forward model of light propagation through tissue, which is the mathematical basis for an FMT-XCT formulation model. It began by deriving the diffusion equation from the radiative transfer equation under a specific tissue application situation. By using the FEM method, the forward model of diffusion equation was reduced to a linear system of equations by combining the Robin boundary condition. As a result, the forward model can be described as a calculation of Φ in Formula 2.17 by knowing stiffness matrix A and light source matrix Q. A preconditioner of the BiCGSTAB method was implemented in MATLAB to solve the FEM-based forward model (Equation 2.17). Two different homogeneous silicon phantom experiments showed that the forward model code was capable of accurately modeling light propagation, and the simulated image almost perfectly matched the physical experiment image. To conclude, the forward model is only a basis for the FMT-XCT physical model. The next chapter will describe the complete mathematical

model for FMT-XCT, including the inversion problem, the FMT-XCT system, and reconstruction code.

3 FMT-XCT reconstruction

3.1 Introduction

Imaging the underlying fluorescence distribution in tissue involves two parts: the forward model and inversion problem. The forward model predicts the intensity measurements by inputting a known light source and optical parameters. By knowing the outer measurements, the inversion problem tries to reconstruct the unknown underlying fluorescence contribution. Chapter 2 presented the numerical forward model derivation from the radiative transfer equation to diffusion equation based on diffusion approximation and the FEM method. After building a forward model of the system, an inverse problem calculates fluorescence source distribution. This chapter attempts to derive a mathematical model for the FMT inversion problem that describes the relationship between FMT measurement images and the unrecognized fluorophore distribution in tissue. A regularization method will be discussed for solving an ill-posed linear system of equations. An iterative least squares QR (LSQR) method will be described for solving the inversion problem. Introducing prior information into the inversion improves the FMT inversion result. Therefore, this chapter also explains hybrid FMT-XCT modality. Two investigations are taken up in this chapter—one tissue-like cylinder phantom experiment and one biological *in vivo* lung tumor longitudinal study—help discuss the performance of the FMT-XCT system, the data acquisition strategy, the inversion processing procedure, and the validation results.

3.2 Ill-posed FMT inverse problem

There are two separated light propagation processes. First, excitation laser light irradiates the biological tissue, where the light propagates through the tissue and reaches the fluorescent source. Second, the excited light from the fluorescent source propagates out of the tissue and reaches the detector. Both steps occur in biological tissue, and the FEM method [99] can model them after discretization of tissue geometry (N_e elements and N_v vertex nodes) :

$$[A_x][\varPhi_x] = [Q_x] \tag{3.1}$$

$$[A_m][\varPhi_m] = [F] \cdot [X] \tag{3.2}$$

Where,

$$
\begin{cases}
A_{xi,xj} = \int_\Omega [D_x(\boldsymbol{r})\nabla\psi_{xi}(\boldsymbol{r}) \cdot \nabla\psi_{xj}(\boldsymbol{r}) + \mu_{ax}(\boldsymbol{r})\psi_{xi}(\boldsymbol{r})\psi_{xj}(\boldsymbol{r})]d\Omega \\
\qquad\quad + \dfrac{1}{2A}\int_{\partial\Omega} \psi_{xi}(\boldsymbol{r})\psi_{xj}(\boldsymbol{r})d\partial\Omega \\
A_{mi,mj} = \int_\Omega [D_m(\boldsymbol{r})\nabla\psi_{mi}(\boldsymbol{r}) \cdot \nabla\psi_{mj}(\boldsymbol{r}) + \mu_{am}(\boldsymbol{r})\psi_{mi}(\boldsymbol{r})\psi_{mj}(\boldsymbol{r})]d\Omega \\
\qquad\quad + \dfrac{1}{2A}\int_{\partial\Omega} \psi_{mi}(\boldsymbol{r})\psi_{mj}(\boldsymbol{r})d\partial\Omega \\
Q_{xi,xj} = \int_\Omega q_0(\boldsymbol{r})\psi_{xi}(\boldsymbol{r})d\Omega \\
F_{ij} = \int_\Omega \varPhi_x \psi_{mi}(\boldsymbol{r})\psi_{mj}(\boldsymbol{r})d\Omega
\end{cases}
\tag{3.3}
$$

In Equations (3.1), (3.2), and (3.3), subscript x and m represent excitation and emission, respectively. A_x and A_m represent the excitation stiffness matrix and the emission stiffness matrix, respectively. $\varPhi_x$ and $\varPhi_m$ are column vectors, denoting the fluence rate for excitation and emission wavelengths. Q_x presents the excitation source vector. The fluorophore concentration X in (3.2) is unknown. Section 2.3 from the previous chapter clarifies that the stiffness matrix is symmetrical and definitely positive. So, for every excitation source position $s_t(t = 1,2,…,L)$, Equation (3.2) can be changed to:

$$[\Phi_{m,s_t}] = [A_m^{-1}] \cdot [F_{s_t}][X] = [B_{s_t}][X] \tag{3.4}$$

After assembling all excitation source cases, one final linear equation system between measurements and the solution vector X is formed as the following:

$$[\Phi] = [B][X] \tag{3.5}$$

The inversion problem of FMT requires solving Equation (3.5) for X by giving measurement Φ and model matrix B. Unfortunately, the linear equation (3.5) is ill-posed because it does not satisfy the three conditions set for a well-posed problem [100]: 1) a solution exists, 2) the solution is unique, and 3) the inversion solution continuously depends on the data. A small change in the data set Φ may cause a large error in X. In this study of FMT-XCT's, it is possible for the data acquisition system to introduce some electronic noise.

For fluorescence molecular tomography, the inversion is often based on solving the diffusion equation either by a theoretical method or a numerical method. The most commonly used method, known as the normalized Born approximation method [101], was developed by Ntziachristos and Weissleder in 2001. The whole concept of this method is based on the ratio of measured intensity values at the fluorescence wavelength divided by intensity values measured at the excitation wavelength. This method minimizes theoretical errors like unequal gain factors between different sources and detectors, modeling the boundary conditions, and setting up the tissue optical properties. It also eliminates instrument errors, such as the light source intensities and detector sensitivities, and generates robust and accurate fluorophore distribution even in heterogeneous media [102]. The derivation of this normalized Born approximation uses Green's functions to formulate the excitation wavelength field as:

$$U_{ex}(\boldsymbol{r}_s, \boldsymbol{r}_d) = Q_E^{\lambda_{ex}}\Theta_f^{ex}\Theta_{\det}(\boldsymbol{r}_d)G_{ex}(\boldsymbol{r}_s, \boldsymbol{r}_d)\Theta_{\mathrm{src}}(\boldsymbol{r}_s) \tag{3.6}$$

Where $Q_E^{\lambda_{ex}}$ is the detector quantum efficiency at the excitation wavelength and Θ_f^{ex} refers to attenuation from filter at excitation wavelength. Θ_{src} is the source intensity. $\Theta_{\det}(\boldsymbol{r}_d)$ is the detector gains. $G_{ex}(\boldsymbol{r}_s, \boldsymbol{r}_d)$ is the Green's function solution, which describes the propagation of photons from the source point $\boldsymbol{r}_s$ to the detector at $\boldsymbol{r}_d$ at the excitation wavelength. The most common method to calculate the Green's

function is to solve the diffusion equation (2.10) for a unit point source for the homogeneous infinite medium. It is given as:

$$g(r) = \frac{I}{4\pi D r} \exp(-\sqrt{\frac{\mu_a}{D}} r) \tag{3.7}$$

Where D is the diffusion coefficient, r is the distance from the source point, and I is the point source intensity. The same form as Equation (3.6) can also write the emission or fluorescence field:

$$U_{fl}(r_s, r_d) = Q_E^{\lambda_{fl}} \Theta_f^{fl} \times \int_V \Theta_{\det}(r_d) \, G_{fl}(r, r_d) \frac{v}{D_{fl}} n(r) G_{ex}(r, r_s) \Theta_{\text{src}}(r_s) d^3r \tag{3.8}$$

Where $Q_E^{\lambda_{fl}}$ denotes the detector quantum efficiency and Θ_f^{fl} is the attenuation of the fluorescent filter. $G_{ex}(r, r_s)$ is the Greeen's function describing the light propagation from the source point r_s to the fluorochrome location r. $G_{fl}(r, r_d)$ describes the propagation of photons from the fluorochrome at r to the detector at r_d. D_{fl} refers to the diffusion coefficient at the fluorescence wavelength, and v is the light speed in the medium. $n(\mathbf{r})$ is the fluorescence concentration of the medium, which is the unknown that requires a solution in fluorescence tomography. By using the normalized Born approximation, the fluorescence field measurement is divided by the intrinsic measurements, which can be formulated as:

$$U_c(r_s, r_d) = \frac{U_{fl}(r_s, r_d)}{U_{ex}(r_s, r_d)} = \alpha_0 \frac{\int_V G_{fl}(r, r_d) n(r) G_{ex}(r, r_s) d^3r}{G_{ex}(r_s, r_d)} \tag{3.9}$$

Where,

$$\alpha_0 = \frac{Q_E^{\lambda_{fl}} \Theta_f^{fl}}{Q_E^{\lambda_{ex}} \Theta_f^{ex}} \frac{v}{D_{fl}} \tag{3.10}$$

Since this study mainly focuses on inhomogeneous finite media, the Green's functions were solved by a numerical FEM method. Using FEM-based volumetric discretization, Equation (3.8) can be written as:

$$U_c(\boldsymbol{r}_s, \boldsymbol{r}_d) = \sum_{\Omega} \frac{G_{fl}(\boldsymbol{r}, \boldsymbol{r}_d) G_{ex}(\boldsymbol{r}, \boldsymbol{r}_s)}{G_{ex}(\boldsymbol{r}_s, \boldsymbol{r}_d)} \mathrm{n}(\boldsymbol{r}) \tag{3.11}$$

Assuming that the medium volume can be discretized into N_e volume elements, or so-called voxels, and N_v vertex nodes, the linear equation (3.11) can be written in a matrix form to find the total number of source-detector pairs N_d:

$$b_{N_d \times 1} = W_{N_d \times N_e} \cdot x_{N_e \times 1} \tag{3.12}$$

Where,

$$\begin{cases} b = U_c(r_s, r_d) \quad x = \mathrm{n(r)} \\ W = \sum_{\Omega} \dfrac{G_{fl}(r, r_d) G_{ex}(r, r_s)}{G_{ex}(r_s, r_d)} \end{cases} \tag{3.13}$$

In Equation (3.13), x is the unknown fluorescence distribution vector inside the medium of size $N_e \times 1$. The source-detector measurement vector is b with dimensions $N_d \times 1$. W is the weight matrix with dimensions $N_d \times N_e$.

3.3 Regularization and inversion by LSQR

As discussed, the Equation (3.12) is ill-posed, which means a direct inversion of it is not possible when solving for the unknown fluorescence distribution $x_{N_e \times 1}$. There are many iterative methods in the literature to solve this ill-conditioned problem for fluorescence tomography, and they are classifiable into two categories: regularization approaches and optimization strategies [103]. Some popular inversion formulas include the algebraic reconstruction technique (ART) [104], the simultaneous iterative reconstruction technique (SIRT) [105], Krylov subspace methods [106], the Gauss-Newton method [107], and so on. As mentioned, measurement data vector b almost always contains errors resulting from practical circumstances. Small errors for b result in huge deviations for solutions of x. One theoretical strategy to minimize this instability in numerical solutions is called regularization. First, the linear system Equation (3.12) also can be solved by a least-square minimization:

$$x = \text{argmin}(\|Wx - b\|^2) \tag{3.14}$$

Equation (3.14) tries to find a solution x that satisfies the minimization of residuals between Wx and b. The most commonly used regularization method is the Tikhonov regularization method:

$$x = \text{argmin}(\|Wx - b\|^2 + \lambda\|x\|^2) \tag{3.15}$$

As shown above, the Tikhonov method attempts to minimize a linear combination of the residual and a weighted norm of the solution x. λ represents the regularization parameter existing in many optimization methods. It has an important influence on reconstruction quality, since it controls the balance between a regularized solution and measurement data consistency. There are several strategies proposed in the literature to determine the best trade-off value for λ [108], such as the generalized cross validation method (GCV) [109] and the discrepancy principle (DP) method [110]. One common method, the L-curve [111, 112], logarithmically plots the regularization term $\|x\|^2$ versus the data residual term $\|Wx - b\|^2$ with respect to the parameter λ. This plotted line is L-shaped. If λ is too large on this curve (signifying that the regularization became overwhelming), it may result in an over-smoothed solution for the linear equation. On the other hand, a very small value for λ alerts those artifacts are serious in the solution. Therefore, the optimal parameter for regularization is located at the corner of the whole curve.

Introducing prior information into Equation (3.14) improves fluorescence tomography reconstruction. Many strategies can furnish prior structure information, such as X-ray computed tomography (XCT), magnetic resonance imaging (MRI), or any other structural imaging modality. To introduce this prior information into this regularization equation (3.14) and to improve reconstruction quality, a regularization matrix L is formed into the formula. The matrix penalizes the variance of individual voxels:

$$x = \text{argmin}(\|Wx - b\|^2 + \lambda\|Lx\|^2) \tag{3.16}$$

Containing different types of prior values in regularization matrix L, which is an invertible square diagonal matrix with size, leads to different kinds of regularization methods. For instance, when $L = I$ the regularization matrix equals the identity

matrix and Equation (3.15) changes to the Tikhonov regularization, which does not depend on structural priors. For optical tomography reconstruction, a Laplacian regularization termed as structured priors has been proposed [113, 114]. The Laplacian regularization matrix L is given as:

$$
L = \begin{bmatrix} L_1 & 0 & \cdots & 0 \\ 0 & L_2 & \ddots & \vdots \\ \vdots & \ddots & \ddots & 0 \\ 0 & \cdots & 0 & L_n \end{bmatrix}
\tag{3.17}
$$

By assuming tissue volume is comprised of n regions and every region contains N_k voxels or elements, the sub-matrix L_k in (3.17) is expressed as:

$$
L_k^{i,j} = \begin{cases} 1 & i = j \\ -\dfrac{1}{N_k} & i \neq j \end{cases}
\tag{3.18}
$$

This Laplace prior regularization enforces smoothness within the segmented region and keeps differences close to each region boundary [86]. There are also some data-driven methods to calculate this segmentation weight matrix. Hyde et al. [115] proposed one weight estimation strategy relying on two-step reconstructions. First, a low-resolution inversion was calculated by reducing one dimension of the identity weight matrix L from the voxel number size to the segmentation region number size; this step calculated the relative fluorescence intensity in each segment region. Then, the second inversion was solved using a full size weight matrix (which was estimated by the expected segmentation region distribution results) in order to find a spatially varying regularization matrix. Karin et al. [116] introduced a variation of Hyde et al.'s method. They first estimated an optimal regularization parameter, λ, where the regularization was high enough to suppress surface artifacts. Then, the mean reconstructed fluorescence intensity from the first-step inversion was normalized to values between 1 and 3 proportionally and applied into the corresponding component of matrix L.

Before introducing this study's method, note that Equation (3.16) also can be written as:

$$x = \min \left\| \begin{bmatrix} \widetilde{W} \\ \lambda I \end{bmatrix} \tilde{x} - \begin{bmatrix} b \\ 0 \end{bmatrix} \right\|^2 \tag{3.19}$$

Where, $\tilde{x} = Lx$ and $\widetilde{W} = WL^{-1}$. Equation (3.19) is also called the "damped least-squares" problem, and it counts into the regularization matrix L and parameter λ.

Since matrix $\widetilde{W}$ is sparse and large scale, it is taxing on time and memory to invert Equation (3.19) directly with explicit methods. Thus, computing the fluorescence tomography requires iterative methods. Here, this study introduces an iterative method: the so-called LSQR algorithm [117, 118]. While analytically similar to the standard conjugate gradients methods, it is more efficient and less memory consuming for applications to least-squares problems like Equation (3.19). The LSQR method generates a series of approximations $\tilde{x}_k$ and decreases the residual norm $\left\| \widetilde{W} \tilde{x}_k - b \right\|^2$. For the specific ill-posed problem (3.19), the LSQR algorithm is semi-convergent, which means that the optimal solution will be estimated after only a few iterations and will degrade from system noise without manually stopping the iterations. There are two main separate steps for the entire numerical LSQR method. First, by using the Lanczos process [119], the new weight matrix $\widetilde{W}$ is transformed into a bi-diagonal matrix. Second, QR factorization solves the inversion equation using Givens rotations [120]. A summary of the LSQR method now follows here, while a detailed derivation and the entire algorithm can be found in [117].

The solution for the least-squares problem in Equation (3.19) is known to satisfy the augmented matrix system:

$$\begin{bmatrix} I & \widetilde{W} \\ \widetilde{W}^T & -\lambda^2 I \end{bmatrix} \begin{bmatrix} b - \widetilde{W}x \\ x \end{bmatrix} = \begin{bmatrix} b \\ 0 \end{bmatrix} \tag{3.20}$$

The Lanczos process generates a series of vectors, u_k and v_k, and scalars, α_k and β_k, before matrix $\widetilde{W}$ is reduced to a bi-diagonal matrix. After applying the Lanczos process to the particular symmetric system, after $2k + 1$ iterations, Equation (3.20) can be reformulated as:

$$\begin{bmatrix} I & B_k \\ B_k{}^T & -\lambda^2 I \end{bmatrix} \begin{bmatrix} t_{k+1} \\ y_k \end{bmatrix} = \begin{bmatrix} \beta_1 e_1 \\ 0 \end{bmatrix} \tag{3.21}$$

Where,

$$
\begin{cases}
\beta_1 u_1 = b \\
\alpha_1 v_1 = \widetilde{W}^T u_1 \\
\beta_{k+1} u_{k+1} = \widetilde{W} v_k - \alpha_k u_k \\
\alpha_{k+1} v_{k+1} = \widetilde{W}^T u_{k+1} - \beta_{k+1} v_k \\
t_{k+1} = \beta_1 e_1 - B_k y_k
\end{cases}
\tag{3.22}
$$

And,

$$
B_k =
\begin{bmatrix}
\alpha_1 & & & \\
\beta_2 & \alpha_2 & & \\
& \beta_3 & \ddots & \\
& & \ddots & \alpha_k \\
& & & \beta_{k+1}
\end{bmatrix}
\tag{3.23}
$$

Here, B_k is $(k+1) \times k$ and a lower bi-diagonal matrix. The solution to Equation (3.21) is also the same solution with another projected damped least-squares problem:

$$
\min \left\| \begin{bmatrix} B_k \\ \lambda I \end{bmatrix} y_k - \begin{bmatrix} b \\ 0 \end{bmatrix} \right\|^2
\tag{3.24}
$$

Orthogonal transformations can solve problem (3.24). In LSQR, QR factorization solves it through a Givens rotation:

$$
Q_k \begin{bmatrix} B_k & \beta_1 e_1 \\ \lambda I & 0 \end{bmatrix} = \begin{bmatrix} R_k & f_k \\ 0 & \overline{\emptyset}_{k+1} \end{bmatrix} =
\begin{bmatrix}
\rho_1 & \theta_2 & & & & \emptyset_1 \\
& \rho_2 & \theta_3 & & & \emptyset_2 \\
& & \ddots & \ddots & & \vdots \\
& & & \rho_{k-1} & \theta_k & \emptyset_{k-1} \\
& & & & \alpha_k & \rho_k & \emptyset_k \\
& & & & & & \overline{\emptyset}_{k+1}
\end{bmatrix}
\tag{3.25}
$$

Above, Q_k is a product of a series of rotations to eliminate λ and β_i. With Equation (3.25), the solution of inversion fluorescence tomography can be found by:

$$
x_k = V_k R_k^{-1} f_k
\tag{3.24}
$$

This study modified the implementation code of the LSQR method originally programmed at MATLAB (The MathWorks Inc., Natick, MA) by Damon Hyde.

3.4 Multimodality system FMT-XCT

Although standalone FMT has developed over many years and its resolution and sensitivity have improved significantly, a state-of-the-art FMT system is still far from accurately reconstructing fluorescence distribution in biological tissue. As discussed in Section 3.3, incorporating prior information into a regularization matrix L can solve the inversion of the FMT system equation more accurately. Anatomical tissue structure from an MRI [121] or an XCT [85] can provide this prior information. This study's system incorporated XCT modality since it is economically and spatially more efficient. There are four advantages of applying the XCT anatomical modality information into the system and inversion reconstruction. First, an XCT projection image could optimize the FMT data acquisition process. Figure 3.1 (a) shows one XCT fluoroscopy for a live mouse during the data collection procedure of one FMT-XCT *in vivo* experiment. The bright green line in the image's center shows the center of mouse; this line was calculated automatically by FMT data acquisition software. Red dots with green crosses display all source locations on the mouse that were determined around a green centerline. Red dots without green crosses indicate that the laser was too close to the mouse boundary, and these laser locations were eliminated. Second, a high-resolution XCT reconstruction can present a three-dimensional geometry of the mouse sample employed for FMT reconstruction mesh generation. The example in Figure 3.1 (b) illustrates one mesh of a subcutaneous tumor mouse model, generated from the mouse geometry acquired by XCT reconstruction. This particular mesh was used for FMT reconstruction based on the FEM method. Third, the interior anatomical information of the biological sample from XCT reconstruction and segmentation can also be utilized for helping FMT reconstruction, because it provides different optical parameters for various segmentation organs or regions. Co-registered XCT mouse data may also deliver the interior structure of the mouse volume and introduce the regularization matrix into the inversion equation (as Section 3.3 discusses). Fourth, the integrated three-dimensional (3D) results of fluorescence tomography from the FMT inversion and structural information from the XCT reconstruction could contribute a more straightforward display for biological researchers by detailing fluorescence origination signal strength. Selected 3D results will be shown later in this study. Overall, high-

resolution anatomical information offered by XCT, which combines high-sensitivity tissue fluorescence contrast from FMT, can yield a hybrid system that, when compared with a standalone FMT system, enormously improves fluorescence tomography.
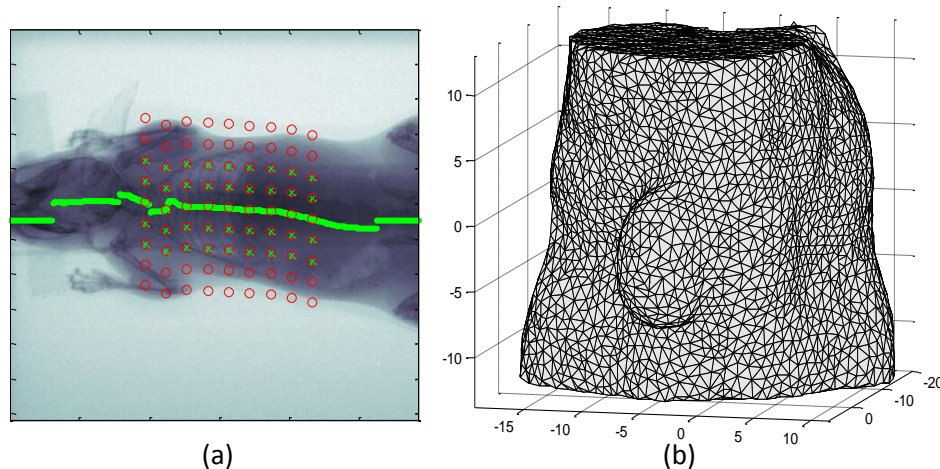

(a)   (b)

Figure 3.1. XCT modality helps the FMT system and inversion. (a) represents an XCT projection of a live mouse marked by red dots and green crosses. (b) displays one mesh generated from an XCT-reconstructed 3D volume for a subcutaneous tumor mouse model.

To overcome all the limitations of a standalone FMT system, a combination system—FMT with X-ray computed tomography (XCT)—was developed at our institute (Institute for Biological and Medical Imaging (IBMI) at the Helmholtz Zentrum München (HMGU)) [86]. It is named the hybrid FMT-XCT system. The hybrid system was developed by incorporating the $360°$ free-space FMT system into commercial micro-CT eXplore Locus XCT equipment (GE HealthCare, London, ON, Canada). Figure 3.2 illustrates the system's outer and interior. This section introduces the hybrid system. The XCT scanner includes one X-ray illumination source and one X-ray detector. Roughly one meter of lead wraps the entire eXplore Locus scanner. The illumination source projects X-rays through a filter and transmits the sample onto the X-ray detector. The X-ray detector consists of a scintillator, which converts the X-rays into visible light, and a CCD camera, which captures the optical image. This cone-beam XCT can scan the complete body of a small animal at resolutions of 45 μm or 90 μm. A lead cube also shields the X-ray source to safeguard X-rays from the FMT component, which is shown in Fig. 3.2. The FMT component consists of four parts. First, two diode laser sources (B&W Tek, Newark, DE, USA) with a wavelength of 680 nm and 750 nm, respectively, paired with two optical fibers coupled to two separate optical collimators.

The collimators focus the laser light into a point as small as possible and shoot onto the specimen. Second, the collimators are fixed onto the electromechanically controlled linear stages (Thorlabs, Newton, NJ, USA). The stage can move along the x-y axis freely, which absorbs the focused laser that shoots in different locations on the surface of the specimen, as displayed in Figure 3.1(a). Third, before the transmitted laser light reaches the CCD camera, one filter wheel is positioned before the camera. Different combinations of long-pass filters and band-pass filters (Andover, Salem, NH) were fixed into the wheel to filter out the excitation light for fluorescence images or filter out the fluorescent wavelength light for excitation images. Fourth, a back-illuminated cooled CCD camera (Princeton Instruments, Trenton, NJ), which is coupled with a 50 mm lens (Carl Zeiss, Oberkochen, Germany), captures and records all the excitation and emission (or fluorescence) images.
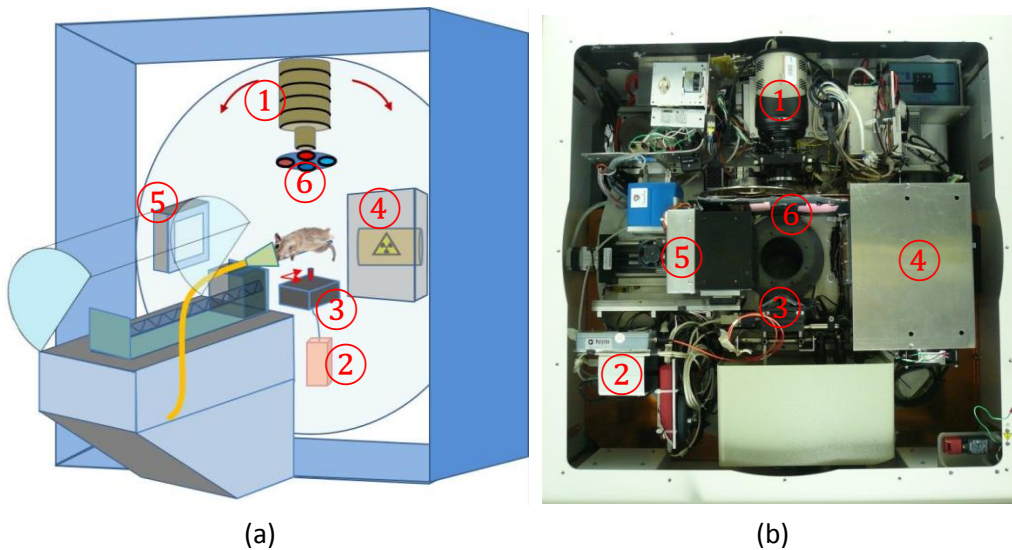

(a)   (b)

Figure 3.2. The hybrid FMT-XCT imaging system. (a) illustrates a schematic view of the system. (b) is a physical photograph of the system's interior [86]. In both, important components are labeled: 1 = scientific cooled CCD camera, 2 = CW laser sets, 3 = laser source translation stage, 4 = X-ray illumination source, 5 = X-ray flat panel detectors, and 6 = optical filter wheel.

X-ray computed tomography modality and FMT modality are positioned vertically onto a rotating gantry, which can rotate $360°$ freely. The sample can be placed on an epoxy bed, shown in Figure 3.2 (a), where it can hold the tissue-like phantom or mouse in order to transfer the sample along the translation stage into the FMT-XCT system for precise positioning. After affixing all components onto the $360°$ rotating gantry, the next step is to calibrate the system and ensure that the optical FMT unit and XCT unit match geometrically. A mathematical pinhole model performed the

system's coregistration calibration [122]. Using a silicon cylinder phantom marked with a black-tape grid, both calibrations—the camera calibration and the source calibration—calculated the correct parameters between the optical FMT coordinate and the XCT coordinate. A self-programmed LabView code (National Instruments, Austin, TX, USA) controlled all components of the FMT-XCT imaging system. During *in vivo* mouse experiments, the mouse was anesthetized with Isoflurane using a tube (the yellow one in Figure 3.2 (a)) connected to a Sigma Delta system (Penlon Inc., NB, UK).

3.5 Multimodality FMT-XCT data collection

For data acquisition, the hybrid FMT-XCT dataset includes two separate parts: XCT raw data and FMT raw data. Since this study utilizes a normalized Born approximation method for the inversion of fluorescence tomography, collection required both the excitation wavelength optical data and the fluorescence wavelength data. The FMT and XCT raw data are acquired separately, but the specimen is kept fixed in one position throughout the data collection procedures.
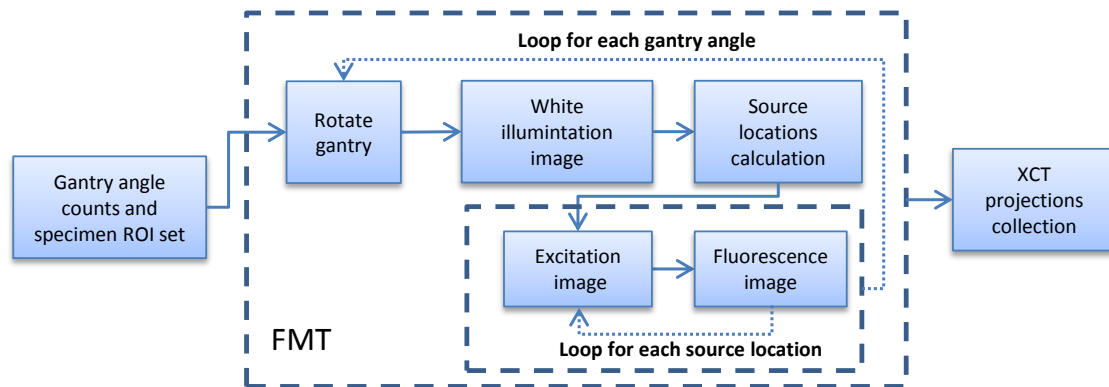

Figure 3.3. Flowchart of FMT-XCT data acquisition methodologies.

Fluorescence molecular tomography raw datasets are collected from $360°$ and 18 gantry locations ($20°$ between each location). For each gantry angle, the CCD camera collected three sets of data sequentially for analysis. The first set was white-front illumination images using flat-sheet white light in the system. For each angle, the data collection software calculated between 20-50 laser-source locations (dependent on the geometry or size of the specimen) using either a white image (the FMT-XCT system in Helmholtz Zentrum München) or the corresponding XCT projection of that

angle (the system in Klinikum Recht der Isar, shown in Figure 3.1 (a)). The second set was excitation images recorded for each source location. Excitation images, here, result from filtering the fluorescence wavelength signal from the excitation filter set. During this process, the laser power was automatically set to its optimal value in order to acquire the best signal-to-noise ratio (SNR) of each image data. The third set, emission fluorescence image data, was collected right after the excitation images by rotating the filter wheel to the fluorescence wavelength filter set. The laser power was also set optimally. The total scan time for the FMT part is around one hour, but greatly depends on specimen size, laser source location counts, and fluorescence intensity inside of the specimen. The size of each FMT image—whether a white image, an excitation image, or a fluorescence image—is high-resolution with a size of 512×512 in SPE format (Princeton Instruments, Trenton, NJ, USA). The setup also generates another FMT file that includes all of the FMT data collection information: geometry information for system calibration, the rotation center coordinate, the rotating angle degree, laser source location coordinates, the integration time for each excitation and emission image, and the maximum intensity of each excitation and emission image. Subsequent FMT-XCT reconstruction utilizes these parameters.

X-ray computed tomography raw data, known as projections of the imaged sample, are also collected before (the FMT-XCT system at the Klinikum Recht der Isar) or after (the FMT-XCT system at the Helmholtz Zentrum München) FMT data acquisition. A typical XCT data set includes 400 projections for each specimen, with a high resolution of 1750×914 in VFF file format (Sun Microsystems, Inc., USA). Figure 3.3 depicts the flowchart of the whole FMT-XCT data collection procedure.

An *in vivo* small animal study requires some specific preparation work before placing the animal onto the specimen bed. Before experiments, infrared imaging agents should be administered into the mouse intravenously or intraperitoneally (depending on the mouse model and the commercial fluorescent agent instructions). The agent type ultimately conditions the injection time, and ranges from one hour (intravenous) to one day (intraperitoneal) before imaging can commence. Sometimes, to improve XCT projection contrast and reconstructed 3D quality, XCT contrast agents are also prepared around one hour before experimentation.

3.6 Multimodality FMT-XCT data processing

All FMT raw data and XCT projection raw data are stored and processed by self-programmed software. Figure 3.4 shows the complete flow of the data processing procedure. X-ray computed tomography projections are processed for 3D reconstruction by a wrapped application from GE (evsbeam.exe) and MATLAB programming. It generates a 3D data VFF file that is performed for segmentation. Segmentation can be carried out semi-automatically or manually. The commercial software Amira (Visage Imaging, Richmond, Australia) assists manual segmentation, which may be necessary since the automatic segmentation software might dysfunction if the 3D XCT data contains low contrast between different tissue regions. Under *in vivo* study conditions with the help of an XCT contrast agent (e.g., the ExiTron nano 12000 (Miltenyi Biotec GmbH, Bergisch Gladbach, Germany)), the 3D CT result can be reconstructed with high contrast and high resolution, which makes segmentation of most of the small animal's organs possible. This detailed segmentation can significantly improve later FMT inversion in two ways. Firstly, specific optical properties can be assigned to the corresponding organ, which can optimize the forward problem calculation. Secondly, as discussed in section 3.3, different organs can be used for constructing regularization matrix L. After XCT reconstruction and segmentation, the geometry of the specimen is extracted and discretized into a tetrahedral mesh. The average edge size of the mesh is around 1.3 mm in order to maintain a balance between FMT reconstruction accuracy and the time and memory costs of the inversion problem. When choosing the Region of Interest (ROI) of the mouse from a white illumination image in a typical *in vivo* small animal model study, the generated mesh elements are around 50,000-75,000 elements and the mesh nodes are around 10,000-15,000. As Section 2.5 introduced, the produced mesh is prepared for solving the forward problem. The information included in the FMT acquisition file is also used to normalize the dataset and to organize forward model calculation. The forward model was performed for calculating the weight matrix W by assigning various optical properties into different organs' meshes previously generated by XCT segmentation.

A Born ratio of fluorescence images and excitation images calculates measurement data vector b. All fluorescence images and excitation images are background subtracted initially, which is called pre-processing. Then, a detector point grid is generated after choosing the specimen's ROI. Some detector points on this grid are removed because these points may emerge from the specimen bed bars or from the place very close to the boundary of the specimen. Either situation indicates that the

detected fluorescence signal or excitation signal on these points are over-saturated or inaccurate for a Born ratio calculation. After removing the defective points from the detector grid, both the two-dimensional source point grid and the detector grid are mapped onto the surface nodes of the 3D volume of the specimen using a ray-tracing approach and the calibration matrix previously explained. Then, the Born ratios of emission fluorescence image intensity and excitation intensity (for each source detector pair from all source locations of every gantry angle) are calculated and ordered identically with the mesh nodes' order.
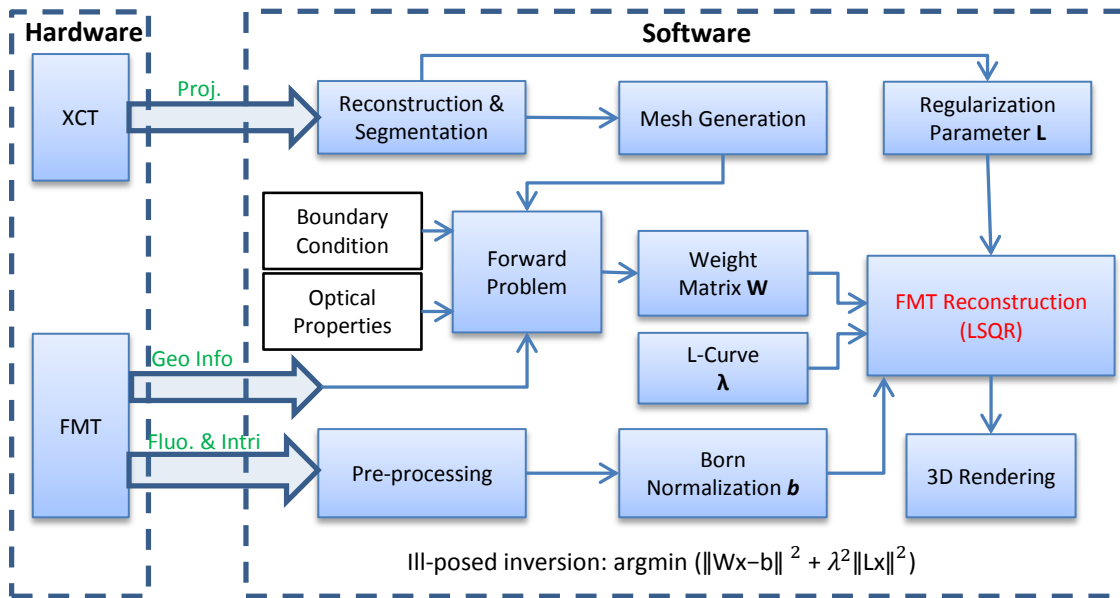

Figure 3.4. Flowchart of the FMT-XCT data processing strategy. The dashed box on the left is the hardware, and the right-hand one is the software flowchart.

Two parameters remain before inversion of fluorescence tomography: the regularization matrix L and regularization parameter λ. In this study, as explained in Section 3.3, the L-curve method determines optimal λ. To ensure optimal reconstructed fluorescence distribution, several choices of λ around the L-curve corner are compared to find the ideal value. Although multiple strategies for calculating the regularization matrix L exist, these methods are not consistently accurate. Thus, in this implementation study, the elements of regularization matrix L are manually set to 1 for all different organ parts. For cases of ROI-specified fluorescent distribution (i.e., the lung region is the ROI in a lung tumor model study), the corresponding weights for the specific ROI region nodes on the diagonal of the regularization matrix are manually set to 4, and the remaining nodes' weights are manually assigned to 1. This manual weight-setting strategy can improve fluorescence tomography accuracy. The disadvantage of this method is it would exclude some

other fluorescent sources in biological tissue, such as tumors outside of the lung region in lung tumor study case.

For an *in vivo* study, optical properties are important to the inversion of FMT-XCT, because they influence the forward model calculation. After segmentation of different organs from an XCT-reconstructed result, distinct properties will be assigned to different organs for FMT-XCT inversion. To compare all the reconstructed results, this study consistently employed identical optical properties for all mice involved, as shown in Table (3.1). Hyde et al. [123] proposed this approach in 2009.

Table 3.1. Optical properties for different organs used in this work.

Value (cm^{-1})	Tissue	Bone	Lung	Heart	Liver
μ_a	0.3	0.1	0.25	0.35	0.5
μ_s^{-1}	10	20	30	23	13

3.7 An FMT-XCT application example

This section explains the FMT-XCT code and data processing for a cylinder phantom demonstration experiment. The same procedure as in Section 2.5 characterizes this silicon phantom. The size of the cylinder phantom is 80 mm in length with a 20 mm diameter, as displayed in Figure 3.5(a). It contains two symmetrical holes used to insert two small tubes containing a probe of dyes Alexa 680 Fluor and Alexa 750 Fluor (Thermo Fisher Scientific, WA, USA). This setup assumes Alexa 750 Fluor as a background noise and focuses on reconstructing the fluorescence tomography from source Alexa 680 Fluor. The 680 nm setup—a 680 nm laser in the FMT system with corresponding excitation and emission filter sets—collected all FMT data. As explained, FMT raw data (containing a white illumination image and all of the excitation and fluorescence images) and XCT raw projection data are acquired for processing. Eighteen gantry angles with around 30 laser point locations for each angle, as shown in Figure 3.5 (b)-(d) with red dots for one gantry angle, were determined manually for FMT data acquisition. Figure 3.5 (b)-(d) shows one typical FMT data pair: 3.5 (b) displays one emission image with laser illumination from the other side of the view, marked by a yellow star. This emission image is superimposed on the white image

from this gantry angle. All red dots in this figure illustrate all laser locations used in this angle, including those illuminated from the backside. Green dots show the corresponding detector points selected. Two thick red lines mark the ROI for FMT-XCT reconstruction. In Fig. 3.5 (b), there is a red region on the right side of the image that shows the stronger fluorescence signal intensity region compared to other parts of the image. Experimenters speculate that the Alex 680 tube is near the right side of this image. Figure 3.5 (c) presents the excitation image from same angle superimposed on the white image. The red region in this figure is more uniform and dispersed, because the laser was shooting from an almost symmetrical location to the phantom. Figure 3.5 (d) shows the Born ratio image of figures 3.5 (b) and 3.5 (c) multiplied by a correction factor calculated by data collection information (e.g., integration time and laser power for each image). Clearly, the red region (the high-intensity region) in this figure is still close to right side.
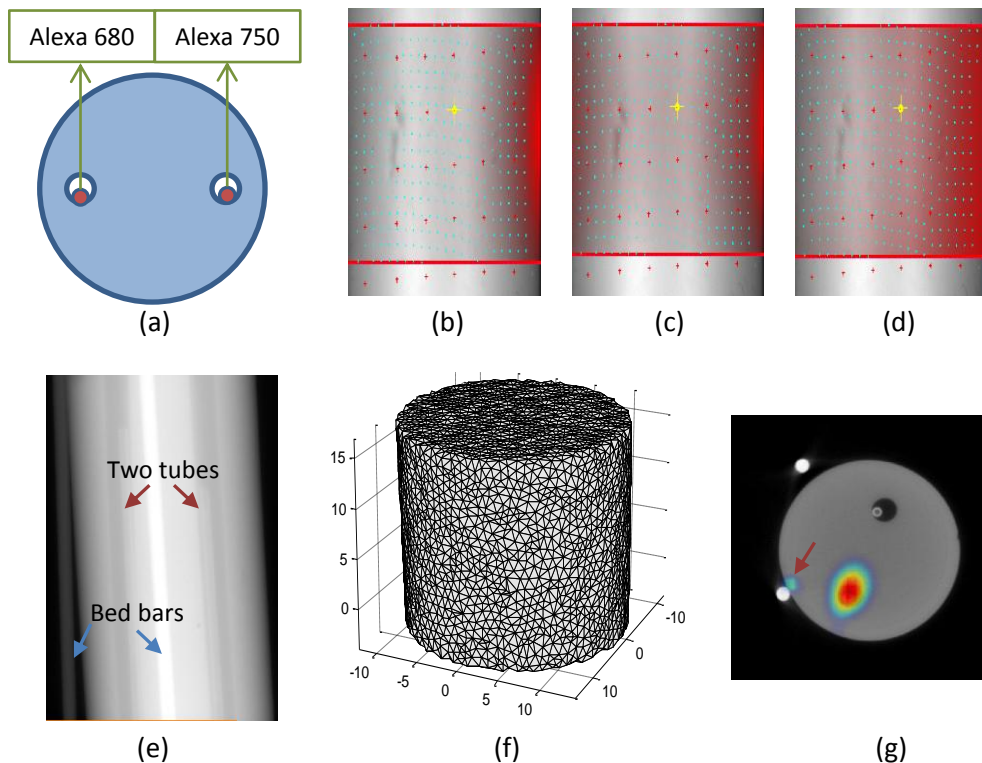

Figure 3.5. The cylinder silicon phantom FMT-XCT experiment illustrates the complete data processing procedure. (a) shows a schematic diagram of the phantom cross-section: the phantom with two holes and tubes containing fluorescence probes Alexa 680 and Alexa 750. (b) illustrates one sample fluorescence image imposed on the white image, where a yellow cross marks the corresponding laser source location. Red dots indicate all source locations, and green dots show detectors. The two red lines

display the ROI. (c) is the corresponding excitation image overlapped onto the white image. (d) depicts the Born ratio image of (b) and (c) overlapped onto the white image. (e) shows one typical XCT projection of raw data. (f) exhibits the code-generated mesh for this phantom. (g) shows one cross-sectional view of the FMT-XCT reconstruction result.

Figure 3.5 (e) displays a typical XCT projection of raw data from this cylinder phantom collected by the FMT-XCT system. Two blue arrows in this image point out the thick black line and the thick white line that illustrate the two epoxy black bars of the specimen bed. The left bar is black because it is outside of the phantom projection region. The Figure's two red arrows signal the two holes in the phantom. The tubes in these holes are even observable with reduced contrast. Figure 3.5 (f) shows the tetrahedral mesh for the cylinder phantom generated by the FMT-XCT reconstruction code with an average edge size 1.16 mm. This mesh was used in forward model calculation. Figure 3.5 (g) shows a cross-section of the reconstructed FMT-XCT fluorescence tomography. The elliptical coloring at the lower part of the image depicts the reconstructed fluorescence distribution superimposed on the corresponding transverse plane from the XCT 3D image. Note that a small colorful stain close to one of the specimen bed bars, which is white spot in the figure. Noise from the specimen bed generates this colorful stain because the black bars reflect light, which means they have a higher intensity in the Born-ratio image compared to the phantom region. Even when removing some detector points on and around the bars for select gantry angles, it is impossible to remove them for all gantry angles since the bars are behind the image at some angles.

There are a few important facts that this phantom experiment demonstrates. The reconstructed 3D XCT result is $576 \times 576 \times 457$. After choosing the ROI region, which is around 20 mm in length along the cylinder phantom, there are 110,168 source-detector pairs for all of the 18 gantry angles. The number of pairs means that the size of measurement vector b in the inversion problem (Equation 3.16) is 110168×1. The generated mesh for this ROI contains 18,049 nodes and 99,730 tetrahedral elements or voxels, which means that the size of the original weight matrix is 110168×18049. The XCT anatomical reconstruction took around 50 minutes for 400 projections of raw data. The whole inversion process consumed 527.75 seconds after imputing all FMT and XCT 3D data. MATLAB Profiler analyzed the entire reconstruction process on a computer with an Intel Core 2 Duo CPU @3.00GHz and 8GB RAM. The most time-consuming function of the total fluorescence tomography was solving the forward model, which consumed 256.7 seconds and accounted for almost half of the entire process. The LSQR inversion method took 93.1 seconds, around 20% of total inversion

time. The L-curve calculation consumed 40.6 seconds, 7.5% of whole inversion. The remaining 20% of time was consumed by other functions, such as volume extraction, mesh generation, preconditioning matrix building, and so on.

3.8 XCT modality performance

It is worth mentioning that a high-resolution XCT contrast agent makes it possible to track and evaluate lung tumor progression through XCT solo modality, both in preclinical biological research and in clinical study [124-127]. To validate this study's built-in XCT performance, a high-resolution XCT experiment follows, with the help of an XCT contrast agent, to evaluate nodule progression in a longitudinal observation lung tumor mouse model.

One study found extensive amplification of the anti-apoptotic gene myeloid cell leukemia 1 (Mcl-1) for cell survival in human lung cancer and other cancers [128]. Myeloid cell leukemia 1 inhibition significantly reduced proliferation in lung cancer cells and inhibited growth of xenograft tumors in mice. Further, the compound ABT-263 is an inhibitor of small-molecule anti-apoptotic BCL-2 [129]. The aim of this study's experiment is to verify that ABT-263 combined with a low expression of Mcl-1 triggers tumor regression in non-small cell lung cancer (NSCLC) by using XCT imaging modality [130].

This experiment prepares one widely used mouse model of NSCLC, $Kras^{G12D/+}$, as a control group. The other group is a $Kras^{G12D/+}$ mouse with the $Mcl-1^{fl/+}$ gene knocked out [131]; this group also treated by compound ABT-263 (100mg/kg daily by oral administration) for two weeks. There are three observation time points. First is before ABT-263 administration, which establishes baseline imaging. Second is after two weeks of ABT-263 administration, set as early response imaging. Third is two weeks after administration ended, which is four weeks after baseline imaging, set as overall response imaging.

The Micro-CT component of this study's hybrid FMT-XCT system scanned all of the small animals with a source voltage of 80 kVp, a current of 450 μA, and an exposure time of 2,000 ms. Four hundred projections were acquired in about 20 minutes. One hour before each imaging, XCT contrast agent eXIA 160 (Binitio Biomedical, Inc., Ottawa, ON) was intravenously injected into the mouse to enhance distinction between tumors and air in the lung. Commercially available software from GE was

used for XCT reconstruction for each time point of each mouse. Commercial software Amira (Visage Imaging, Richmoud, Australia) performed segmentation and 3D rendering. The reconstructed data stack $576 \times 576 \times 457$ was read through individually to find the interested tumor nodule for tracking. Then, by segmenting every slice including this nodule, Amira can calculate the total tumor size. Amira also conducted a 3D rendering of one nodule location inside of the lung using the final time point XCT data set.
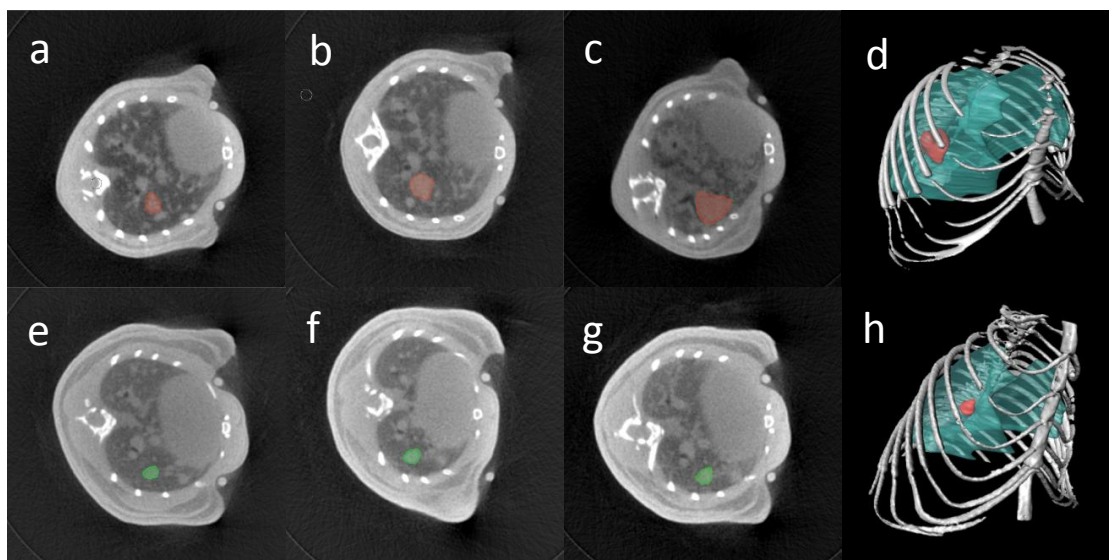

Figure 3.6. Lung cancer mouse model's individual nodule tracking for demonstration of high-resolution XCT performance. (a)-(c) show transverse images from XCT reconstruction 3D results of one typical $Kras^{G12D/+}$ mouse from the control group. (a) is the baseline image. (b) is the early response image. (c) is the overall response image. (d) depicts the 3D rendering of the tumor's location for the control mouse. (e)-(g) are corresponding transverse images for $Kras^{G12D/+}\&Mcl-1^{fl/+}$ mouse. (e) is the baseline image (before administration of inhibitor ABT-263). (f) is the early response image for the two-week nonstop daily administration of ABT-263. (g) is the overall response image (two weeks after administration stopped). (h) shows the 3D rendering for the inhibitor administration mouse and indicates nodule location.

Figure 3.6 illustrates one typical comparison result between two mice from the control group and the administration group, respectively. Images Fig. 3.6 (a)-(c) show transverse visualizations from one mouse in the control group. Fig. 3.6 (a) indicates the baseline image (0 week), Fig. 3.6 (b), is the early response time point image (two weeks), and Fig. 3.6 (c), from the overall response time point image (four weeks), demonstrate the stages of cancer proliferation in the NSCLC $Kras^{G12D/+}$ mouse

model. To display the location and size of this chosen nodule, Fig. 3.6 (d) shows a 3D rendering from the final time point of this control mouse. Figures Fig. 3.6 (e)-(h) depict the corresponding images for one representative mouse from the $Kras^{G12D/+}\&Mcl-1^{fl/+}$ model combined with inhibitor ABT-263 administration group. By comparing Fig. 3.6 (a)-(c), one observes that without eliminating the Mcl-1 gene and administration of the inhibitor, the selected nodule doubles after two weeks and quadruples after four weeks. On the contrary, in the $Kras^{G12D/+}\&Mcl-1^{fl/+}$ plus inhibitor group, the tumor proliferation is apparently controlled when compared with images Fig. 3.6 (e)-(g). Clearly, the contrast enforcement agent eXIA 160 enhances contrast between different tissues in the thorax region. Clear boundaries for all organs in this region, such as heart, bone, lung, and lung tumor, can be found easily in every transverse image of the XCT reconstruction, which helps in accurate segmentation and estimation of an individual nodule of NSCLC. This will also help segmentation for other *in vivo* studies of the thorax region, and improve the FMT-XCT reconstruction quality.

3.9 FMT-XCT reconstruction validation – cryoslicing and histology

As introduced before, the FMT-XCT system can track or detect a fluorescence-marked tumor or other diseases in a mouse model by *in vivo* method. To validate the performance of *in vivo* experiments' (reconstructed fluorescence distribution calculation) by the FMT-XCT system and reconstruction code, we compare the reconstructed result with the *ex vivo* imaging modality, which is referred to as a planer cryoslicing imaging system [132]. Ex-vivo cryoslicing (considered the gold standard) offers high-resolution colored and fluorescent cross-sectional images of a small animal. The system was built by setting up a planer two-dimensional multispectral imaging system within a cryostat system. The two-dimensional epi-illumination imaging system consists of a white light source and filter wheels placed in front of a CCD camera. The filter wheels contain various sets of filters for different excitation and emission wavelengths. The whole system is also controlled automatically by a programmed Labview interface and code.

After each FMT-XCT imaging, the mice were euthanized and embedded into a mixture of optimal cutting temperature medium (O.C.T.) and India ink. Then, it was frozen to -50°C and submitted for whole-body cryoslicing. There are three types of images for each slice of the specimen after selecting the correct wavelength: a white-light RGB

image, an excitation wavelength image by an excitation filter, and a corresponding fluorescence image by an emission filter. Fluorescence images were acquired and employed for validation of the *in vivo* findings.

There are other histological strategies for validating FMT-XCT reconstruction results, such as H&E staining. A detailed explanation will be introduced later for specific application with the FMT-XCT system.

3.10 Conclusion

This chapter, which began with the ill-posed FMT inversion equation, brought out the hybrid FMT-XCT system. By incorporating prior anatomical structural XCT modality information into an FMT system and reconstruction, more accurate and robust fluorescence reconstructions can be achieved. Since FMT inversion is ill-conditioned, we introduced the least-square regularization method for inversion. To solve the Tikhonov regularization equation, a stable and iterative algorithm (referred to as LSQR) was applied for the hybrid FMT-XCT inversion. X-ray computed tomography segmentations provided values for regularization matrix L, called a penalty matrix. Other groups have developed a few strategies for building a penalty matrix. In this thesis, the matrix was generated manually after segmentation of different organs. A detailed explanation of the FMT-XCT system was elaborated, which reflects the core focus of this work. The account included the multimodality machine, the data collection strategy, and the data processing procedure. The Born ratio approximation method was also introduced as a part of the FMT-XCT inversion. Two FMT-XCT experiments were performed to demonstrate the performance of the system and the inversion code. One experiment, with a typical tissue-like cylinder phantom containing a fluorescence probe, confirmed the FMT-XCT's high performance. With the help of an XCT contrast agent, the standalone XCT imaging modality could also trace selected specific nodule progression in an NSCLC mouse model experiment. A gold-standard *ex vivo* multispectral two-dimensional imaging modality was also presented at the end for validation of FMT-XCT reconstructed fluorescence distribution. After explaining all key facts of the FMT-XCT system, subsequent chapters will utilize the system for specific biological application in the thorax region.

4 Quantitative evaluation of asthmatic inflammation by FMT-XCT

4.1 Introduction

Asthma is a chronic lung disease affecting millions of people across the world. Bronchial hyper-responsiveness (BHR), airway inflammation, and airway remodeling are key symptoms that characterize the disease [133-136]. Chronic airway inflammation involves the recruitment of inflammatory cells, such as T lymphocytes, mast cells, and eosinophils. Among all asthma-related inflammatory cells, eosinophils predominate and are well known to produce various proteases in asthma, including cathepsins B, S, L, H, and K, which are thought to contribute to the pathogenesis of the asthma disease [137, 138]. Asthma models employ cathepsin activity as a biomarker of disease severity using near-infrared fluorescent agents [139]. Remodeling is commonly believed to occur as a result of the pathological repair of chronic airway inflammation processes [140]. Chronic airway inflammation involves structural changes in the airway's architecture in asthmatic patients, such as airway narrowing, wall thickening that results in airflow obstruction, and persistent BHR. The complex mechanisms behind the remodeling process are not fully understood [141]. Nevertheless, matrix metalloproteinases (MMPs) have been identified as enzymes that inflammatory cells and resident cells synthesize and produce [142]. Matrix

metalloproteinases are capable of degrading the extracellular matrix (ECM), and, therefore, play a critical role in remodeling [143, 144]. Elevated MMP expression has been associated with airway inflammation and remodeling [144].

An *in vivo* study of asthma and related drugs commonly involves mouse models [145]; however, animal measurements face limitations. A common drawback of many mouse models is tolerance development in animals exposed to the same allergen [146]. In those cases, an asthma phenotype reaches a peak in two or three days after a challenge, but the biological response drastically reduces within one to two weeks. To reduce this limitation, the Goplen group [147] describes an animal model of asthma that sustains the disease phenotype for at least three weeks by sensitizing a mice with a combination of three allergens relevant for human pathology: dust mites, ragweed, and aspergillus species (DRA) [147]. Besides sustaining asthma-related inflammatory responses over time, the DRA mouse model is capable of sustaining asthmatic features even after discontinuation of exposure to allergens [147].

The second limitation with small animal asthma research has been the ability to retrieve accurate longitudinal measurements of disease biomarkers. Traditionally, histological studies used for the evaluation of bronchial inflammation, airway obstruction, and remodeling involve animal sacrifice, which only allow for measurements at single time points. The requirement to assess disease progression or response to treatment has shifted attention to noninvasive technologies [148]. Spirometry is a long-known noninvasive technique [149] that estimates asthma severity by measuring inhaled and exhaled air volumes [149], but can result in overestimation and measurement uncertainty [150]. X-ray computed tomography (XCT) is a commonly used imaging modality to assess airway remodeling [151-153]. X-ray computed tomography identifies anatomical changes, but cannot visualize biological parameters associated with pulmonary inflammation [154]. Nuclear medicine is a noninvasive functional imaging technique used for asthma research [155]. Nuclear medicine provides suitable functional information, but suffers from short-lived signals of the radio-isotopes [156].

Optical methods also have been considered for asthma research. A limitation with commonly employed fluorescence epi-illumination imaging is its sensitivity to surface fluorescence activity, which visualizes signals in the lung unreliably [6]. Transillumination and tomographic techniques—in particular, Fluorescence Molecular Tomography (FMT)—have proven more efficient than epi-illumination fluorescence imaging when sampling biological processes in pulmonary diseases [139, 157, 158]. The ability to visualize pulmonary inflammation has been demonstrated using a

limited-angle FMT system in animal models of chronic obstructive pulmonary disease (COPD) [82]. Conversely, a standalone FMT is unable to provide high-fidelity functional information, due to strong photon scattering in tissue and the corresponding ill-posed nature of the inversion problem [159, 160]. The recent development of hybrid imaging, employing both FMT and XCT under a common rotating gantry, has shown significant improvements in the resolution and quantification achieved by the optical method [85]. This hybrid modality utilizes the XCT information for anatomical coregistration with the fluorescence images, which allows better orientation of the biological signals in relation to morphological landmarks [85, 116, 161]. Importantly, the XCT information is also employed as prior information into the FMT inverse problem, which improves overall accuracy and resolution by reducing the ill-posed nature of the inverse problem [85, 123, 162, 163]. Compared with previous FMT studies using limited angle projection illumination [82], the FMT-XCT system provides further 360-degree angle coverage that improves imaging fidelity. However, there has been no systematic evaluation of FMT-XCT in its ability to resolve asthma biomarkers in animal models. This work hypothesized that FMT-XCT could be ideally suited for asthma research studies due to its unique ability to combine anatomical and fluorescence-based biological contrast. In particular, this study investigated the performance of FMT-XCT when measuring pulmonary eosinophilias and MMP activity in a DRA mouse model.

4.2 Materials and methods

4.2.1 Asthmatic inflammation mouse model

The DRA chronic asthma model was chosen from among the large number of murine asthma models present in literature, because it maintains eosinophilic inflammation, remodeling, and other features of asthma for at least three weeks post-exposure to allergens [147]. Female Balb-C mice (7-8 weeks old) were purchased from The Harlan Laboratories (Indianapolis, IN, USA). For asthmatic groups, each mouse received an intranasal administration of 15μL of DRA allergen solution twice per week, using a 200μL pipette to reproduce the biological and molecular features of human chronic asthma. The 15μL DRA mixture solution was prepared using a 5μg dust mite in 5μL (extracts of *Dermatophagoides farinae*, Greer Laboratories, NC, USA), 50μg ragweed in 5μL (extracts of *Ambrosia artemisiifolia*, Greer Laboratories, NC, USA) and 5μg

Aspergillus in 5μL (extracts of *Aspergillus fumigatus*, Greer Laboratories, NC, USA). As Figure 4.1 shows, three experimental animal groups were established by means of DRA exposure (i.e., DRA exposure for six weeks, nine weeks, and nine weeks followed by three weeks of rest (12-week group)). The control mice received 15μL of saline using the same intranasal administration.
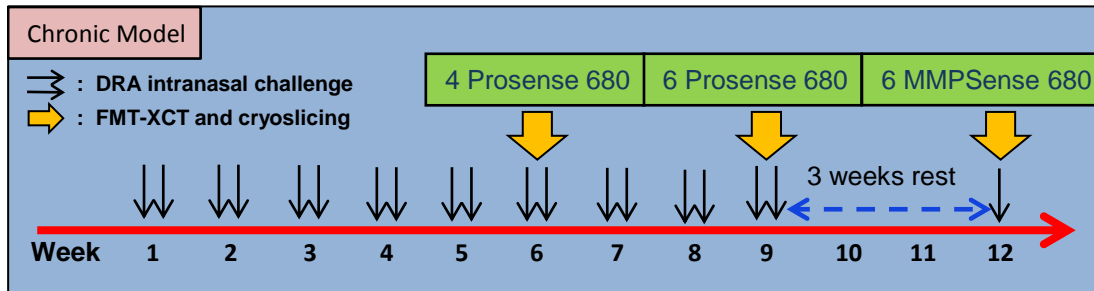

Figure 4.1. Schematic diagram of DRA-challenged chronic asthmatic mouse model and imaging strategies of FMT-XCT and cryoslicing.

4.2.2 Fluorescence imaging agents

Two different commercially available near-infrared imaging agents—namely, Prosense680 (Perkin Elmer, Waltham, MA, USA) activated by Cathepsin B and MMPSense680 (Perkin Elmer, Waltham, MA, USA) activated by MMPs—were intravenously administered prior to imaging studies. The excitation and emission wavelength of both imaging agents was approximately at 680 nm/700 nm. Around 2nmol of near-infrared imaging agent was injected into each mouse 24 hours prior to FMT-XCT *in vivo* imaging. The quantity of the injected imaging agent was calculated based on the body weight of each mouse. The Prosense680 dosage was given to each mouse at week six and at week nine, while the mice were injected with MMPsense680 at week 12. For the Prosense680 group, ten mice were used (three for control, three for week six, and four for week nine). For the MMPSense680 group, six mice were imaged (two for control and four for week 12).

4.2.3 FMT-XCT and validation strategies

The home-built FMT-XCT system introduced in Chapter 3 performed the FMT-XCT imaging. As Figure 4.1 illustrates, three groups of asthmatic mice were imaged by FMT-XCT and cyroslicing separately. The first group, of four mice (one control mouse and three asthmatic mice), was imaged by using Prosense 680 after six weeks of DRA

administration. The second group, of six mice (two control mice and four asthmatic mice), was imaged after nine weeks of DRA challenge. The third group, also consisting of six mice (two control mice and four asthmatic mice), was imaged after a three-week rest following nine weeks of DRA treatment. The FMT-XCT system employs a 360-degree rotation gantry system that carries both the XCT and the FMT illumination and detection components to achieve hybrid imaging of mice under identical placement conditions. To avoid fluorescent signals from food, all mice were fed a non-fluorescent diet before and during experimentation. The mice were shaved and then chemically depilated to reduce the influence of fur on the optical measurements. Subsequently, the animals were anesthetized with an isoflurane inhalation (Isoflurane 2.5%, O_2 0.85L/min) during the imaging experiment. Quantitative 3D fluorophore distribution was reconstructed using 50 iterations of the LSQR inversion algorithm (explained in Chapter 3). Mean values of the fluorescence distribution were computed in the thorax region (obtained by the XCT transverse image).

After FMT-XCT imaging the mice were euthanized, frozen to -50°C, and submitted for whole-body cryoslicing. Fluorescence images were acquired from each mouse's cryoslices, and were employed to validate the *in vivo* findings. A multispectral epi-illumination cryoslicing system performed all cryoslicing imaging, which Section 3.8 explains. *Ex vivo* cryoslicing offers high-resolution colored and fluorescent cross-sectional images of the animal lung. A maximum exposure time of seven seconds was applied to acquire the cryosectioned fluorescence images. The mean fluorescence intensity value in the lung region of each image slice was quantified. The quantification procedure involved normalizing the fluorescence image by the exposure time after background subtraction. The background subtraction represents a calculation of the mean value of a 200×200-pixel region in the image that did not contain mouse tissue. The value of this background mean was then calculated from the entire fluorescent cryosectioned image. After normalization, specific ROIs were extracted from the color image and used to compute the mean intensity of the fluorescence image in the ROI (note that the color and fluorescence image was obtained using matching parameters). Lastly, main slices in the lung region were marked and processed by the above procedure to compute the average fluorescence intensity value for these marked slices.

When collecting cryosliced images, some of the representative slices from the specimen were selected for histological H&E staining. For H&E staining, the ROI slices were fixed in 4% PFA (Santa Cruz, Heidelberg) and then rinsed with distilled water. To stain the nuclei, the slices were incubated in Mayer's haematoxylin (Carl Roth, Karlsruhe, Germany) for 30 seconds and then rinsed with tap water, which changed

the color from red to blue as a result of pH alteration. To stain the cytoplasm, the slices were incubated in Eosin G (Carl Roth, Karlsruhe, Germany) for one second and then rinsed with distilled water. The slices were dehydrated next in 70%, 94%, and 100% Ethanol, followed by ten-minute Xylene incubation. Finally, the slices were covered with Rotimount cover media (Carl Roth, Karlsruhe, Germany). Representative slides were observed using a Zeiss Axio Imager M2 upright microscope, and pictures were taken using an Axiocam 105 color camera (Carl Zeiss, Jena, Germany).

4.3 Results

4.3.1 Quantitative evaluation of asthmatic inflammation using Prosense680

Figure 4.2 depicts results from the *in vivo* studies and *ex vivo* validations. Figure 4.2 compares the hybrid FMT-XCT reconstruction results with the fluorescent cryosection images for two mice in week six using the Prosense680 imaging agent. One mouse acts as a control (seen in the first row of Figure 4.2), while the other mouse is DRA-sensitized for six weeks (second row of Figure 4.2). Figure 4.2 (a) shows a transverse XCT cross-section through the lung region of the control (which was intranasally treated with saline for six weeks). The reconstructed fluorescence signal is superimposed on the transverse XCT cross-section as shown in Figure 4.2 (b). Corresponding *ex vivo* color and fluorescence images of the control mouse were obtained by cryoslicing, and are shown in Figures 4.2 (c) and 4.2 (d), respectively; these cryoslicing images are used for validation of the FMT-XCT reconstructions. Figures 4.2 (e)-(h) depict the *in vivo* and *ex vivo* images for the six-week DRA-sensitized asthma mouse model. White arrows in Figures 4.2 (e)-(h) indicate the identical region in the ROI, and demonstrate one mild inflammatory part in the left lung. A comparison between the lung regions in Figures 4.2 (d) and 4.2 (h) indicate that an higher fluorescence intensity can be found in the asthmatic mouse through cryoslicing.

The comparison of the FMT-XCT reconstructed fluorescence distribution between the control mouse and the DRA-challenged mouse also clearly indicates an increase in fluorescence signal in the lung region (see Figures 4.2 (b) and 4.2 (f)). The cryosliced fluorescence profiles and hybrid FMT-XCT reconstruction have considerable

correspondence, as Figure 4.2 establishes. The arrows in Figures 4.2 (f) and 4.2 (h) denote the part of lung exhibiting a high fluorescence signal, indicative of asthma-related biological activity. Note that, due to the freezing process and small displacements of the animals, slight shifts between *in vivo* images and *ex vivo* cryoslicing images are expected; hence, absolutely identical representations cannot be achieved. Figures 4.2 (i)-(l) show the H&E staining images, where asthmatic features are observable in the six-week DRA-treated mouse as compared to the control mouse (see Figures 4.2 (j) and 4.2 (l) for control). These asthmatic features represent significant inflammatory infiltration and airway epithelium hypertrophy. This biologic finding correlates strongly with the FMT-XCT reconstruction results.
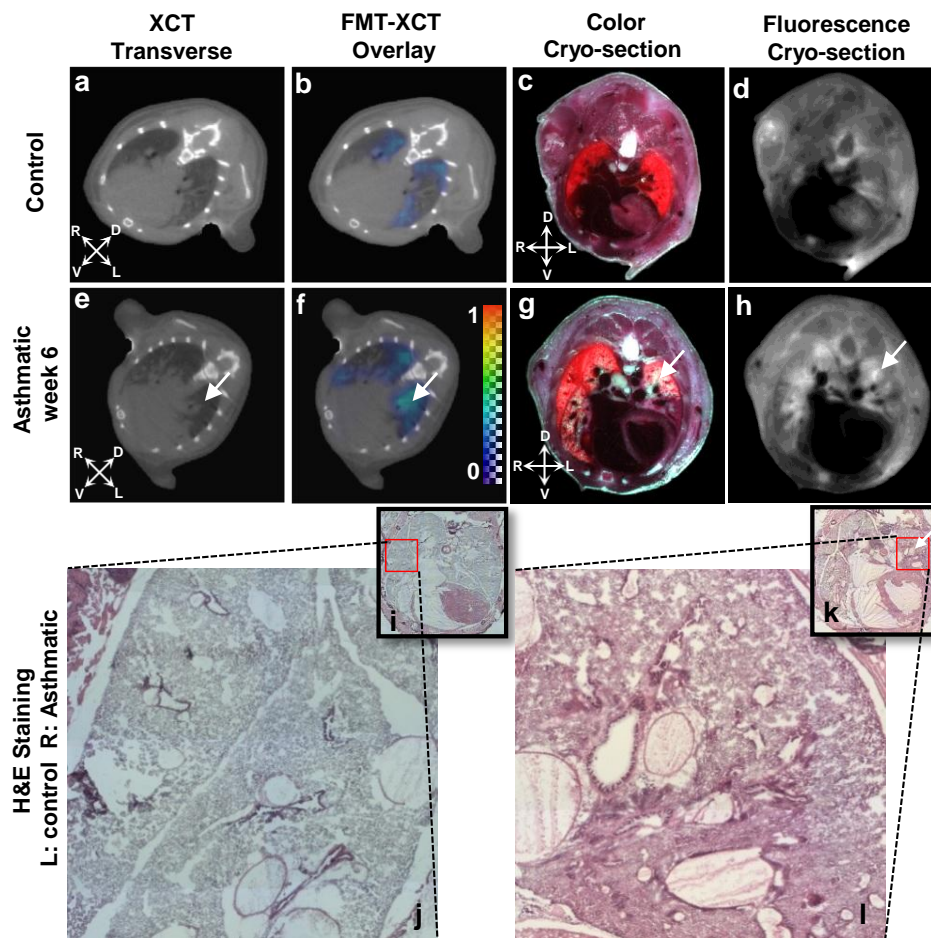

Figure 4.2. Representative slice comparison of FMT-XCT reconstruction, cryoslicing image, and H&E staining in sixth week using ProSense680 fluorescent agent between control mouse and asthmatic mouse model. (a)-(d) are images obtained from different imaging modalities for the same slice of a control mouse in the sixth week, where (a) is the XCT transverse plane, (b) is the transverse slice of FMT reconstruction overlaid on the XCT slice, (c) is the cryoslicing color image, and (d) is the transverse normalized

fluorescent cryosection for validation of FMT-XCT reconstruction. (e)-(h) are images obtained from different imaging modalities of DRA-sensitized asthma murine in the sixth week, where (e) is the XCT transverse plane, (f) is the transverse slice of FMT reconstruction overlaid on the XCT slice, (g) is the cryoslicing color image, and (h) is the transverse normalized fluorescent cryosection. (i)-(j) are H&E staining results of control mouse, where (i) is the whole sample slide, and (j) shows the larger picture of the red rectangular region in (i). (k)-(l) are the H&E staining results of asthmatic mouse at the same time point, where (k) depicts the whole sample slide, and (l) shows the larger figure of red rectangular region in (k). Coordinate systems are designated by D (dorsal), V (ventral), L (left), and R (right).

Figure 4.3 displays the FMT-XCT reconstructions along with cryoslicing images for both the control mouse and the asthma mouse model in week nine using ProSense680 as an imaging agent. Figures 4.3 (a)-(d) show images obtained from *in vivo* FMT-XCT experiments and *ex vivo* cryoslicing of the control mouse at week nine. Figure 4.3 (a) displays the transverse plane of the XCT image, and Figure 4.3 (b) depicts the FMT-XCT reconstructed fluorescence signal overlaid on the transverse XCT slice. Figure 4.3 (c) indicates the color cryoslicing image of the control mouse, while Figure 4.3 (d) represents the corresponding fluorescence cryosection after normalization with exposure time and background subtraction. Figures 4.3 (e)-(h) indicate results of the DRA-challenged asthma model in week nine. Figure 4.3 (f) exhibits fluorescence accumulation in the lung region clearly, which correlates well with the cryosection image in Figure 4.3 (h); all white arrows in Figure 4.3 highlight the strongest inflammatory regions.

As observed in Figure 4.3, the FMT-XCT imaging technique achieved strong conformity with the cryosection validation results. The inflammatory lung regions were fairly distinguishable from the surrounding tissue (see Figures 4.3 (f) and 4.3 (h)). After nine weeks of DRA treatment, more severe inflammatory cell accumulation was observed than in the control mouse. Here, the severity was also notably higher than in the sixth week's analysis, which substantiates FMT-XCT's value for staging asthma. The severity can be seen in the impairment of multiple lung lobes, with the loss of alveolar segments. These challenged areas are all found associated with bronchus, middle sized airways, indicating one intra-tracheal treated tissue damage. The involved lobes also showed a high-fluorescence signal in this study's FMT-XCT reconstruction analysis and corresponding cryosection slides. Figures 4.3 (d) and 4.3 (h) also observe fluorescence signals in the bone region, which further demonstrates the important role of cathepsins in bone resorption [164]. Inputting the prior XCT-based segmentation information in the FMT-XCT reconstruction allows one to discard the

artifacts and the false-positive signals from ribs in Figures 4.3 (b) and 4.3 (f). As the yellow arrows in Figures 4.3 (d) and 4.3 (h) denote, the cryoslicing fluorescence images show a high fluorescence signal in the mouse's spine region. However, the corresponding FMT-XCT reconstruction results indicate greatly diminished fluorescence concentration in the mouse's spine region (see Figures 4.3 (b) and 4.3 (f)).
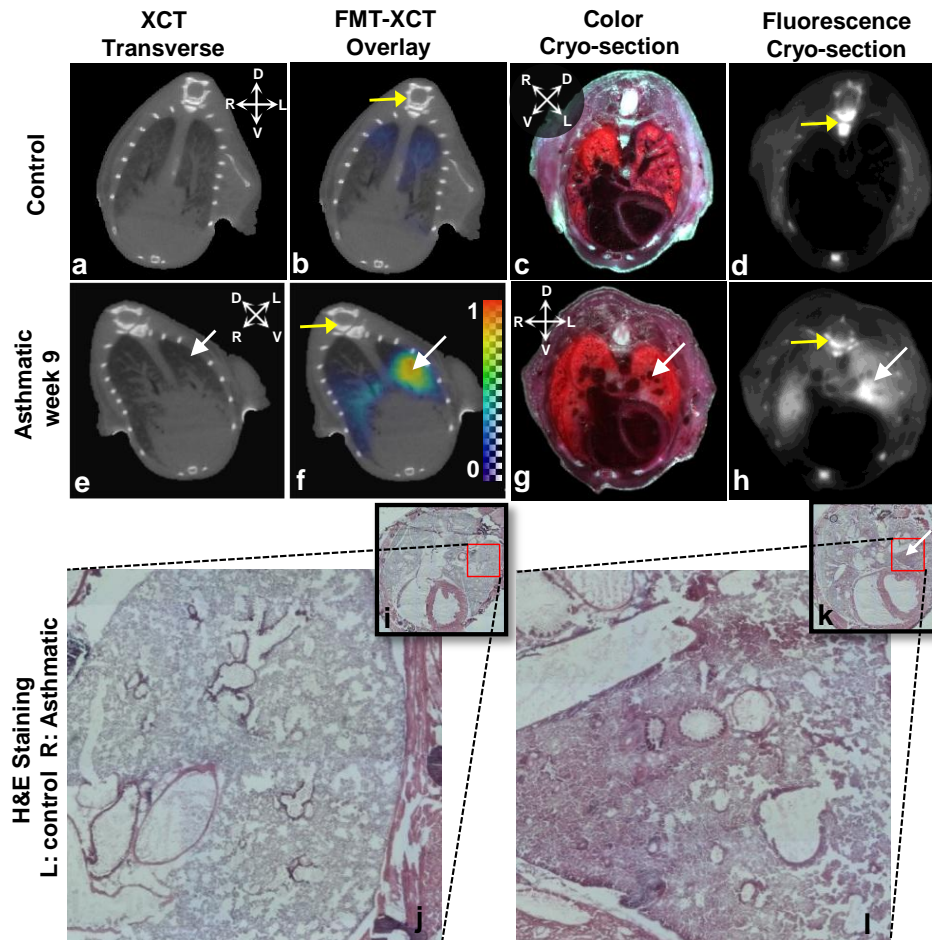

Figure 4.3. Representative slice comparison of FMT-XCT reconstruction, cryoslicing images, and H&E staining in week nine using ProSense680 fluorescent agent. Images (a)-(d) are obtained from different imaging modalities of the same slice of one control mouse, where (a) shows the XCT transverse plane, (b) is the transverse slice of the FMT reconstruction overlaid on the XCT slice, (c) depicts the cryoslicing color image, and (d) is the transverse normalized fluorescent cryosection. Images (e)-(h) are obtained from different imaging modalities of the same slice of DRA-sensitized asthma murine at the ninth week, where (e) is the XCT transverse plane, (f) illustrates the transverse slice of the FMT reconstruction overlaid on the XCT slice, (g) shows the cryoslicing color image, and (h) is the transverse normalized fluorescent cryosection

for validation of FMT reconstruction. All white arrows illustrate the same ROI, indicating the most serious inflammatory part in the lung of the asthmatic mouse. (i)-(j) are the H&E staining results of the control mouse in week nine, where (i) shows the whole sample slide, and enlarged view (j) represents the red rectangular region in (i). (k)-(l) show the H&E staining results of the DRA-challenged asthmatic mouse in week nine, where (k) depicts the whole sample slide, and enlarged view (l) represents the red rectangular region in (k). Coordinate systems are designated by D (dorsal), V (ventral), L (left), and R (right).

Figure 4.4 depicts a 3D-rendered image of mouse bones and lungs co-registered with fluorescence intensity acquired from FMT-XCT reconstructions and fluorescent cryosections, respectively, for two different time points of the DRA model and the control model. Figures 4.4 (a) and 4.4 (d) depict the same control mouse. Figures 4.4 (b) and 4.4 (e) represent the FMT-XCT reconstruction and cryosections for the six-week DRA-sensitized mouse, while Figures 4.4 (c) and 4.4 (f) indicate the equivalent for the nine-week DRA-sensitized mouse. The 3D renderings offer a direct assessment of volumetric activity present in the lung, and similarly showcase increased activity in the entire DRA-sensitized organ compared with the control lung.
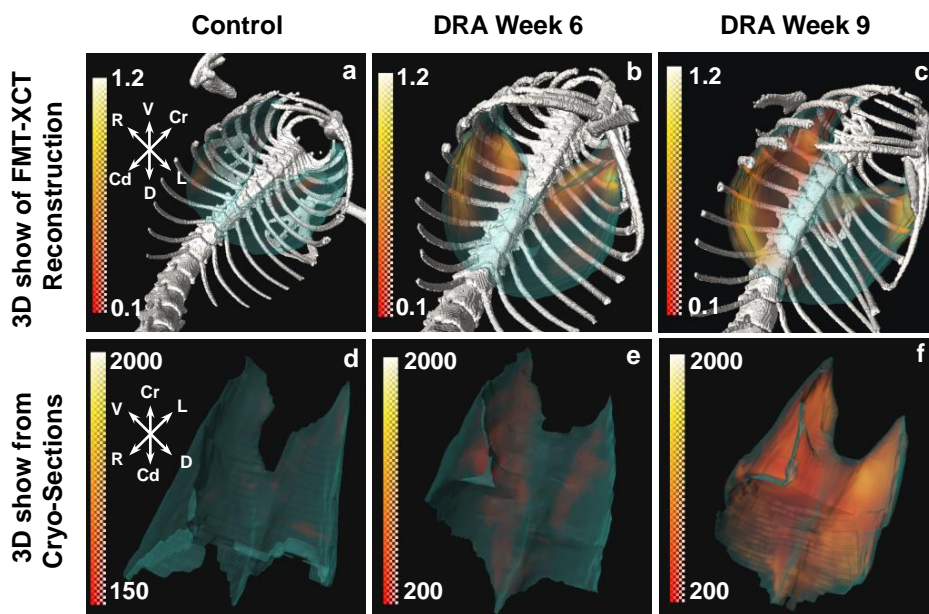

Figure 4.4. Three-dimensional rendering comparison of hybrid FMT-XCT reconstruction and cryosections between different time points of the asthma model and the control mouse. (a)-(c) are 3D renderings of mice bones and lungs based on XCT segmentation and fluorescence signal reconstructed from FMT-XCT, where (a) is the control mouse, (b) is the six-week DRA-sensitized mouse with Prosense680, and (c)

is the nine-week DRA-challenged mouse with ProSense680. (d)-(e) show 3D renderings of mice lungs based on color cryoslicing images and fluorescence signals from the corresponding fluorescent cryosections, where (d) is the control mouse, (e) is the six-week DRA-sensitized mouse with Prosense680, and (f) is the nine-week DRA-challenged mouse with ProSense680. Coordinate systems are designated by D (dorsal), V (ventral), Cr (cranial), Cd (caudal), L (left), and R (right). Three-dimensional rendering was implemented using Amira software.

4.3.2 Quantitative evaluation of asthmatic inflammation and remodeling

Analysis of different airway parameters in the chronic DRA model reported that, three weeks after the final DRA challenge, airway inflammation and remodeling persisted [147]. Previous studies showed that MMPs activity can effectively assess the severity of pulmonary inflammation and remodeling [157]. The ability of the hybrid FMT-XCT system to resolve parameters when evaluating asthma-related inflammation and remodeling with fluorescent agent MMPSense680 is examined here. In this experiment, six mice were imaged with the FMT-XCT system alongside cryoslicing validation; two of the mice acted as a control, while four mice were challenged for nine weeks and rested for three weeks.
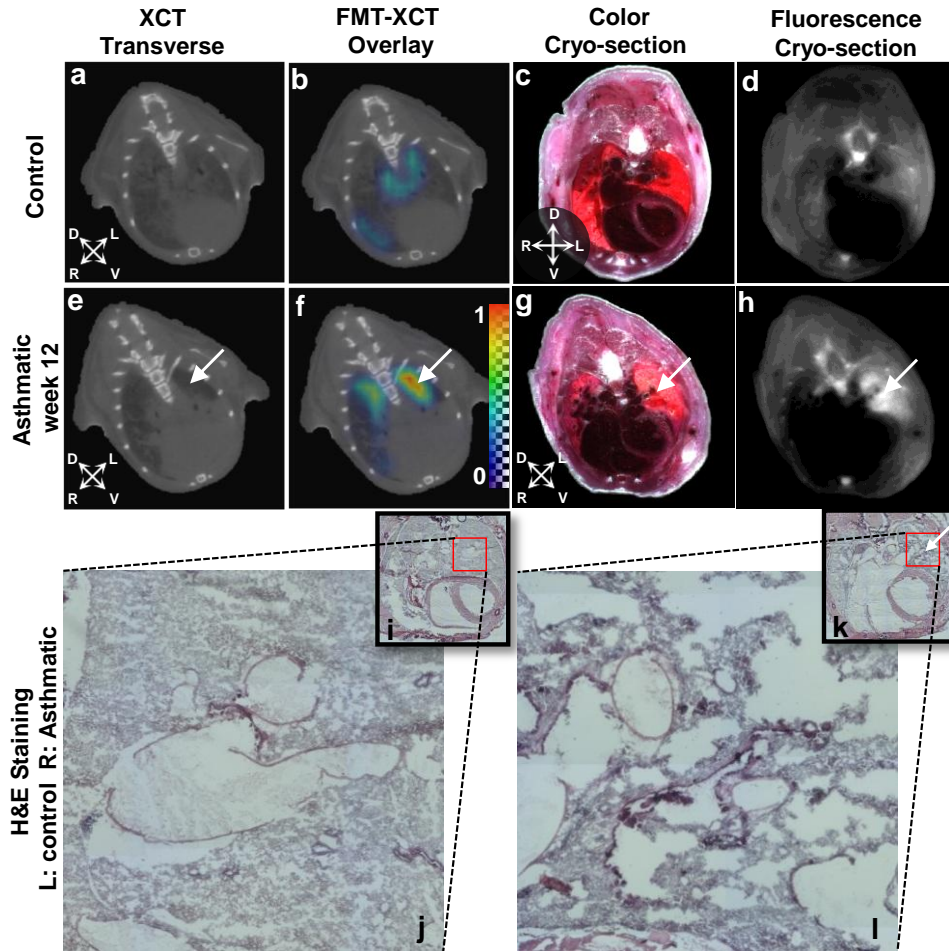
Figure 4.5. Representative slice comparison of FMT-XCT reconstruction, cryoslicing image, and H&E staining in week 12 using the fluorescent agent MMPSense680. Images (a)-(d) are obtained from different imaging modalities from the same slice of the control mouse, where (a) is the XCT transverse plane, (b) is the transverse slice of the FMT reconstruction overlaid on the XCT slice, (c) shows the cryoslicing color image, and (d) depicts the transverse normalized fluorescent cryosection. Images (e)-(h) are obtained from different imaging modalities from the same slice of the asthma model at 12 weeks (with three weeks of rest after the final DRA treatment in week nine), where (e) is the XCT transverse plane, (f) is the transverse slice of the FMT reconstruction overlaid on the XCT slice, (g) shows the cryoslicing color image, and (h) represents the transverse normalized fluorescent cryosection for validation of FMT reconstruction. (i)-(j) are the H&E staining results of the control mouse, where (i) shows the whole sample slide, and enlarged view (j) represents the red rectangular region in (i). (k)-(l) are the H&E staining results of the asthmatic mouse, where (k) is the whole sample slide, and enlarged view (l) represents the red rectangular region in

(k). White arrows indicate the inflammatory and remodeling asthma region. Coordinate systems are designated by D (dorsal), V (ventral), L (left), and R (right).

Figure 4.5 indicates the results of the *in-vivo* and *ex-vivo* studies from week 12 (three weeks after the final DRA challenge in week nine), intravenously injected with MMPSense680. The comparison of the control and the asthmatic mouse on a representative transverse slice of XCT image is shown in Figures 4.5 (a) and 4.5 (e), respectively. The comparison of the FMT reconstruction overlaid on the XCT with the representative slice for the control and the asthmatic mouse is indicated in Figures 4.5 (b) and 4.5 (f), respectively. Figures 4.5 (c) and 4.5 (g) indicate the color cryosection images of the identical slice with the control and the asthmatic mouse, respectively, while Figures 4.5 (d) and 4.5 (h) show the corresponding fluorescence cryosection images. The top row of Figure 4.5 illustrates one representative control mouse that was intranasally treated with saline for nine weeks before resting for three weeks. The second row shows a nine-week DRA-challenged mouse that rested for three weeks after the challenge. Arrows in Figures 4.5 (f) and 4.5 (h) indicate a clear increase in the fluorescence distribution compared with the nearby lung tissue, which demonstrates the capability of fluorescence imaging to localize and identify asthma. On the other hand, Figures 4.5 (b) and 4.5 (d) do not show a rise in fluorescence distribution in the control mouse treated with saline, which confirms that fluorescence imaging is capable of identifying asthmatic conditions with very high sensitivity. By comparing the histological findings of the control mouse in Figures 4.5 (i) and 4.5 (j) with the histology results of DRA-treated mouse in Figures 4.5 (k) and 4.5 (l), clear chronic lung morphologic damage appears. Figure 4.5 (l) indicates that inflammation was found in a central area with immune-cell accumulation and lymphocyte aggregation. Further, lung remodeling is observable in these mice, demonstrated by an enlarged air space in the alveoli septum and loss of lung structures. This obstructive lung disease was also apparent in this study's FMT-XCT reconstructions.

4.3.3 Statistical analysis for FMT-XCT

In order to precisely assess the imaging capability of the hybrid FMT-XCT system for evaluation of asthma-related inflammation severity, a quantitative assessment of *in vivo* FMT-XCT reconstructions against corresponding *ex vivo* cryoslicing images was performed. The statistical analysis involved evaluating all 16 mice used for this study. On the one hand, for the Prosense680 group, three control mice (one control mouse with six weeks of saline treatment and two control mice with nine weeks of saline treatment), three mice challenged for six weeks with DRA, and four mice challenged

for nine weeks with DRA were used in total. On the other hand, for the MMPSense680 group, two control mice (with nine weeks of saline treatment and three weeks of rest) and four asthmatic mice (with nine weeks of DRA treatment and three weeks of rest) were imaged and analyzed.
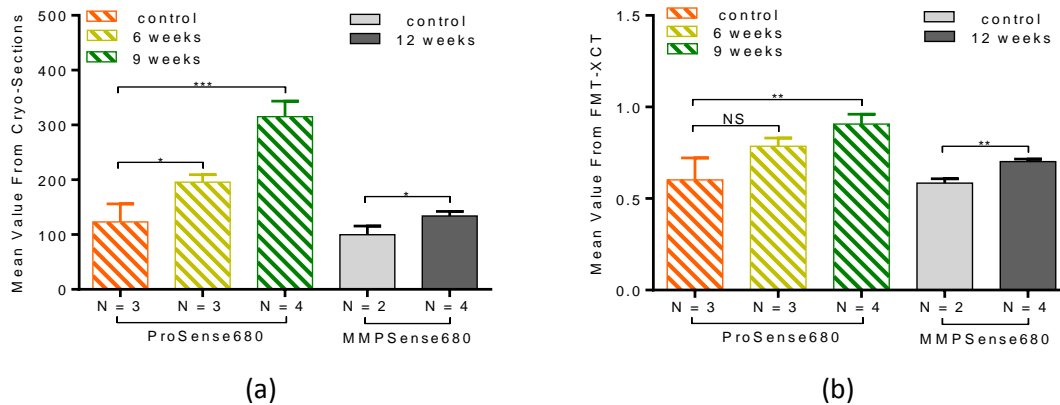

(a)   (b)

Figure 4.6. Bar plots (mean ± standard error of the mean (SEM)) showing different inflammation and remodeling severity. The mean value is computed for the FMT-XCT reconstructions and the cryosection intensities for a DRA-challenged mice and a control group at different time points of the protocol. Colored bars depict the mice with Prosense680 at week six and at week nine, gray bars show mice with MMPSense680 at week 12. (a) is a bar plot showing the mean intensity values of cryoslicing. (b) is a bar plot showing the mean values from the FMT-XCT reconstructed results. Asterisks indicate statistical significance using a Student's t-test (*: $p < 0.05$; **: $p < 0.01$; ***: $p < 0.001$; NS: non-significant).

Figure 4.6 (a) shows the evaluation of inflammation severity: the bar plot indicates the computed mean values of fluorescence intensity from *ex vivo* cryosections. The average values were computed at different time points using either ProSense680 of MMPSense680 as fluorescent agents. A 58% increase of mean fluorescence intensity was observed when comparing the six-week DRA-challenged mice treated with ProSense680 against the control mice. On the other hand, a 155% increase was observed in the asthmatic mice at week nine, resulting in a significant difference in the mean values of fluorescence signal measured in the control mice. Note that a 61% increase was observed in the asthmatic mice at week nine compared with the asthmatic mice at week six, which indicates the capability of staging the asthmatic condition. At 12 weeks (i.e., three weeks of rest after the final DRA treatment in week nine) in the MMPSense680 group, the asthma model showed a 34% increase relative to the corresponding saline-treated control group.

Similar to the cryoslicing imaging in Figure 4.6 (b), the average values were computed to evaluate the hybrid FMT-XCT's imaging performance. Its performance with Prosense680 as the fluorescence agent showed a 31% increase at week six and a 51% increase at week nine compared with the control mouse. Note that a 15% increase was observed in the asthmatic mice at week nine compared with the asthmatic mice at week six. After three weeks of rest in the MMPSense680 group, the asthmatic mice showed a 31% rise over the control group. The increasing tendencies of FMT-XCT quantification correlated tightly with the *ex vivo* cryosection results.

Results of FMT-XCT quantification showed great consistency with the *ex vivo* validation numbers. Figure 4.7 plots the mean fluorescence values of the cryoslicing analysis against the corresponding values obtained with the FMT-XCT system. The mean values for the week-nine mice are higher than the week-six mice (Prosense680), indicating that continued exposure to allergens increases the inflammatory burden in the lung.
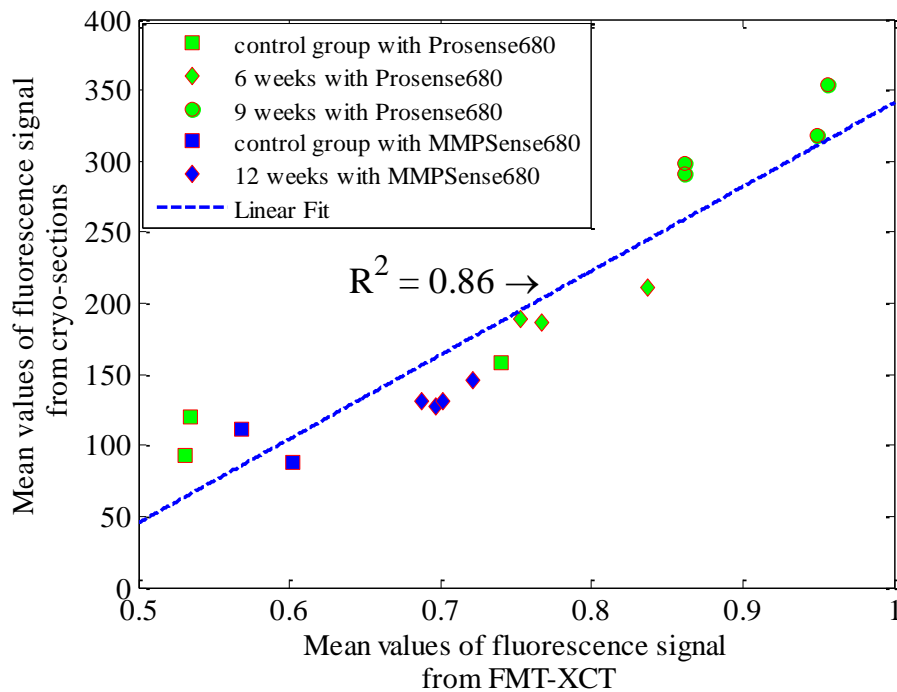

Figure 4.7. Linear fit of mean value of the fluorescence signal from cryosection images plotted against the FMT-XCT findings for all 16 mice studied.

4.4 Conclusion

Biomedical research increasingly considers noninvasive imaging techniques that can lead to important insights about disease development on an identical mouse model. While nuclear imaging methods can resolve biological contrast, their short-lived radioisotopes limits its usage and the ionizing radiation involved prohibits repeated experiments on the same animal. This chapter investigated hybrid FMT-XCT imaging as an alternative modality to nuclear methods in asthma research. It focused on resolving cathepsins, as a biomarker of eosinophil activity, and matrix metalloproteinases implicated in airway remodeling and inflammation.

Different studies have established the ability to utilize near-infrared fluorescent labels to resolve pulmonary inflammation and remodeling in COPD, or asthma, models [6, 82, 157]. Of particular importance to this study were: to interrogate the merits of the hybrid FMT-XCT 360-degree projection, to examine the image fidelity and quantification achieved against fluorescence cryoslicing images, and to employ FMT-XCT as an imaging gold standard. Since the selection of reconstruction parameters may alter image parameters, this study consistently employed the same parameters for all mice scanned, including estimates of the absorption and the scattering coefficients for different organs, which were based on previous literature estimates [123].

In comparison to cryoslicing imaging and H&E staining, FMT-XCT enables the noninvasive study of DRA-based asthma responses at different time points. The *in vivo* results are consistent with previously established *ex vivo* observations of increases in eosinophil, mucus glycoproteins, α-smooth muscle actin, and collagenous fibers in the DRA-asthmatic model three weeks after the final challenge [147]. The FMT-XCT system resolved elevated fluorescence intensity in the lung region of the asthmatic mouse by displaying increased cathepsin and MMP expression, which was further confirmed by *ex vivo* cryoslicing imaging. At week 12, the histological image of the DRA model confirms the asthmatic inflammation and remodeling features.

5 Neutrophils assessment in atherosclerosis model and background subtraction of FMT-XCT

5.1 Introduction

Atherosclerosis and related cardiovascular diseases (CVD) are leading causes of mortality and morbidity in developed countries especially, where they manifest as stroke or myocardial infarction [165, 166]. Atherosclerosis is a chronic inflammatory disease of the arterial wall with significant involvement of the immune system [167]. Immune cells, such as mast cells, T lymphocytes, and macrophages, are the main components of atherosclerosis. The fact that these immune cells are rich during the process of lesion-formation in atherosclerotic subjects has been established for years [168].

In recent years, greater attention has been drawn to the use of activatable fluorescent agents, which significantly increases the studies of different cardiovascular pathologies [169, 170]. There have been some quantifications of atherosclerosis-related protease activity from matrix-metalloproteinases (MMPs) [70, 171, 172] and different cathepsins [173, 174]. Many imaging modalities have become an important

tool for cardiovascular and atherosclerosis research. Molecular imaging of atherosclerosis is difficult, because vessels move rapidly and surrounding tissue creates a strong background signal. Hybrid imaging modalities, combing FMT and MRI, has been demonstrated as a powerful imaging tool for atherosclerosis in mice [70]. When assisted by cathepsin and integrin NIRF agents, a standalone FMT noninvasive imaging modality was also presented as an early diagnosis strategy for atherosclerosis [175]. A hybrid FMT-XCT system provides higher sensitivity and reconstruction accuracy than a standalone FMT, and it is more cost-effective than FMT-MRI.

As an important inflammatory cell in the innate immune system, neutrophils in the pathophysiology of atherosclerosis play an important role in early and late stages of atherosclerosis [176-178]. Neutrophils are phagocytes that aim to track and to destroy pathogenic organisms: they are recruited for first-line defense in acute injury. As Soehnlein et al. [179] discovered in 2009, neutrophils invade the intima and secrete granule proteins during early stages of plaque formation from atherosclerosis. These granule proteins recruit and activate other inflammatory cells. Activated neutrophils secrete granule proteins (e.g., myeloperoxidase, neutrophil elastase, cathepsin G, and proteinase 3) [179]. Unfortunately, *in vivo* detection of these activated neutrophils remains challenging, due to their short life span and their functional phenotypic changes [180].

This chapter uses the hybrid FMT-XCT system to quantify protease activity of neutrophils in early stages of atherosclerosis. Here, the system employs an atherosclerosis mouse model and Neutrophil Elastase 680 FAST (a novel neutrophil elastase activatable near-infrared fluorescence agent).

5.2 Material and methods

5.2.1 Mouse model

The two most commonly used mouse models for atherosclerosis research are apoE-/- and LDLR-/- [181]. The LDL model contains a receptor that is an expressed plasma membrane protein for clearance of plasma lipoproteins. Plaque develops in the vascular sites. In this longitudinal study, LDLR-/- mice (C57BL/6, Jackson Laboratory, Bar Harbor, ME, USA) were used as an atherosclerosis model to study neutrophils. Fourteen- to fifteen-weeks-old LDLR-/- mice were fed a high-fat diet (HFD), which is a Western-Type diet containing 21% fat, 0.15% cholesterol, and 19.5% casein. As shown

in Figure 5.1, all mice studied were classified into four groups: zero weeks of diet feeding, four weeks of diet feeding, eight weeks of diet feeding, and 12 weeks of diet feeding. For the control group, LDLR-/- mice were fed a normal chow diet.
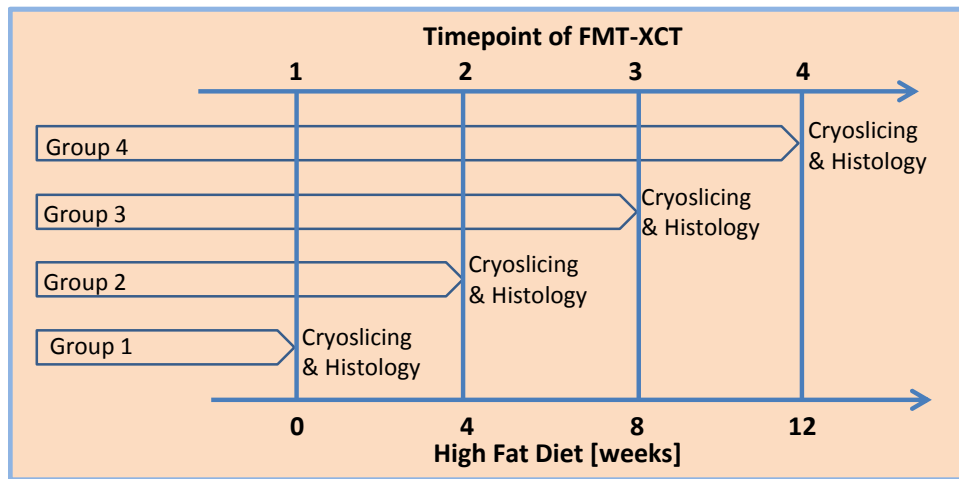

Figure 5.1. Schematic diagram of the HFD-fed atherosclerosis mouse model and related imaging strategies of FMT-XCT (cryoslicing and histology).

5.2.2 Two imaging agents

This study used one commercially available contrast agent, called Neutrophil Elastase 680 FAST (Perkin Elmer, Waltham, USA). It is a neutrophil elastase activatable fluorescent imaging agent, and is optically silent upon injection. The agent only produces a fluorescence signal after achieving cleavage by elastase-produced neutrophil cells. The half-life of this agent in plasma is four hours.

Each vial of Neutrophil Elastase 680 FAST contains 48 nmol of the agent in dry solid form. By using 1.2 ml PBS for reconstitution, one vial could be administered for approximately ten mice (25 g weight for each mouse). For each mouse, a 4 nmol dose in $100\ \mu l$ is recommended. For an *in vivo* imaging study, the agent should be administered via intravenous injection in the tail vein 4-8 hours before imaging. The excitation wavelength for the agent is 680 nm, and the emission wavelength is centered at 700 nm.

Another commercial agent, Exitron nano 12000 (Miltenyi Biotec, CA, USA), was used to facilitate the visualization of the vasculature and contrast of the XCT reconstruction. It is a nanoparticle contrast agent specifically for preclinical *in vivo* study of micro-CT. Because it is metal-based, vessels show a strongly absorbed image in XCT projections

from its circulation in the bloodstream. For each approximately 20 g-mouse, the typical injection dose is 30 mg iodine in 100 μl volume.

5.2.3 Imaging protocols and validation

Figure 5.2 shows the whole processing procedure for each mouse. As Figure 5.2 (a) displays, roughly 4 nmol/100 μl of fluorescence agent Neutrophil Elastase 680 FAST was injected intravenously via the tail vein of an anaesthetized experimental mouse 4-8 hours before imaging. The mouse's thorax region was depilated afterward. This step was crucial, because animal fur on and around the imaged area of the specimen blocks, absorbs, and scatters light during the imaging procedure. Tissue scatters and absorbs near-infrared light minimally, but fur scatters and absorbs it enormously. Right before putting the anaesthetized mouse into the FMT-XCT imaging system, XCT contrast agent Exitron nano 12000 was administered intravenously (see Figure 5.2(c)) through its tail vein.

For FMT-XCT data acquisition, the fluorescent agent required a 680 nm channel. Four groups of atherosclerosis mouse models were imaged at four different time points for this longitudinal study of neutrophil cells in atherosclerosis (see Figure 5.1): the first group was 14-15-weeks-old LDLR-/- mice; the second group was LDLR-/- HFD-fed mice for four weeks; the third group was HFD-fed mice for eight weeks; and the fourth group was HFD-fed mice for twelve weeks. All of the mice were anesthetized with an isoflurane inhalation of 2.5% isoflurane and 0.85 L/min oxygen. Atherosclerosis plaque typically builds up inside of the arteries, and prefers to develop at arterial branches [182]. Therefore, the aortic root and the aortic arch, located in the thorax region, represent this study's ROI and its FMT-XCT-imaging region. Around 20-30 laser source locations were calculated to acquire excitation and emission images for each gantry angle. After FMT-XCT imaging, the mice were euthanized for *ex vivo* cryoslicing and histological validation.
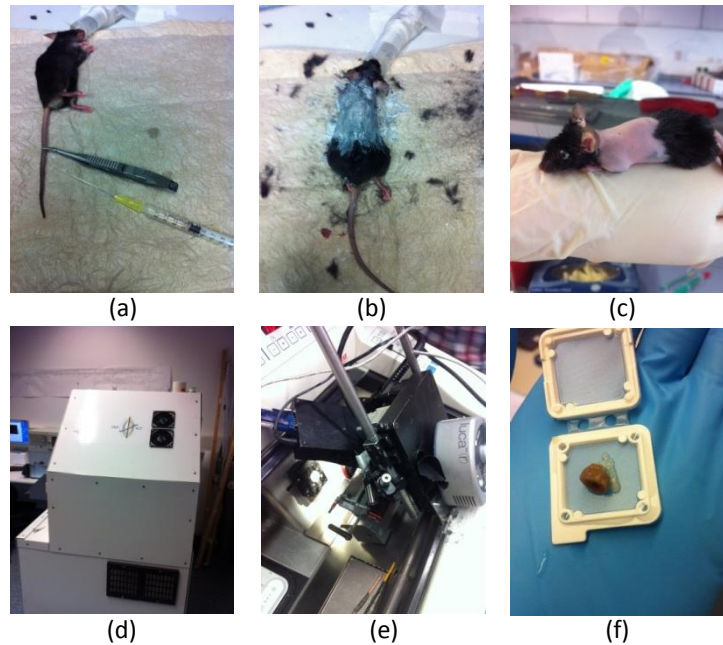
(a) (b) (c)

(d) (e) (f)

Figure 5.2. Schematic diagram of the atherosclerosis mouse model study protocol. (a) shows the fluorescence agent injection 4-8 hours before FMT-XCT imaging. (b) records mouse depilation. (c) shows the injection of the XCT contrast agent right before FMT-XCT imaging. (d) pictures the FMT-XCT data collection. (e) represents the *ex vivo* validation by multispectral cryoslicing. (f) shows histology validation.

For *ex vivo* neutrophil counting, the mice were euthanized before their heart and aortic arch were immersed in 4% Formalin. The aortic root and arch were embedded in paraffin after dehydration, and then sectioned and placed on adhesive-glass slides. Neutrophil staining was then conducted with an anti-Ly6G antibody with dilution 1:200. Following primary antibody incubation, a Dako Streptavidin-Biotin (LSAB) system visualized the neutrophils with horseradish peroxidase (HRP). A nuclei counterstain was performed with haematoxylin. ImageJ software analyzed all of the slides by counting the number of neutrophils and measuring the plaque size. Collaborator Almut Glinzer from the Klinikum Recht Der Isar performed this histological analysis part.

5.3 Results

5.3.1 Assessment of atherosclerosis-related neutrophils

As mentioned in Section 5.2, because atherosclerotic plaque accumulate significantly in the aortic root and the aortic arch, which is in the thorax region, all the imaging modalities focusing on this region for fluorescence light emission by looking for activated neutrophils. Figure 5.3 depicts a representative comparative result between a control mouse and a typical atherosclerotic mouse through noninvasive FMT-XCT imaging and validation cryoslicing imaging. The three figures on the top row are images of cryosections from the control mouse (which was fed with normal chow food). Figure 5.3 (a) shows a transverse color image, and 5.3 (b) depicts the corresponding fluorescence image for the same transverse slice. To show the interested region clearly (which is the aortic arch of the aorta), a magnified view of the dashed rectangular area in 5.3 (b) is shown in 5.3 (c). The relatively black area in the middle of 5.3 (c) is the arch region, which appears vague and difficult to find the vessel walls. The second row of Figure 5.3 shows cryoslicing transverse images from an atherosclerotic mouse that was HFD-fed for 12 weeks. Figure 5.3 (d) illustrates the transverse color image, and 5.3 (e) shows the matching related fluorescence cross-section. Figure 5.3 (f) shows an enlarged view of the arch region in 5.3 (e). The third row of Figure 5.3 depicts the FMT-XCT reconstruction for a typical atherosclerotic mouse. Figure 5.3 (g) shows a three-dimensional rendering of the FMT-XCT reconstruction displayed on the reconstructed and segmented XCT result. Figure 5.3 (h) depicts a transverse slice image from the XCT reconstruction. The red arrow in Figure 5.3 (h) points at the interested aortic arch. Figure 5.3 (i) shows the FMT-XCT inversed fluorescence distribution on the XCT transverse slice.

Comparing the control mouse in Figure 5.3 (c) with the atherosclerotic mouse 5.3 (f) demonstrates two findings. First, the comparison shows that atherosclerotic plaque successfully accumulated in the aortic arch region of the HFD-fed LDLR-/- mouse model. The blue arrow in 5.3 (f) points out the white swath of plaque attached to the aortic wall. Second, the comparison proves the performance of fluorescence agent Neutrophil Elastase 680 FAST. The control mouse was not injected with any fluorescent agent, and 5.3 (c) is therefore blurry even in intensity range 0-150. Injecting an activatable fluorescent agent makes the aortic region and other regions

clear on fluorescent cryosections with an intensity range of 0-900. This indicates that cryoslicing images can prove a powerful validation tool for even tiny ROIs.

The FMT-XCT reconstruction can assesses fluorescence distribution of marked neutrophils in the aortic arch area than the cryoslicing result in Figure 5.3 (f). As Figure 5.3 (i) illustrates, the pseudo-color in the center shows fluorescence intensity reconstructed by FMT-XCT inversion, which is in the same aortic arch area pointed out by the red arrow in 5.3 (h). A 3D illustration of fluorescence distribution in Figure 5.3 (g) also indicates the activated neutrophil elastase agent distribution in the regions of the aortic arch and the descending aorta (gray part), which is designated by white arrow in the figure.
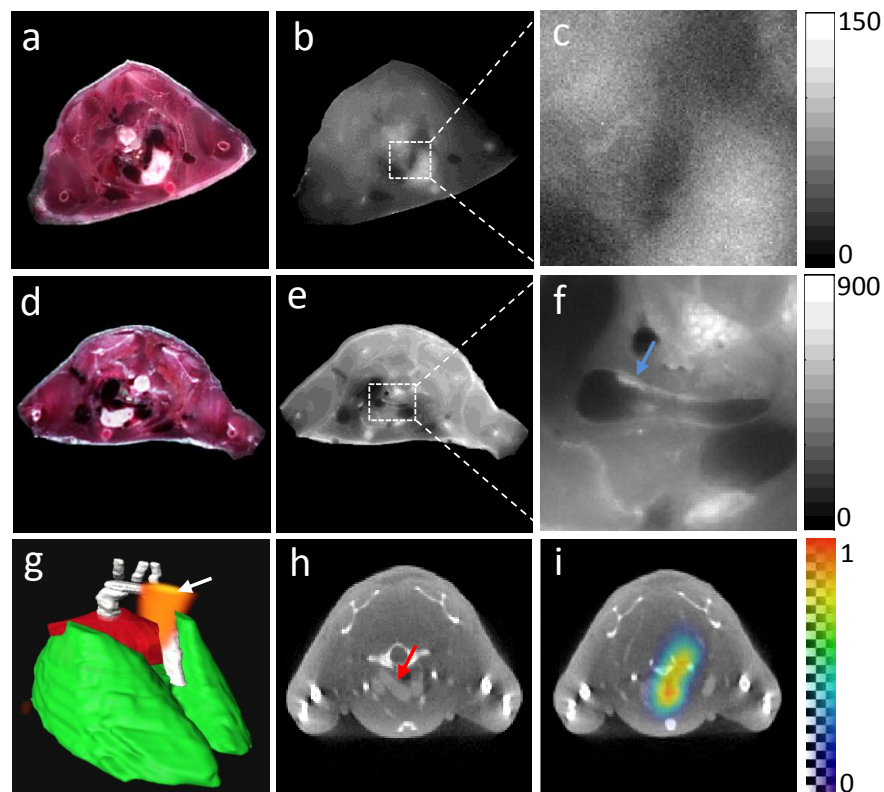

Figure 5.3. Representative slice comparisons of the atherosclerosis mouse model and the control mouse by FMT-XCT imaging and cryoslicing imaging validation. (a) shows a colorful cryoslicing image from the control mouse. (b) is the corresponding transverse slice of a fluorescence cryosection from same control mouse. (c) is an enlarged view of the rectangular region in (b). (d) shows one cryoslicing color figure from the atherosclerosis mouse model. (e) is the corresponding fluorescent cryosection slice from same mouse. (f) is an enlarged view of the rectangular ROI in (e). (g) is a 3D-rendered view of FMT-XCT reconstruction (pseudo color), shown on an XCT

segmentation of the lung (green), the heart (red), and the aortic arch (gray). (h) is one transverse view of a slice from XCT reconstruction. (i) is the FMT-XCT reconstruction overlaid on the same transverse slice.

5.3.2 Quantitative statistical analysis and histology validation

For post-reconstruction quantification of FMT-XCT, five continuous slices of reconstructed fluorescence distribution were selected from the thorax region; then, the mean value of these five slices was calculated for a quantification result of this mouse. As for cryosection quantification comparison, one fluorescence cross-section containing the aortic arch was first chosen. Then, this fluorescent image was normalized by the exposure time after background subtraction. To obtain the background subtraction, a small region around the corner of the image was first chosen as a background region (away from the imaged sample). The mean value of this background region was used for subtraction. The aortic arch was segmented manually after background removal and normalization, because the contrast between the arch and the surround tissue was not clear for some mice. Then, another small area of tissue away from arch was selected as a noisy region. Dividing the mean value of the aortic arch by the mean value of the noisy region established the fluorescent cryosection quantification reference for FMT-XCT reconstruction verification.
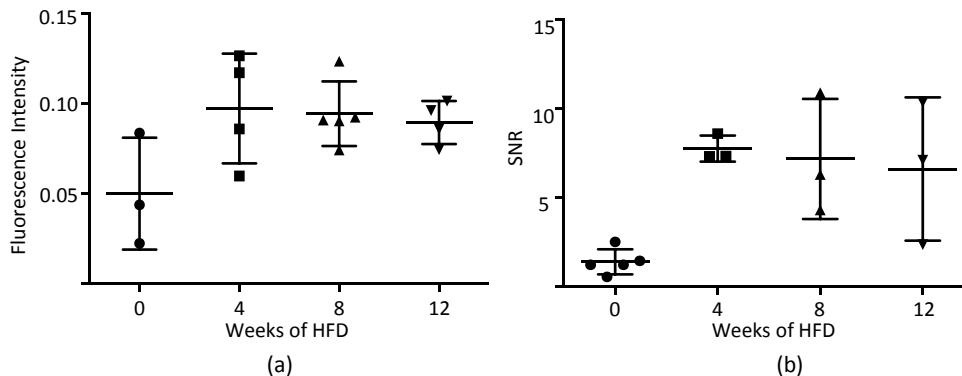

Figure 5.4. FMT-XCT reconstruction quantification of all mice and cryoslicing quantification. (a) is the FMT-XCT quantification plot. (b) shows the cryoslicing quantification.

Figure 5.4 compares the FMT-XCT reconstruction quantification with the corresponding fluorescent cryoslicing quantification. The Y-axis in Fig. 5.4 (a) represents fluorescence intensity, and measures the mean values of five

reconstructed slices of ROIs. Figures 5.4 (a) and 5.4 (b), together, exhibit a similar tendency regarding the quantification averages of both imaging modalities: after four weeks of HFD feeding, the neutrophil counts reach a maximum (in the study's time span), which validates the claim that neutrophils have a short life span [180]. After eight weeks of HFD feeding, neutrophil counts decrease slightly, and, 12 weeks later, decrease more. One interesting takeaway when comparing Figures 5.4 (a) and 5.4 (b) is that, at the initial research time point (0 weeks of HFD feeding), the FMT-XCT system reconstructed a relatively higher mean value of fluorescence intensity than the cryoslicing quantification analysis. In theory, at 0 weeks of HFD feeding, neutrophils ought to be absent or fewer, which the cryoslicing result confirms. This means that some background noise remains in the FMT-XCT's reconstructed results. The next section will try to reduce this noise.
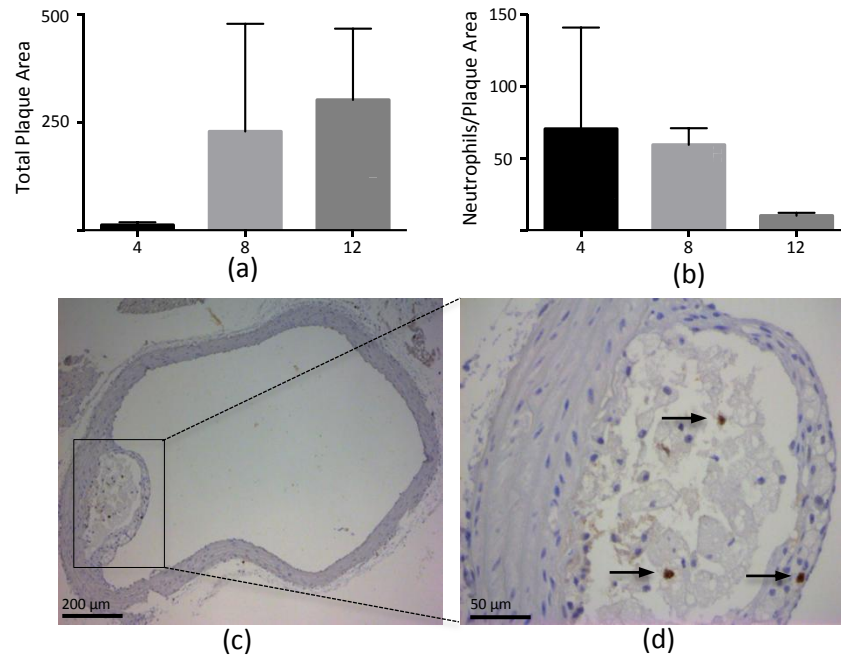

Figure 5.5. Histological validation of FMT-XCT quantification result, statistically. (a) charts the total plaque-area sizes in the aortic arch. (b) compares the quotients of neutrophil amounts per plaque area in the aortic arch. (c) is representative immunostaining of neutrophils cells in aortic arch section.

Our collaborator completed the histological immunostainings for all *ex vivo* neutrophil counts in order to validate this study's FMT-XCT reconstruction results, which Figure 5.5 presents above. Figure 5.5 (a) charts the total plaque area in the aortic arch at four weeks of the HFD, at eight weeks of the HFD, and at 12 weeks of the HFD. Figure 5.5

(b) depicts the immunostainings' proportions of total neutrophil counts per entire plaque-area size for the aortic arch region. Figure 5.5 (b) clearly portrays that the neutrophils-per-area values gradually descended over time, an outcome that corroborates the FMT-XCT quantification findings. Although Figure 5.5 (a) shows the total plaque areas greatly expanding, the neutrophils-per-area values still drop over time. One disadvantage of these results is that the immunostainings only examined the aortic arch area. The corresponding FMT-XCT results quantified the aortic arch and root regions. However, this domain disparity does not nullify the comparison: the aortic arch is the main place for atherosclerotic plaque, and neutrophils mostly accumulate in this area.

5.4 Optimized FMT-XCT reconstruction by background subtraction

5.4.1 Two-wavelength-based background subtraction method

As Figure 5.4 indicates even when *ex vivo* cryoslicing quantification reveals few neutrophils, FMT-XCT quantification still reports a high number of them. This incongruity was considered noise or background in FMT-XCT reconstruction. Here, a strategy for removing or reducing this noise is proposed.

There have been many strategies proposed to reduce background noise for fluorescence molecular tomography [183-190]. Soubert and Ntziachristos [187] advised a background level estimation strategy that introduced a linear relationship between the Born ration and the proportional source-detector distance. Ale et al. [183] optimized this method by proposing a data-driven proportionality estimation for the distance-correlated fluorescence background. The proportionality constant was calculated as a ratio of a source-detector pair's normalized measurements to a corresponding source-detector distance. Background-estimation strategies related to multispectral methods were also studied [186, 189, 191]. Nicolas et al. [186] developed a spectral method that used shorter-wavelength excitation measurements for auto-fluorescence correction from measurements of an exciting probe's peak excitation wavelength. Kenneth presented a dual-tracer-based background subtraction approach [189], which introduced one untargeted tracer with characteristics similar to background noise. Kenneth proportionally subtracted the

untargeted tracer signal from the targeted tracer signal to improve FMT reconstruction quality. Fei et al., in 2012 [191], introduced another background subtraction algorithm that also utilized a shorter-wavelength excitation light to generate a background auto-fluorescence signal. The team calculated the subtraction coefficient, as a constant, by solving a least-squares problem.

Here, this study developed a method that estimates and removes the shared nonspecific background of FMT-XCT reconstruction. This communal background arises with every FMT-XCT reconstruction, because the data collection of FMT and the inversion procedure generate it. For instance, the auto-fluorescence of tissue, the noise from a specimen-holder bar's reflectance, and the inversion or optical-property approximations all mismatch with a real situation. These noises exist similarly for each mouse in every FMT-XCT reconstruction regardless of the probe or wavelength selected, since data collection and processing procedures are almost the same every time. Sometimes, these noises are too big to locate the real fluorescence source.

This study's measured data at a second wavelength to estimate mutual nonspecific background. This hybrid FMT-XCT system, explained in Section 3.4, contains two different wavelength lasers set at two commercially and commonly used probe wavelengths: 680 nm and 750 nm. After choosing the targeted tracer wavelength (e.g., 680 nm in the atherosclerosis model application above), the other wavelength laser was set as untargeted wavelength background. An FMT-XCT inversion was performed for both wavelengths. The optimized reconstruction result is given by:

$$I_{result} = I_{targeted} - \alpha I_{untargeted} \quad subject\ to\ \ I_{result} \geq 0 \qquad (5.1)$$

Here, I_{result} denotes the optimized FMT-XCT-reconstructed fluorescence distribution, $I_{targeted}$ and $I_{untargeted}$ represent the targeted probe wavelength for FMT-XCT reconstruction (680 nm for this study) and reconstruction by untargeted wavelength (750 nm in this case), respectively. The scaling coefficient α is important to balance the weight of background in every reconstruction, which was estimated manually by experience.

For data collection, two data sets of FMT were collected separately for both the target tracer wavelength and the corresponding untargeted tracer wavelength by using two different lasers and corresponding filter sets. The two sets of FMT data acquired indicate that one data set of white image was used to collect excitation and emission images of both wavelengths. The laser source locations calculated were identical for both cases, which was important for separate inversion of each wavelength afterward

because it eliminated the noise introduced by source perturbation. Lastly, because the specimens were stationary throughout the data collection process, one set of XCT raw data could be used in FMT-XCT inversion reconstruction for both wavelengths.

For inversion of FMT-XCT, two reconstructions were performed separately for each wavelength on an identical ROI. All reconstruction parameters maintained consistency for these two inversions (the LSQR methods, the iterative number, the optical properties for every segmentation, the XCT-generated mesh, the regularization parameter, and the regularization matrix). After calculating two inversions, the reconstructed targeted fluorescence distribution was subtracted proportionally from the untargeted fluorescence result (see Equation 5.1). The disadvantage of this method was its greater time cost compared with the original FMT-XCT methodology, because data collection and FMT-XCT inversion is to be performed twice. For *in vivo* data collection, the mouse was under anesthesia around 2.5 hours during the process. Anesthesia depth control involved lowering the isoflurane to 1.5% or less after one hour of 2.5% isoflurane inhalation to avoid mouse death in the relatively cold environment of the FMT-XCT system.

5.4.2 Optimized FMT-XCT reconstruction results

A tissue-like phantom validation experiment was carried out to demonstrate the above background subtraction method. It used the same phantom and setup introduced in Section 3.7. Two 1 mm-diameter tubes containing two near-infrared fluorescence dyes—20 pmol of Alexa Fluor 680 and 40 pmol of Alexa Fluor 750 (Thermo Fisher Scientific, WA, USA)—were cast into the phantom. One XCT raw projection and two separate FMT raw data sets (at different wavelengths) were acquired and inversion was performed later. In this setup, one of the near-infrared fluorescence dyes was arranged as the targeted fluorescence source, and the other dye was set as the untargeted fluorescence background. The experiment's second half performed the setup in reverse. Two identical inversions conducted for both 680 nm and 750 nm fluorescence dyes verified the background estimation strategy. Figure 5.6 displays the results of phantom validation.

Figure 5.6 (a) depicts a schematic diagram of the phantom validation setup. Figures 5.6 (b) and 5.6 (c) shows the reconstruction results for the 680 nm dye and the 750 nm dye generated from using the original FMT-XCT inversion method. Figures 5.6 (d) and 5.6 (e) display the reconstruction results for the 680 nm dye and the 750 nm dye obtained with the subtraction method, which subtracted corresponding 750 nm and

680 nm reconstruction results as backgrounds. Non-negativity constraint was used for both cases. As Figures 5.6 (d) and 5.6 (e) demonstrate, the reconstructed fluorescence sources are more localized after removing nonspecific mutual background. To underscore the localization more obviously, one blue line was drawn on the transverse image of fluorescence distribution across both source's centers (as shown in Figure 5.6 (a)). Figure 5.6 (f) plots the intensity profiles of all four reconstructions along this blue line. Two green lines in Figure 5.6 (f) represent two reconstructions for 750 nm dye. The solid green line and the dashed line mean reconstruction before subtraction and after. After background removal, the dashed line is sharper than the original reconstruction (the solid line). The subtracted part—the right part of the solid red line, pointed out by the blue arrow—occupies around 10% of the total reconstruction for the 750 nm dye. The same comparison conclusion can be drawn for the reconstructions of the Alex Fluor 680 dye, which are shown as red lines in Figure 5.6 (f). The peak value for the 750 nm dye is roughly 0.95 and the corresponding value for the 680 nm dye is around 0.47, which is half of the 750 nm-dye's value. These peak values ascertain the quantity of both dyes used for the experiment: one is 40 pmol, and the other is half. The removed part of the background, shown by the left blue arrow in 5.6 (f), also occupies around 10% of the entire reconstruction; hence we can conclude that the background in the original FMT-XCT method is quite noticeable. The green vertical line in the middle of Figure 5.6 (f) shows that the removed parts for both wavelengths are almost symmetrical, which demonstrates this non-specific inversion noise has no specific relationship with wavelength.
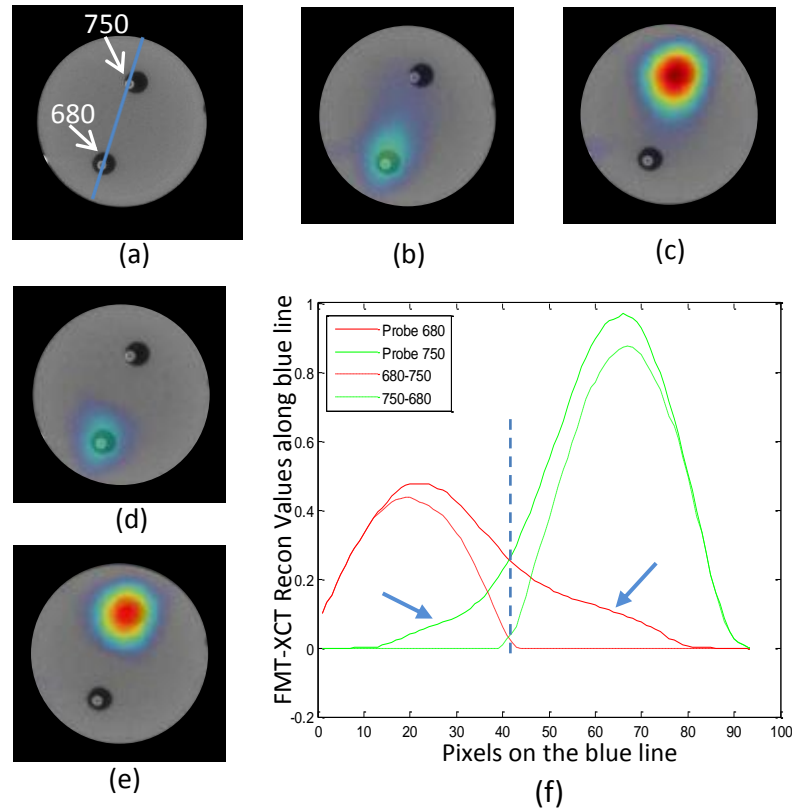
Figure 5.6. Phantom validation results of optimized background subtraction for FMT-XCT inversion. (a) is the schematic diagram of one phantom transverse image from XCT reconstruction with two cased fluorescent dyes marked by a blue line and two arrows. (b) is a FMT-XCT inversion-reconstructed slice displayed on an XCT image without background subtraction for the Alexa Fluor 680 probe. (c) is the FMT-XCT inversion without background subtraction for the Alexa Fluor 750 dye. (d) is the FMT-XCT inversion with subtraction of 680-750. (e) is the FMT-XCT inversion with subtraction of 750-680. (f) is a line profile along the blue line in (a) for four FMT-XCT inversions.

The optimized FMT-XCT method (background subtraction) was applied to the atherosclerosis model. The application's main motivation was that neutrophils do accumulate around the aortic arch—located in the middle of the small animal, and difficult for FMT-XCT inversion because of the arch's location (deep inside the body)—even though those neutrophils are not numerous. Fewer neutrophils reduce fluorescence intensity and may merge with background (e.g., the cryoslicing result Figure 5.3 (f) displays).　Figure 5.7 shows the effect of subtraction on the atherosclerotic model and control mouse. Since this application used Neutrophil

Elastase 680 FAST as a fluorescence agent, the FMT data was collected at 750 nm to match the background conditions.
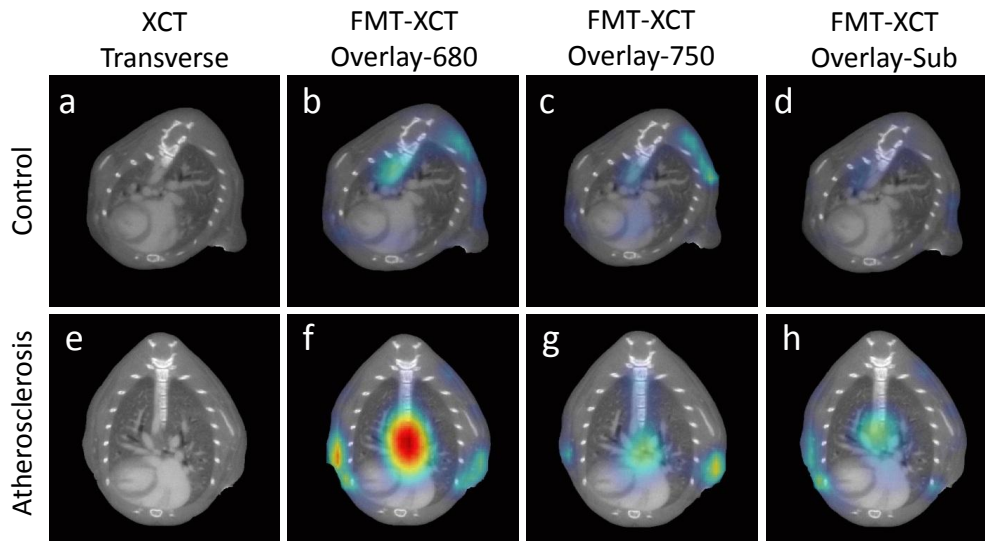

Figure 5.7. Background subtraction strategy applied on atherosclerosis mouse model. (a)-(d) compare the inversion results for one control mouse, where (a) is the XCT transverse image, is the (b) FMT-XCT inversion of targeted 680 nm-fluorescence distribution superimposed on (a), (c) depicts the FMT-XCT inversion of untargeted 750 nm-background-noise distribution, and (d) represents the non-negativity constraint subtraction of (b) and (c). (e)-(h) are the corresponding comparison for the atherosclerosis mouse, where (e) is the transverse XCT image, (f) is the 680 nm reconstruction from the original FMT-XCT inversion before subtraction, (g) is the reconstructed noise from the 750 nm data, and (h) shows the result after performing the subtraction method.

To test the performance of fluorescence molecular tomography *in vivo*, the proposed, optimized FMT-XCT inversion method was also applied on the atherosclerotic model. The fluorescence distribution was reconstructed for the control mouse (without any fluorescence agent), and the 12-week HFD-fed atherosclerosis mouse. The reconstructed fluorescence distributions in Figures 5.7 (b) and 5.7 (c) are nearly identical; however, this study's optimized method controlled background after completing subtraction, as Figure 5.7 (d) shows. The atherosclerosis model mouse (Figures 5.7 (f)-(h)), same conclusion can be arrived at. Mutual reconstruction noises (Figure 5.7 (f), which depicts fluorescence distributions around mouse boundaries as well as overly strong signals in the center) significantly reduced after using the subtraction method. In Figure 5.7 (h), fluorescence distribution in the center shows

the actual location and intensity of neutrophil-activated fluorescence (here, located in the mouse's aorta).

5.5 Conclusion

This chapter investigated the FMT-XCT imaging system for longitudinal cardiovascular research. To the best of our knowledge, FMT-XCT was used for the first time to track early-stage neutrophil activity by using commercial fluorescent imaging agent Neutrophil Elastase 680 FAST. Comparing the validation results from the fluorescent cryoslicing image with the FMT-XCT-reconstructed image establishes that the hybrid FMT-XCT enables the noninvasive study of atherosclerosis-related neutrophils at different stages. Imaging the aortic root and arch regions, which are located in the thorax region, demonstrates that conclusion.

Because neutrophils-activated fluorescence distribution was low in FMT-XCT reconstruction results, we developed a background subtraction method to remove the noise from the inversion method and other sources. By using one untargeted wavelength as background, the reconstructed targeted fluorescence was subtracted proportionally. Both the targeted wavelength FMT data and the untargeted wavelength FMT data needed to be collected under identical conditions. A phantom experiment was performed to validate the performance of our subtraction strategy. After verifying its performance, this method was used in the atherosclerosis study. Two mouse samples—a control mouse with no fluorescence distribution and a atherosclerosis mouse—were tested, and the final results showed that this new background subtraction improved both FMT-XCT inversion quality and accuracy.

6 Integrins-targeted fluorescence imaging of non-small cell lung cancer

6.1 Introduction

Lung cancer is one of the most pervasive type of cancer, and mortality from lung and bronchus cancers in United States outnumbered all other cancers in both men and women in 2015 [192]. There are two types of lung cancer: non-small cell lung cancer (NSCLC) and small cell lung cancer (SCLC). Small cell lung cancer spreads and grows differently in the body than NSCLCs. Small cell lung cancer is defined as "a malignant epithelial tumor consisting of small cells with scant cytoplasm, ill-defined cell borders, finely granular nuclear chromatin, and absent or inconspicuous nucleoli" [193]. Lung cancer accounts for 12% of all new cases of cancer worldwide, and SCLC represents approximately 15% of all lung cancers. An estimated 33,900 new SCLC patients were diagnosed in the United States [194]. Mostly attributable to cigarette smoking, SCLC is greatly aggressive [195, 196] with a poor prognosis: a five-year survival rate under 7% [197]. Chemotherapy and radiotherapy are the main clinical treatment strategies to reduce tumor vasculature for the majority of patients, and they respond well for initial treatment. Unfortunately, almost all patients relapse within 6-12 months with resistant disease [197].

Non-small cell lung cancer is the most common type of lung cancer, and accounts for approximately 85% of diagnosis [198, 199]. The primary factor of NSCLC causality is tobacco smoking. Non-small cell lung cancer is subdivided into four groups: adenocarcinomas, squamous cell carcinomas, bronchioloalveolar carcinomas, and large-cell carcinomas [200]. Non-small cell lung cancers express completely different

histopathologic characteristics than SCLCs [201]. Diagnoses of NSCLC have been increasing in many countries, and its appearance is becoming more common in smokers as well as non-smokers [202]. The low survival rates from lung cancer result from late diagnosis. In order to improve the understanding of NSCLC's molecular characterization, preclinical research assisted by different imaging modalities is urgently needed.

Mouse models of NSCLC have similar morphologic and histopathologic characteristics as humans with NSCLC, and are a valuable tool to understand lung tumor biology and development; they can also help validate tumor cells and different methods of therapy research [203]. Preclinical murine models of various NSCLCs can provide preliminary information about histology, such as predicting clinical trials of therapy [204]. The Lewis lung carcinoma (LLC) mouse model is the only syngeneic murine model reproducible for NSCLC. The LLC is an NSCLC cell line acquired by implanting a C57BL mouse with primary Lewis lung carcinoma [204]. This LLC mouse model is mainly used for *in vivo* evaluations of chemotherapeutic agent efficiency [205]. For instance, Navelbine therapy evaluation utilized the LLC model before proceeding to clinical trial [206]. A typical LLC mouse model is built by orthotopic injection of the LLC cell line into the peritoneal cavity of a C57B6 mouse [204]. This LLC mouse model differs from other xenograft models, because the injected LLC cells are compatible with the living body's immune system; therefore, true immune responses about the chemical therapy can be fully evaluated with the LLC model [204].

Integrins are heterodimeric transmembrane receptors involved in tumor angiogenesis. Integrins are composed of two subunits of α and β pairings, which form 24 different members of the integrin family by ligand binding. Integrins play an important role between cancer cells as well as between cancer cells and other key components in the extracellular matrix (ECM) [207, 208]. Although many kinds of cells in a tumor microenvironment express a few different integrins, one famous integrin is $\alpha_v\beta_3$, also known as the vitronectin receptor. The $\alpha_v\beta_3$ integrin is highly expressed in newborn vessels, but is absent in resting endothelial cells and most normal organ systems, which makes it very suitable for cancer tracking and anti-angiogenic therapy [209]. Cilengitide, which is a cyclized arginine-glycine-aspartic acid-containing pentapeptide [210], potentialy blocks $\alpha_v\beta_3$'s and other integrins' activation [207]. Recently evaluated in clinical phase I and phase II studies, Cilengitide shows promising results for glioblastoma patients [211-213]. Cilengitide can prevent blood vessels from growing into a tumor. In our study, we use cilengitide to block $\alpha_v\beta_3$ and test our fluorescence probe IntegriSense 680, which will be introduced later.

Angiogenesis is central in the growth and progression of all solid tumors. Tumor growth beyond 1-2 mm requires blood vessels for nutrients and oxygen. Vascular endothelial growth factor (VEGF) is a key mediator signal protein that stimulates angiogenesis in cancers up-regulated by oncogene expression. Presence of VEGF in a tumor can result in an "angiogenic switch" turning on, which stimulates more new vasculature formation in and around the tumor. This important role of VEGF in tumor growth makes it a reasonable target for cancer therapy [214-217]. Bevacizumab, under the trade name Avastin, is one famous angiogenesis inhibitor that can slow the growth of blood vessels around the tumor by inhibiting VEGF [215]. Bevacizumab is a humanized variant of an anti-VEGF antibody approved by the FDA for different cancers [218, 219]. It binds to VEGF extracellularly (on the surface of endothelial cells), and inhibits VEGF's angiogenic activity in order to control the cancer's growth rate. One of our NSCLC-study experiments uses Bevacizumab to control lung tumor size; the experiment quantitatively monitors therapy using the FMT-XCT modality.

Mitogen-activated protein kinase (MAPK) cascades are important pathways to understand the regulation of normal cell proliferation and differentiation. There is one widely used MAPK pathway, named Raf-MEK-ERK, for research on pharmacological inhibitors of cancer treatment [220]. This pathway works in the following way: Raf serine kinase activates the MAPK/ERK kinase (MEK) protein kinases (ERK stands for extracellular signal-regulated kinase). Then, MEK activates the ERK [220]. This Raf-MEK-ERK pathway is the main downstream effector of Ras, and Ras is the most frequently mutated oncogene in humans. Because this pathway is often overactive in lung cancers, it has been the research focus of pharmaceutical cancer treatment. A MEK inhibitor targets the MEK protein in this pathway, and disrupts cancer cell growth and survival [221]. Using FMT-XCT, we also evaluate a MEK inhibitor's therapeutic effect on an NSCLC mouse model.

This study aims to use the hybrid FMT-XCT modality on an LLC-NSCLC model to: monitor tumor growth rate, test the sensitivity of fluorescence probe IntegriSense 680, and assess two different chemotherapies (an angiogenesis inhibitor and an MEK inhibitor).

6.2 Material and methods

Four groups of mice were prepared for this study: one control group without any therapy treatment, one group treated with cilengitide (to block the integrin $\alpha_\text{v}\beta_3$ in

order to test the probe's sensitivity), one group dosed with a VEGF inhibitor, and one group administered with an MEK inhibitor.

6.2.1 Mouse model

To build the LLC mouse model, LLC cells were implanted endotracheally into C57BL/6J mice. The mice were anesthetized, and each mouse was injected with around 1×10^6 LLC cells in 100 μl of phosphate-buffered saline (PBS).

6.2.2 Imaging agents

The probe used for fluorescence imaging is IntegriSense 680 imaging agent (Perkin Elmer, Waltham, USA). This agent is commercially available and utilized for detecting integrin $\alpha_v \beta_3$ *in vivo*. It couples a low-molecular-weight peptidomimetic antagonist with a red fluorochrome (peak excitation wavelength 680 nm). IntegriSense 680 is a targeted fluorescence agent that will bind to the specific biomarker $\alpha_v \beta_3$, which can be found in disease models of oncology, atherosclerosis, and angiogenesis. Each vial of IntegriSense 680 contains 24 nmol in dry solid form. Adding 1.2 ml of PBS to the vial makes sufficient agent for imaging about ten mice, which results in a dosage of 2 nmol in 100 μl solution for each mouse. Before every imaging, the agent should be injected intravenously via the tail vein of the mouse. The optimal imaging time point for this agent is 24 hours after injection. This fluorescence agent was used for imaging each mouse with the FMT-XCT imaging system.

6.2.3 Imaging protocols and validation

As shown in Figure 6.1, four separate groups of mice were used for imaging. The baseline group established a benchmark of NSCLC tumor growth in the LLC mouse model. By blocking the integrin, the cilengitide group was experimented to verify imaging-agent sensitivity. The Avastin and MEK-inhibitor groups were used for testing FMT-XCT's ability to monitor therapeutic effects. After FMT-XCT imaging, the mice were euthanized for cryoslicing validation of FMT-XCT reconstruction. For every mouse from each group, the experiment included three observation time points at three-to-four-day intervals.

The thorax region of each mouse was depilated to remove animal fur, which might otherwise greatly affect the FMT-XCT data as a result of NIR-light absorption and scattering. Each mouse was first imaged to obtain an T2-weighted MRI to track the size of the tumor; FMT-XCT imaging was used only after the tumor surpassed 2 mm.
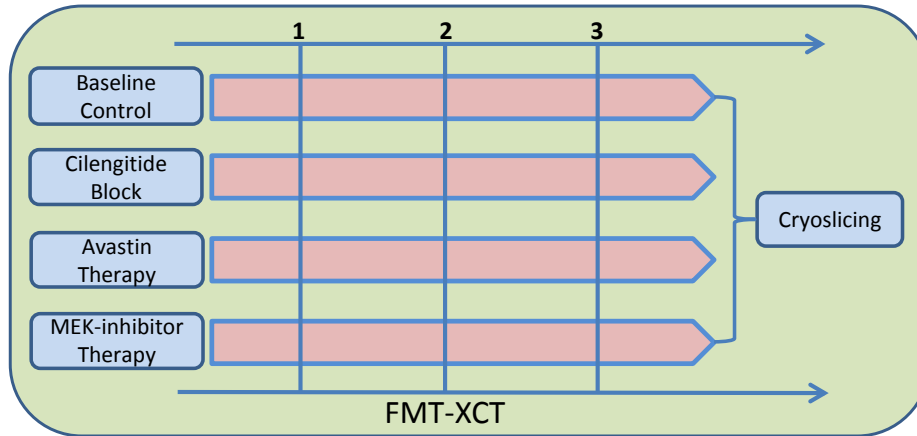

Figure 6.1. Schematic diagram of FMT-XCT's NSCLC mouse-imaging strategies and cryoslicing validation.

6.3 Results

6.3.1 Baseline imaging

The control group mice received no treatment. Three different time points for FMT-XCT imaging is: after MRI imaging chosen the tumor inside is big enough, first FMT-XCT imaging and reconstruction was done. The second and third time points were three days later and one week later, respectively. Figure 6.2 displays the FMT-XCT-reconstructed tumor growth rate that used fluorescence agent IntegriSense 680. Figure 6.2 (a) shows the first time point result, which is a transverse slice of FMT-XCT reconstruction overlaid on the corresponding XCT slice. The second and third time-point results are shown in Figures 6.2 (b) and Fig. 6.2 (c). One caveat: it was not possible to compare an identical slice across the three different time points, because, for every imaging, the mouse's shape and size was slightly different.
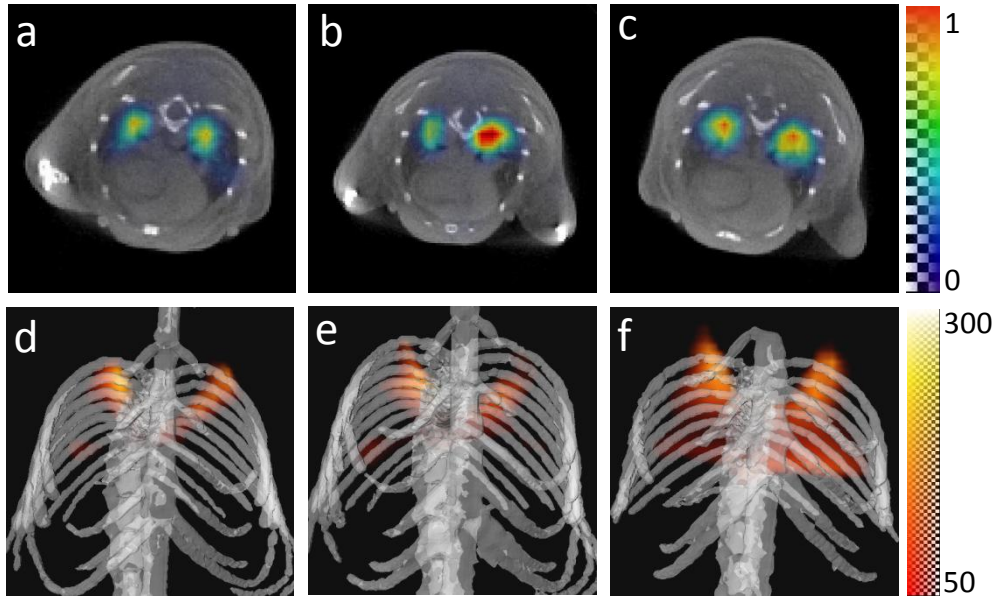
Figure 6.2. A representative slice comparison of FMT-XCT and corresponding 3D rendering for baseline control mouse group. (a) is the transverse slice of FMT-XCT reconstruction overlaid on the XCT slice for first time point. (b) is the same slice after two days. (c) is the same slice from the same mouse one week later. (d)-(f) are 3D renderings of the control mouse at three time points.

Comparing Fig. 6.2 (a)-(c) illustrates that the tumor on the left grew slowly while the tumor on the right side showed almost no change. Because it is sometimes difficult to track the real size of a tumor with two-dimensional images exclusively. Figs 6.2 (d)-(f) displays 3D rendering of FMT-XCT results incorporated into the XCT reconstruction (generated by commercial Amira software). Comparing Fig. 6.2 (d), Fig. 6.2 (e), and Fig. 6.2 (f), demonstrates that the cancer growth rate for the mouse without treatment was rapid; one week later, especially, the tumor size was almost 3-4 times bigger than at the first time point. This experiment is a great example of baseline FMT-XCT imaging an NSCLC LLC mouse model.

6.3.2 Agent sensitivity

To investigate the sensitivity of imaging agent IntegriSense 680, the $\alpha_v\beta_3$ integrin-blocker cilengitide was used for FMT-XCT imaging. Cilengitide is an RGD pentapeptide integrin inhibitor that is active against orthotopic glioblastoma (GBM) xenografts, and can augment radiotherapy and chemotherapy in cancer models [212]. Since fluorescence agent IntegriSense 680 detects $\alpha_v\beta_3$, which is significantly upregulated

in tumor cells, cilengitide can test the sensitivity of a fluorescence agent used. Like the control-group mouse, the mouse was treated with cilengitide daily after initial FMT-XCT imaging. Cilengitide was intraperitoneally injected into the test mouse. After three days and after six days of cilengitide treatment, second and third FMT-XCT imaging datasets were acquired separately. A representative mouse's results are shown in Figure 6.3. Figure 6.3 (a) shows the first time point of FMT-XCT reconstruction by depicting a transverse FMT-XCT-reconstructed fluorescence distribution imposed on an XCT slice. The second time-point FMT-XCT result is shown in Fig. 6.3 (b), and Fig. 6.4 (c) indicates the third time point.
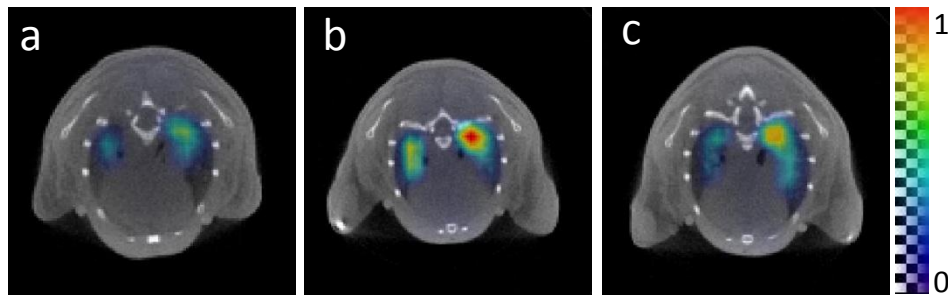

Figure 6.3. A representative slice comparison of FMT-XCT for cilengitide group. (a) is the FMT-XCT-reconstructed lung tumor overlaid on an XCT slice from the first time point. (b) is the FMT-XCT reconstruction of the same mouse after three days of cilengitide treatment. (c) shows the same after one week using cilengitide.

By comparing Figures 6.3 (a)-(b), one can see the tumor is growing slowly; fluorescence intensity strengthens at the second time point. But the third time-point imaging, six days later, shows the fluorescence intensity decreasing, especially in the right lung. This intensity drop means the cilengitide had inhibited the integrin, which also inhibited the fluorescence signal from the second point. Further, compared with the growth rate of the baseline imaging, this integrin-inhibited imaging also proves the effect of cilengitide.

6.3.3 Avastin therapy

The third group used Avastin for chemotherapy of the NSCLC mouse model, which is a recombinant humanized monoclonal antibody developed against VEGF to prevent receptor binding. Avastin is the first anti-angiogenetic treatment approved by the FDA for colorectal cancer, and it demonstrates efficacy for NSCLC in clinical trials. The mice studied in this third group had an NSCLC tumor larger than 2 mm (determined by MRI).

After initial FMT-XCT imaging, the mice in this group were administered intraperitoneally with around 2.5 mg/kg Avastin every day. The second time point was after three days of treatment, and the third time point was after one week of Avastin medication. A typical slice comparison of FMT-XCT reconstructed fluorescence distribution is shown in Figure 6.4. Figure 6.4 (a) depicts the lung tumor at the first time point of FMT-XCT reconstruction. After three days of Avastin treatment, the corresponding FMT-XCT quantification result is shown in Fig. 6.4 (b). The effect of one week of non-stop Avastin treatment is presented in Fig. 6.4 (c). By comparing Figures 6.4 (b) and 6.4 (a), the area of lung cancer expanded over three days. But, after one week of treatment Fig. 6.4 (c), the NSCLC tumor size clearly decreased. This longitudinal study shows that Avastin is an efficient chemotherapy medicine for NSCLC mouse models, and demonstrates the performance of the FMT-XCT system for monitoring treatment.
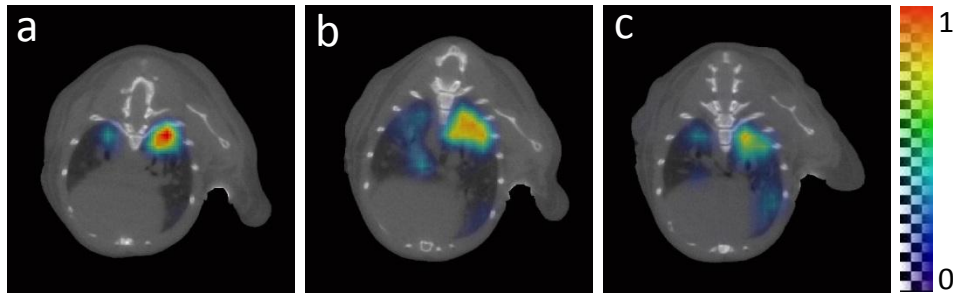

Figure 6.4. A representative slice comparison of FMT-XCT for the Avastin group. (a) is the FMT-XCT-reconstructed lung tumor overlaid on the XCT slice from the first time point. (b) shows the FMT-XCT reconstruction of the same mouse after three days of Avastin treatment. (c) shows the same after six days of treatment.

6.3.4 MEK-inhibitor therapy

Another chemotherapy medicine this study used for the NSCLC model was an MEK inhibitor. This inhibitor was used to affect the specific Raf-MEK-ERK MAPK pathway, which is often overactive in NSCLCs. Like the first Avastin therapy group, first FMT-XCT dataset was collected before treatment only after the mouse had grown a large tumor. Then, 1.5 mg/kg of MEK inhibitor was administered to the mouse every day. A second FMT-XCT imaging of the treated mouse was performed after three days of daily administration. After one week of chemotherapy, the mouse was imaged by FMT-XCT for the third time. All three results are shown in Figure 6.5. Figure 6.5 (a) displays the

FMT-XCT-reconstructed lung tumor at the first time point prior to treatment. The effect of three days of treatment effect is shown in Fig. 6.5 (b), and the corresponding effects after one week is presented in Fig. 6.5 (c). Comparing Fig. 6.5 (a)-(c) reveals that the tumor size was decreasing throughout chemotherapy. Notably, after one week, the largest tumor's size was half of the original in Fig. 6.5 (a). Two-dimensional images cannot show the entire size of every tumor, so three-dimensional renderings of FMT-XCT reconstruction for all three time points of the same mouse are displayed in Figures 6.5 (d)-(f). The same conclusion regarding decreased tumor size can also be observed in the 3D comparison. To be more specific, comparing Fig. 6.5 (d) with Fig. 6.5 (e) reveals that the mouse's left tumor shrunk was obvious. After one week of MEK-inhibitor therapy, the right tumor was nearly eliminated.
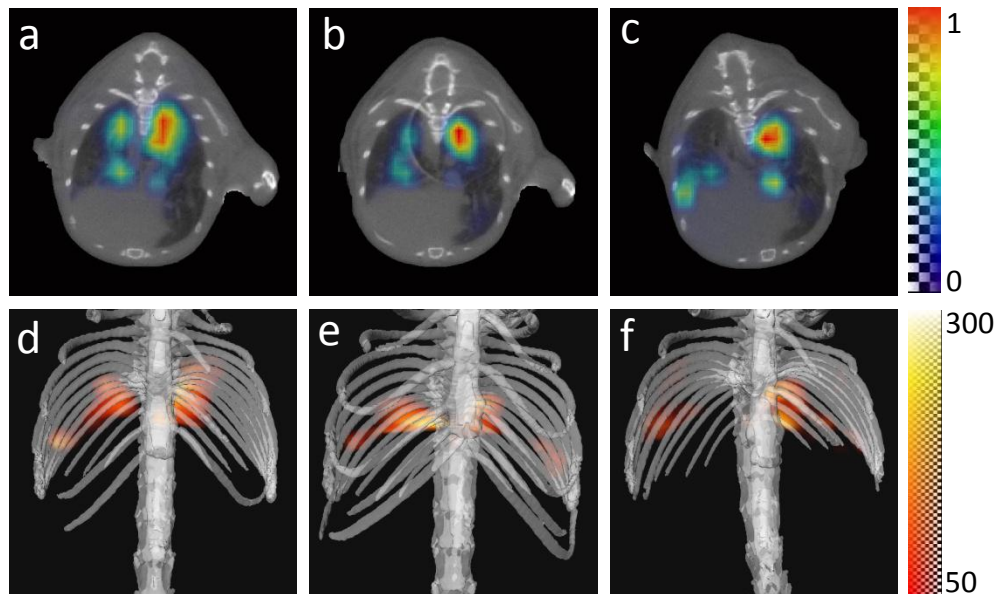

Figure 6.5. A representative slice comparison of FMT-XCT imaging and corresponding 3D rendering for the MEK-inhibitor treatment mouse group. (a) is the transverse slice of the FMT-XCT reconstruction overlaid on the XCT slice at the first time point. (b) is the same slice after three days of MEK-inhibitor medication. (c) is the same slice from the same mouse after one week of MEK-inhibitor treatment. (d)-(f) are 3D renderings of FMT-XCT reconstruction for same mouse at three time points.

6.4 Conclusion

This chapter used the FMT-XCT imaging modality for investigation of a longitudinal lung tumor study utilizing an LLC NSCLC mouse model. Four separate sub-studies

showed four different biological findings from FMT-XCT-reconstructed fluorescence distribution to indicate tumor distribution. Initial baseline images illustrated that this NSCLC tumor was aggressive and grew rapidly. To investigate the sensitivity of fluorescence agent IntegriSense 680, one *in vivo* experiment was performed by using the integrin inhibitor cilengitide daily for around one week; after six days of treatment the FMT-XCT-reconstructed fluorescence intensity did not change greatly compared to the baseline, which demonstrated the sensitivity of the agent. Two different chemotherapies were used for this NSCLC mouse model, and both presented efficacy in treatment. Avastin therapy differed from MEK-inhibitor therapy by demonstrating efficacy later than the MEK inhibitor. In conclusion, serial imaging established that FMT-XCT can monitor tumor progression in the same mouse and, and can continuously observe the efficacy of treatments for longitudinal studies in lung cancer as well.

7 Conclusion and outlook

Preclinical imaging aims to provide a powerful tool to visualize specific molecular-level biological processes in a living body, and can find applications in many aspects of biology research. Among all molecular imaging modalities, optical imaging—especially fluorescence molecular tomography—plays an important role, because of its high sensitivity, cost-effectiveness, and multiplexing capabilities. Unfortunately, optical imaging suffers from a few disadvantages like the ill-posedness of the problem, which results from the high-scattering property of tissue. One solution to address this issue is to incorporate anatomical information (such as XCT) into a functional imaging modality. A hybrid FMT-XCT utilizes XCT structural knowledge to improve the quality and quantitative accuracy of FMT in reconstructing internal fluorescence distribution. Although FMT's depth of penetration is another problem (because of high optical absorption in tissue), this modality remains sufficient for studying small animals. Longitudinal noninvasive imaging using FMT-XCT could furnish researchers with biologically detailed insights about molecular distribution, metastasis, or disappearance. This thesis was dedicated to investigate the FMT-XCT imaging modality for various biological applications like cardiovascular and respiratory preclinical research.

Finding a suitable mathematical model that simulates light propagation in living tissue is the first step for FMT-XCT imaging. The radiative transfer equation is the most widely used model, which is difficult to solve by standard methods. In case of biological tissue, the diffusion equation can be used as an alternative to RTE. The FEM method coupled with Robin boundary conditions can be used for solving the DE (by reducing it to a linear system of equations). The preconditioned BICGSTAB method

solved this FEM-based forward model of FMT. To validate the forward-model solution using MATLAB code, two experiments with two different shapes of tissue-like home-built homogeneous silicon phantoms were performed. The code-simulated forward-model images matched perfectly with the slab-phantom-experiment image and the cylinder-phantom-experimental image, respectively. Two symmetrical source locations in physical experiments also tested the consistency of the code simulation. Results showed that the difference in the code's consistency was around 1% in the cylinder test and approximately 0.5% in the slab test.

Chapter 3 firstly explained the ill-posed inversion equation for FMT inversion, and then detailed the motivations for the hybrid FMT-XCT combination. X-ray computed tomography modality and segmentation provides structural information that can be used for FMT inversion, and can improve the accuracy and robustness of FMT quantification. To address the ill-posed FMT-XCT inversion, the iterative algorithm, LSQR, was introduced and applied to FMT-XCT quantification based on Tikhonov regularization. Regularization parameter λ was calculated by the L-curve method. The corresponding regularization matrix, or penalty matrix, was acquired by assigning different weights into the matrix for diverse organs after XCT segmentation. The hybrid FMT-XCT system was introduced, and all details were relayed about the machinery, data acquisition for both FMT and XCT modalities, and the entire data processing procedure (from raw data to reconstructed 3D-distributed fluorescence). To demonstrate XCT modality's standalone performance, one NSCLC $Kras^{G12D/+}$ mouse model was employed for individual nodule tracking with the assistance of an XCT contrast agent. An additional tissue-like phantom experiment was conducted to validate the complete FMT-XCT modality procedure. One important validation method for *in vivo* imaging—called a multispectral planer cryoslicing imaging modality—was built at our institute and employed in this study for FMT-XCT preclinical result verification.

This study then performed three separate cardiovascular and respiratory *in vivo* applications using the FMT-XCT imaging system. All three different biological diseases were in the thorax region, which contains three important organs apart from muscle: bones, the heart, and the lungs. The lungs account for largest part of this region. The first longitudinal biological study was a quantitative evaluation of asthma- related inflammation and remodeling. It integrated the FMT-XCT imaging modality and two fluorescence imaging agents: Prosense680 and MMPSense680. With DRA-challenged mice as the mouse model, three different time points or groups were chosen for imaging comparison: these are six weeks of DRA exposure, nine weeks of exposure, and nine weeks of exposure followed by three weeks of rest. Reconstruction results

from FMT-XCT for these three times showed that FMT-XCT could resolve elevated fluorescence intensity, indicating increasing inflammation-related cathepsin and MMP expression elevation. The quantification of these results was also compared against gold-standard cryoslicing results, and exhibited pronounced consistency between the *in vivo* findings and the *ex vivo* validations for studies on all sixteen mice. Statistical analysis of FMT-XCT also presented the quantification capability of the hybrid imaging system. Biological H&E staining of mice from three groups further confirmed the asthmatic inflammation and remodeling characteristics for this mouse model.

Chapter 5 focused on a deadly mouse model disease: atherosclerosis. Here the hybrid FMT-XCT system was used to visualize quantification of neutrophils, which accumulate in the plaques of an atherosclerotic aortic arch region. A commercially available fluorescence agent, Neutrophil Elastase 680 FAST, was used to track neutrophils activity at the early stages of atherosclerosis. Quantification results of FMT-XCT were compared with *ex vivo* cryoslicing findings, which also demonstrated that the hybrid system could resolve neutrophils accumulation. A new, optimized FMT-XCT reconstruction was developed in this chapter: by setting one untargeted wavelength as a background reference, the targeted wavelength reconstruction results were subtracted proportionally from this reference signal. This method removed the mutually reconstructed background that existed in every FMT-XCT inversion. An important prerequisite was that two data sets needed collection under identical conditions without any change and then deploying those exact parameters for reconstruction. Before exercising this new inversion method for biological application, a phantom test was performed by using two different wavelength agents, 680 nm and 750 nm, as a targeted and an untargeted source. The phantom experiment and the atherosclerosis mouse model test both attested that this optimized background subtraction method could improve the accuracy and quality of FMT-XCT reconstruction.

Lung cancer is also a high-mortality respiratory disease. Chapter 6 used an NSCLC mouse model, the LLC model, to demonstrate the performance of the FMT-XCT system. Four study groups were set up with distinct purposes: the first group was a baseline imaging group, with no treatment of the LLC mouse, to monitor the growth rate of this cancer model; the second group was treated with the integrin inhibitor cilengitide to test the sensitivity of IntegriSense 680; the third and fourth groups were each treated with a chemotherapy medicine separately (one with the anti-angiogenesis compound Avastin, and one with an MEK-inhibitor). Every mouse in each group was FMT-XCT-imaged at three different time points: before initial treatment, after three days of treatment, and after either six days or one week of medication.

Comparisons of each group demonstrated the same result: FMT-XCT imaging provided a useful tool for tracking tumor growth and monitoring medication therapy efficacy.

Even though these biological applications evidenced the high-quality performance of FMT-XCT quantification, a few improvements to the hybrid FMT-XCT modality await future implementation. They include the hardware and quantification inversion methods.

The studies in this thesis confirmed the basic feasibility and elucidated the performance merits of FMT-XCT in biological research. Time, however, remained a technological challenge associated with the home-built nature of the FMT-XCT system. It utilized slow scanning machinery that resulted in data acquisition times of up to 1.5 h per mouse for a three-dimensional lung reconstruction. Optimization of scanning hardware and data acquisition protocols are possible [222, 223], and would be necessary in the future to make the FMT-XCT application's throughput rate more practical. Using graphic-processing units [224, 225] and XCT contrast-enhancement techniques, such as phase contrast CT [163] or other agents, are necessary for the incorporation of XCT priors into the FMT inverse problem [85]. Finally, the establishment, here, of FMT-XCT imaging now urges multi-wavelength FMT-XCT as a next step in order to institute internal controls and to offer more precise insights into underlying biology.

Bibliography

[1]   J. Condeelis, and R. Weissleder, "In vivo imaging in cancer," *Cold Spring Harbor perspectives in biology,* vol. 2, no. 12, pp. a003848, 2010.

[2]   J. K. Willmann, N. van Bruggen, L. M. Dinkelborg, and S. S. Gambhir, "Molecular imaging in drug development," *Nature Reviews Drug Discovery,* vol. 7, no. 7, pp. 591-607, 2008.

[3]   B. Seddon, and P. Workman, "The role of functional and molecular imaging in cancer drug discovery and development," *The British journal of radiology*, 2014.

[4]   M. A. Pysz, S. S. Gambhir, and J. K. Willmann, "Molecular imaging: current status and emerging strategies," *Clinical radiology,* vol. 65, no. 7, pp. 500-516, 2010.

[5]   R. Weissleder, and M. J. Pittet, "Imaging in the era of molecular oncology," *Nature,* vol. 452, no. 7187, pp. 580-589, 2008.

[6]   V. Ntziachristos, J. Ripoll, L. V. Wang, and R. Weissleder, "Looking and listening to light: the evolution of whole-body photonic imaging," *Nature biotechnology,* vol. 23, no. 3, pp. 313-320, 2005.

[7]   S. J. Kennel, I. A. Davis, J. Branning, H. Pan, G. W. Kabalka, and M. J. Paulus, "High resolution computed tomography and MRI for monitoring lung tumor growth in mice undergoing radioimmunotherapy: correlation with histology," *Medical physics,* vol. 27, no. 5, pp. 1101-1107, 2000.

[8]   N. M. Effendy, N. I. Ibrahim, N. Mohamed, and A. N. Shuid, "An evidence-based review of micro-CT assessments of the postmenopausal osteoporosis rat model," *International Journal of Pharmacology,* vol. 11, no. 3, pp. 177-200, 2015.

[9]   J. Li, A. Chaudhary, S. J. Chmura, C. Pelizzari, T. Rajh, C. Wietholt, M. Kurtoglu, and B. Aydogan, "A novel functional CT contrast agent for molecular imaging of cancer," *Physics in medicine and biology,* vol. 55, no. 15, pp. 4389, 2010.

[10]   T. F. Massoud, and S. S. Gambhir, "Molecular imaging in living subjects: seeing fundamental biological processes in a new light," *Genes & development,* vol. 17, no. 5, pp. 545-580, 2003.

[11]   T. Hussain, and Q. T. Nguyen, "Molecular imaging for cancer diagnosis and surgery," *Advanced drug delivery reviews,* vol. 66, pp. 90-100, 2014.

[12]   M. L. James, and S. S. Gambhir, "A molecular imaging primer: modalities, imaging agents, and applications," *Physiological reviews,* vol. 92, no. 2, pp. 897-965, 2012.

[13]   M. D. Blackledge, M. O. Leach, D. J. Collins, and D.-M. Koh, "Computed diffusion-weighted MR imaging may improve tumor detection," *Radiology,* vol. 261, no. 2, pp. 573-581, 2011.

[14]   J. C. Chatham, and S. J. Blackband, "Nuclear magnetic resonance spectroscopy and imaging in animal research," *IlAR Journal,* vol. 42, no. 3, pp. 189-208, 2001.

[15]   R. Gessner, and P. A. Dayton, "Advances in molecular imaging with ultrasound," *Molecular imaging,* vol. 9, no. 3, pp. 117, 2010.

[16]   N. Deshpande, A. Needles, and J. K. Willmann, "Molecular ultrasound imaging: current status and future directions," *Clinical radiology,* vol. 65, no. 7, pp. 567-581, 2010.

[17]   I. Tardy, S. Pochon, M. Theraulaz, P. Emmel, L. Passantino, F. Tranquart, and M. Schneider, "Ultrasound molecular imaging of VEGFR2 in a rat prostate tumor model using BR55," *Investigative radiology,* vol. 45, no. 10, pp. 573-578, 2010.

[18]   T. Fischer, A. Thomas, I. Tardy, M. Schneider, H. Hünigen, P. Custodis, D. Beyersdorff, J. Plendl, J. Schnorr, and F. Diekmann, "Vascular endothelial growth factor receptor 2-specific microbubbles for molecular ultrasound detection of prostate cancer in a rat model," *Investigative radiology,* vol. 45, no. 10, pp. 675-684, 2010.

[19]   H. Liang, and M. Blomley, "The role of ultrasound in molecular imaging," *The British journal of radiology*, 2014.

[20]   M. E. Phelps, "Positron emission tomography provides molecular imaging of biological processes," *Proceedings of the National Academy of Sciences,* vol. 97, no. 16, pp. 9226-9233, 2000.

[21]   M. E. Juweid, and B. D. Cheson, "Positron-emission tomography and assessment of cancer therapy," *New England Journal of Medicine,* vol. 354, no. 5, pp. 496-507, 2006.

[22]   M. G. Pomper, and J. S. Lee, "Small animal imaging in drug development," *Current pharmaceutical design,* vol. 11, no. 25, pp. 3247-3272, 2005.

[23]   D. J. Rowland, J. S. Lewis, and M. J. Welch, "Molecular imaging: the application of small animal positron emission tomography," *Journal of Cellular Biochemistry,* vol. 87, no. S39, pp. 110-115, 2002.

[24]   V. Sossi, and T. Ruth, "Micropet imaging: in vivo biochemistry in small animals," *Journal of neural transmission,* vol. 112, no. 3, pp. 319-330, 2005.

[25]   H. R. Herschman, "Micro-PET imaging and small animal models of disease," *Current opinion in immunology,* vol. 15, no. 4, pp. 378-384, 2003.

[26]   F. J. Beekman, F. van der Have, B. Vastenhouw, A. J. van der Linden, P. P. van Rijk, J. P. H. Burbach, and M. P. Smidt, "U-SPECT-I: a novel system for submillimeter-resolution tomography with radiolabeled molecules in mice," *Journal of Nuclear Medicine,* vol. 46, no. 7, pp. 1194-1200, 2005.

[27]   M. Tian, "Molecular imaging of small animals: instrumentation and applications," *Journal of Nuclear Medicine,* vol. 56, no. 7, pp. 1130-1130, 2015.

[28]   S. Nikolaus, A. Wirrwar, C. Antke, S. Arkian, N. Schramm, H.-W. Müller, and R. Larisch, "Quantitation of dopamine transporter blockade by methylphenidate: first in vivo investigation using [123I] FP-CIT and a dedicated small animal SPECT," *European journal of nuclear medicine and molecular imaging,* vol. 32, no. 3, pp. 308-313, 2005.

[29]   E.-M. Kim, E.-H. Park, S.-J. Cheong, C.-M. Lee, D. W. Kim, H.-J. Jeong, S. T. Lim, M.-H. Sohn, K. Kim, and J. Chung, "Characterization, biodistribution and small-animal SPECT of I-125-labeled c-Met binding peptide in mice bearing c-Met receptor tyrosine kinase-positive tumor xenografts," *Nuclear medicine and biology,* vol. 36, no. 4, pp. 371-378, 2009.

[30]   Z. Liu, M. Zhao, X. Zhu, L. R. Furenlid, Y.-C. Chen, and H. H. Barrett, "In vivo dynamic imaging of myocardial cell death using 99m Tc-labeled C2A domain of synaptotagmin I in a rat model of ischemia and reperfusion," *Nuclear medicine and biology,* vol. 34, no. 8, pp. 907-915, 2007.

[31]   R. van der Meel, W. M. Gallagher, S. Oliveira, A. E. O'Connor, R. M. Schiffelers, and A. T. Byrne, "Recent advances in molecular imaging biomarkers in cancer: application of bench to bedside technologies," *Drug discovery today,* vol. 15, no. 3, pp. 102-114, 2010.

[32]   P. Blake, B. Johnson, and J. W. VanMeter, "Positron emission tomography (PET) and single photon emission computed tomography (SPECT): clinical applications," *Journal of neuro-ophthalmology,* vol. 23, no. 1, pp. 34-41, 2003.

[33]   D. W. Townsend, and S. R. Cherry, "Combining anatomy and function: the path to true image fusion," *European radiology,* vol. 11, no. 10, pp. 1968-1974, 2001.

[34]   B. H. Hasegawa, K. Iwata, K. H. Wong, M. C. Wu, A. J. Da Silva, H. R. Tang, W. C. Barber, A. H. Hwang, and A. E. Sakdinawat, "Dual-modality imaging of function and physiology," *Academic radiology,* vol. 9, no. 11, pp. 1305-1321, 2002.

[35]   S. R. Cherry, "Multimodality in vivo imaging systems: twice the power or double the trouble?," *Annu. Rev. Biomed. Eng.,* vol. 8, pp. 35-62, 2006.

[36]   G. A. Kastis, L. R. Furenlid, D. W. Wilson, T. E. Peterson, H. B. Barber, and H. H. Barrett, "Compact CT/SPECT small-animal imaging system," *Nuclear Science, IEEE Transactions on,* vol. 51, no. 1, pp. 63-67, 2004.

[37]   A. Weisenberger, R. Wojcik, E. Bradley, P. Brewer, S. Majewski, J. Qian, A. Ranck, M. Saha, K. Smith, and M. F. Smith, "SPECT-CT system for small animal imaging," *Nuclear Science, IEEE Transactions on,* vol. 50, no. 1, pp. 74-79, 2003.

[38]   R. Fontaine, F. Bélanger, J. Cadorette, J.-D. Leroux, J.-P. Martin, J.-B. Michaud, J.-F. Pratte, S. Robert, and R. Lecomte, "Architecture of a dual-modality, high-resolution, fully digital positron emission tomography/computed tomography (PET/CT) scanner for small animal imaging," *Nuclear Science, IEEE Transactions on,* vol. 52, no. 3, pp. 691-696, 2005.

[39]   C. Lasnon, A. E. Dugue, M. Briand, C. Blanc-Fournier, S. Dutoit, M.-h. Louis, and N. Aide, "NEMA NU 4-optimized reconstructions for therapy assessment in cancer research with the Inveon small animal PET/CT system," *Molecular Imaging and Biology,* vol. 17, no. 3, pp. 403-412, 2015.

[40]   C. Lasnon, E. Quak, Z. Gu, M. Briand, M.-H. Louis, and N. Aide, "Contrast-enhanced versus non-enhanced small animal PET/CT in cancer research," *Journal of Nuclear Medicine,* vol. 54, no. supplement 2, pp. 1424-1424, 2013.

[41]   S. R. Cherry, A. Y. Louie, and R. E. Jacobs, "The integration of positron emission tomography with magnetic resonance imaging," *Proceedings of the IEEE,* vol. 96, no. 3, pp. 416-438, 2008.

[42]   B. J. Pichler, H. F. Wehrl, A. Kolb, and M. S. Judenhofer, "Positron emission tomography/magnetic resonance imaging: the next generation of multimodality imaging?." pp. 199-208.

[43]   M. S. Judenhofer, H. F. Wehrl, D. F. Newport, C. Catana, S. B. Siegel, M. Becker, A. Thielscher, M. Kneilling, M. P. Lichy, and M. Eichner, "Simultaneous PET-MRI: a new approach for functional and morphological imaging," *Nature medicine,* vol. 14, no. 4, pp. 459-465, 2008.

[44]   C. Li, Y. Yang, G. S. Mitchell, and S. R. Cherry, "Simultaneous PET and multispectral 3-dimensional fluorescence optical tomography imaging system," *Journal of Nuclear Medicine,* vol. 52, no. 8, pp. 1268-1275, 2011.

[45]   J. Peter, and W. Semmler, "Performance investigation of a dual-modality SPECT/optical small animal imager." pp. S117-S117.

[46]   M. Niedre, and V. Ntziachristos, "Elucidating structure and function in vivo with hybrid fluorescence and magnetic resonance imaging," *Proceedings of the IEEE,* vol. 96, no. 3, pp. 382-396, 2008.

[47]   I.-C. Tan, C. Darne, Y. Lu, S. Yan, A. Smith, J. Rasmussen, A. Azhdarinia, and E. Sevick, "Hybrid fluorescence, PET, and CT for small animal imaging," *Journal of Nuclear Medicine,* vol. 53, no. supplement 1, pp. 493-493, 2012.

[48]   W. Koba, L. A. Jelicks, and E. J. Fine, "MicroPET/SPECT/CT imaging of small animal models of disease," *The American journal of pathology,* vol. 182, no. 2, pp. 319-324, 2013.

[49]   L. V. Wang, and S. Hu, "Photoacoustic tomography: in vivo imaging from organelles to organs," *Science,* vol. 335, no. 6075, pp. 1458-1462, 2012.

[50]   A. Taruttis, G. M. van Dam, and V. Ntziachristos, "Mesoscopic and macroscopic optoacoustic imaging of cancer," *Cancer research,* vol. 75, no. 8, pp. 1548-1559, 2015.

[51]   S. R. Cherry, "Multimodality imaging: Beyond pet/ct and spect/ct." pp. 348-353.

[52] J. C. Hebden, S. R. Arridge, and D. T. Delpy, "Optical imaging in medicine: I. Experimental techniques," *Physics in medicine and biology,* vol. 42, no. 5, pp. 825, 1997.

[53] J. R. Lorenzo, "PRINCIPLES OF DIFFUSE LIGHT PROPAGATION," 2012.

[54] B. Valeur, and M. N. Berberan-Santos, *Molecular fluorescence: principles and applications*: John Wiley & Sons, 2012.

[55] S. L. Jacques, "Optical properties of biological tissues: a review," *Physics in medicine and biology,* vol. 58, no. 11, pp. R37, 2013.

[56] R. Weissleder, "A clearer vision for in vivo imaging," *Nature biotechnology,* vol. 19, no. 4, pp. 316-317, 2001.

[57] C. H. Contag, and M. H. Bachmann, "Advances in in vivo bioluminescence imaging of gene expression," *Annual review of biomedical engineering,* vol. 4, no. 1, pp. 235-260, 2002.

[58] R. T. Sadikot, and T. S. Blackwell, "Bioluminescence imaging," *Proceedings of the American Thoracic Society,* vol. 2, no. 6, pp. 537-540, 2005.

[59] D. Huang, E. A. Swanson, C. P. Lin, J. S. Schuman, W. G. Stinson, W. Chang, M. R. Hee, T. Flotte, K. Gregory, and C. A. Puliafito, "Optical coherence tomography," *Science,* vol. 254, no. 5035, pp. 1178-1181, 1991.

[60] A. G. Podoleanu, "Optical coherence tomography," *The British journal of radiology*, 2014.

[61] R. Robertson, M. Germanos, C. Li, G. Mitchell, S. Cherry, and M. Silva, "Optical imaging of Cerenkov light generation from positron-emitting radiotracers," *Physics in medicine and biology,* vol. 54, no. 16, pp. N355, 2009.

[62] J. Rao, A. Dragulescu-Andrasi, and H. Yao, "Fluorescence imaging in vivo: recent advances," *Current opinion in biotechnology,* vol. 18, no. 1, pp. 17-25, 2007.

[63] A. Corlu, R. Choe, T. Durduran, M. A. Rosen, M. Schweiger, S. R. Arridge, M. D. Schnall, and A. G. Yodh, "Three-dimensional in vivo fluorescence diffuse optical tomography of breast cancer in humans," *Optics express,* vol. 15, no. 11, pp. 6696-6716, 2007.

[64] R. Meier, K. Thürmel, P. Moog, P. B. Noël, C. Ahari, M. Sievert, F. Dorn, S. Waldt, C. Schaeffeler, and D. Golovko, "Detection of synovitis in the hands of patients with rheumatologic disorders: diagnostic performance of optical imaging in

comparison with magnetic resonance imaging," *Arthritis & Rheumatism,* vol. 64, no. 8, pp. 2489-2498, 2012.

[65]   I. L. Medintz, H. T. Uyeda, E. R. Goldman, and H. Mattoussi, "Quantum dot bioconjugates for imaging, labelling and sensing," *Nature materials,* vol. 4, no. 6, pp. 435-446, 2005.

[66]   X. Michalet, F. Pinaud, L. Bentolila, J. Tsay, S. Doose, J. Li, G. Sundaresan, A. Wu, S. Gambhir, and S. Weiss, "Quantum dots for live cells, in vivo imaging, and diagnostics," *science,* vol. 307, no. 5709, pp. 538-544, 2005.

[67]   D. Citrin, A. K. Lee, T. Scott, M. Sproull, C. Ménard, P. J. Tofilon, and K. Camphausen, "In vivo tumor imaging in mice with near-infrared labeled endostatin," *Molecular cancer therapeutics,* vol. 3, no. 4, pp. 481-488, 2004.

[68]   M. Funovics, R. Weissleder, and C.-H. Tung, "Protease sensors for bioimaging," *Analytical and bioanalytical chemistry,* vol. 377, no. 6, pp. 956-963, 2003.

[69]   R. Weissleder, C.-H. Tung, U. Mahmood, and A. Bogdanov, "In vivo imaging of tumors with protease-activated near-infrared fluorescent probes," *Nature biotechnology,* vol. 17, no. 4, pp. 375-378, 1999.

[70]   B. Li, F. Maafi, R. Berti, P. Pouliot, E. Rhéaume, J.-C. Tardif, and F. Lesage, "Hybrid FMT-MRI applied to in vivo atherosclerosis imaging," *Biomedical optics express,* vol. 5, no. 5, pp. 1664, 2014.

[71]   V. Ntziachristos, "Fluorescence molecular imaging," *Annu Rev Biomed Eng,* vol. 8, pp. 1-33, 2006.

[72]   F. Leblond, S. C. Davis, P. A. Valdés, and B. W. Pogue, "Pre-clinical whole-body fluorescence imaging: Review of instruments, methods and applications," *Journal of photochemistry and photobiology B: Biology,* vol. 98, no. 1, pp. 77-94, 2010.

[73]   V. Ntziachristos, G. Turner, J. Dunham, S. Windsor, A. Soubret, J. Ripoll, and H. A. Shih, "Planar fluorescence imaging using normalized data," *Journal of biomedical optics,* vol. 10, no. 6, pp. 064007-064007-8, 2005.

[74]   A. Becker, C. Hessenius, K. Licha, B. Ebert, U. Sukowski, W. Semmler, B. Wiedenmann, and C. Grötzinger, "Receptor-targeted optical imaging of tumors with near-infrared fluorescent ligands," *Nature biotechnology,* vol. 19, no. 4, pp. 327-331, 2001.

[75] U. Mahmood, C.-H. Tung, A. Bogdanov Jr, and R. Weissleder, "Near-Infrared Optical Imaging of Protease Activity for Tumor Detection 1," *Radiology,* vol. 213, no. 3, pp. 866-870, 1999.

[76] K. E. Bullok, D. Maxwell, A. H. Kesarwala, S. Gammon, J. L. Prior, M. Snow, S. Stanley, and D. Piwnica-Worms, "Biochemical and in vivo characterization of a small, membrane-permeant, caspase-activatable far-red fluorescent peptide for imaging apoptosis," *Biochemistry,* vol. 46, no. 13, pp. 4055-4065, 2007.

[77] V. Ntziachristos, C.-H. Tung, C. Bremer, and R. Weissleder, "Fluorescence molecular tomography resolves protease activity in vivo," *Nature medicine,* vol. 8, no. 7, pp. 757-761, 2002.

[78] V. Ntziachristos, and R. Weissleder, "Charge-coupled-device based scanner for tomography of fluorescent near-infrared probes in turbid media," *Medical Physics,* vol. 29, no. 5, pp. 803-809, 2002.

[79] A. Koenig, L. Hervé, V. Josserand, M. Berger, J. Boutet, A. Da Silva, J.-M. Dinten, P. Peltié, J.-L. Coll, and P. Rizo, "In vivo mice lung tumor follow-up with fluorescence diffuse optical tomography," *Journal of Biomedical Optics,* vol. 13, no. 1, pp. 011008-011008-9, 2008.

[80] A. von Wallbrunn, C. Höltke, M. Zühlsdorf, W. Heindel, M. Schäfers, and C. Bremer, "In vivo imaging of integrin $\alpha v \beta 3$ expression using fluorescence-mediated tomography," *European journal of nuclear medicine and molecular imaging,* vol. 34, no. 5, pp. 745-754, 2007.

[81] V. Ntziachristos, E. A. Schellenberger, J. Ripoll, D. Yessayan, E. Graves, A. Bogdanov, L. Josephson, and R. Weissleder, "Visualization of antitumor treatment by means of fluorescence molecular tomography with an annexin V–Cy5. 5 conjugate," *Proceedings of the National Academy of Sciences of the United States of America,* vol. 101, no. 33, pp. 12294-12299, 2004.

[82] J. Haller, D. Hyde, N. Deliolanis, R. de Kleine, M. Niedre, and V. Ntziachristos, "Visualization of pulmonary inflammation using noninvasive fluorescence molecular imaging," *Journal of Applied Physiology,* vol. 104, no. 3, pp. 795-802, 2008.

[83] F. Stuker, J. Ripoll, and M. Rudin, "Fluorescence molecular tomography: principles and potential for pharmaceutical research," *Pharmaceutics,* vol. 3, no. 2, pp. 229-274, 2011.

[84] S. R. Arridge, and J. C. Schotland, "Optical tomography: forward and inverse problems," *Inverse Problems,* vol. 25, no. 12, pp. 123010, 2009.

[85]   A. Ale, V. Ermolayev, E. Herzog, C. Cohrs, M. H. de Angelis, and V. Ntziachristos, "FMT-XCT: in vivo animal studies with hybrid fluorescence molecular tomography-X-ray computed tomography," *Nature methods,* vol. 9, no. 6, pp. 615-620, 2012.

[86]   R. B. Schulz, A. Ale, A. Sarantopoulos, M. Freyer, E. Soehngen, M. Zientkowska, and V. Ntziachristos, "Hybrid system for simultaneous fluorescence and x-ray computed tomography," *Medical Imaging, IEEE Transactions on,* vol. 29, no. 2, pp. 465-473, 2010.

[87]   D. Hyde, R. de Kleine, S. A. MacLaurin, E. Miller, D. H. Brooks, T. Krucker, and V. Ntziachristos, "Hybrid FMT–CT imaging of amyloid-β plaques in a murine Alzheimer's disease model," *Neuroimage,* vol. 44, no. 4, pp. 1304-1311, 2009.

[88]   L. V. Wang, and H.-i. Wu, *Biomedical optics: principles and imaging*: John Wiley & Sons, 2012.

[89]   S. Prince, and S. Malarvizhi, "Estimation of optical properties of normal and diseased tissue based on diffuse reflectance spectral model."

[90]   B. W. Pogue, S. Geimer, T. O. McBride, S. Jiang, U. L. Österberg, and K. D. Paulsen, "Three-dimensional simulation of near-infrared diffusion in tissue: boundary condition and geometry analysis for finite-element image reconstruction," *Applied Optics,* vol. 40, no. 4, pp. 588-600, 2001.

[91]   A. Gibson, J. Hebden, and S. R. Arridge, "Recent advances in diffuse optical imaging," *Physics in medicine and biology,* vol. 50, no. 4, pp. R1, 2005.

[92]   J. Ripoll, V. Ntziachristos, R. Carminati, and M. Nieto-Vesperinas, "Kirchhoff approximation for diffusive waves," *Physical Review E,* vol. 64, no. 5, pp. 051917, 2001.

[93]   L. Wang, S. L. Jacques, and L. Zheng, "MCML—Monte Carlo modeling of light transport in multi-layered tissues," *Computer methods and programs in biomedicine,* vol. 47, no. 2, pp. 131-146, 1995.

[94]   S. Arridge, M. Schweiger, M. Hiraoka, and D. Delpy, "A finite element approach for modeling photon transport in tissue," *Medical physics,* vol. 20, no. 2, pp. 299-309, 1993.

[95]   S. S. Rao, *The finite element method in engineering*: Butterworth-heinemann, 2005.

[96]   M. R. Hestenes, and E. Stiefel, *Methods of conjugate gradients for solving linear systems*: NBS, 1952.

[97]   H. A. Van der Vorst, "Bi-CGSTAB: A fast and smoothly converging variant of Bi-CG for the solution of nonsymmetric linear systems," *SIAM Journal on scientific and Statistical Computing,* vol. 13, no. 2, pp. 631-644, 1992.

[98]   A. P, R. L, T. S, T. J, and Y. M, "3D Mesh Generation," 2011.

[99]   X. Song, D. Wang, N. Chen, J. Bai, and H. Wang, "Reconstruction for free-space fluorescence tomography using a novel hybrid adaptive finite element algorithm," *Optics Express,* vol. 15, no. 26, pp. 18300-18317, 2007.

[100]   S. I. Kabanikhin, *Inverse and ill-posed problems: theory and applications*: Walter De Gruyter, 2011.

[101]   V. Ntziachristos, and R. Weissleder, "Experimental three-dimensional fluorescence reconstruction of diffuse media by use of a normalized Born approximation," *Optics letters,* vol. 26, no. 12, pp. 893-895, 2001.

[102]   A. Soubret, J. Ripoll, and V. Ntziachristos, "Accuracy of fluorescent tomography in the presence of heterogeneities: study of the normalized Born ratio," *Medical Imaging, IEEE Transactions on,* vol. 24, no. 10, pp. 1377-1386, 2005.

[103]   C. Darne, Y. Lu, and E. M. Sevick-Muraca, "Small animal fluorescence and bioluminescence tomography: a review of approaches, algorithms and technology update," *Physics in medicine and biology,* vol. 59, no. 1, pp. R1, 2013.

[104]   A. C. Kak, and M. Slaney, *Principles of computerized tomographic imaging*: IEEE press, 1988.

[105]   R. J. Gaudette, D. H. Brooks, C. A. DiMarzio, M. E. Kilmer, E. L. Miller, T. Gaudette, and D. A. Boas, "A comparison study of linear reconstruction techniques for diffuse optical tomographic imaging of absorption coefficient," *Physics in medicine and biology,* vol. 45, no. 4, pp. 1051, 2000.

[106]   S. R. Arridge, "Optical tomography in medical imaging," *Inverse problems,* vol. 15, no. 2, pp. R41, 1999.

[107]   M. Schweiger, S. R. Arridge, and I. Nissilä, "Gauss–Newton method for image reconstruction in diffuse optical tomography," *Physics in medicine and biology,* vol. 50, no. 10, pp. 2365, 2005.

[108]   P. C. Hansen, *Rank-deficient and discrete ill-posed problems: numerical aspects of linear inversion*: Siam, 1998.

[109] G. H. Golub, M. Heath, and G. Wahba, "Generalized cross-validation as a method for choosing a good ridge parameter," *Technometrics,* vol. 21, no. 2, pp. 215-223, 1979.

[110] V. A. Morozov, "On the solution of functional equations by the method of regularization." pp. 414-417.

[111] P. C. Hansen, and D. P. O'Leary, "The use of the L-curve in the regularization of discrete ill-posed problems," *SIAM Journal on Scientific Computing,* vol. 14, no. 6, pp. 1487-1503, 1993.

[112] P. C. Hansen, "Analysis of discrete ill-posed problems by means of the L-curve," *SIAM review,* vol. 34, no. 4, pp. 561-580, 1992.

[113] M. Guven, B. Yazici, X. Intes, and B. Chance, "Diffuse optical tomography with a priori anatomical information," *Physics in Medicine and Biology,* vol. 50, no. 12, pp. 2837, 2005.

[114] S. C. Davis, H. Dehghani, J. Wang, S. Jiang, B. W. Pogue, and K. D. Paulsen, "Image-guided diffuse optical fluorescence tomography implemented with Laplacian-type regularization," *Optics express,* vol. 15, no. 7, pp. 4066-4082, 2007.

[115] D. Hyde, E. L. Miller, D. H. Brooks, and V. Ntziachristos, "Data specific spatially varying regularization for multimodal fluorescence molecular tomography," *Medical Imaging, IEEE Transactions on,* vol. 29, no. 2, pp. 365-374, 2010.

[116] K. Radrich, P. Mohajerani, J. Bussemer, M. Schwaiger, A. J. Beer, and V. Ntziachristos, "Limited-projection-angle hybrid fluorescence molecular tomography of multiple molecules," *Journal of biomedical optics,* vol. 46016, pp. 1, 2014.

[117] C. C. Paige, and M. A. Saunders, "LSQR: An algorithm for sparse linear equations and sparse least squares," *ACM Transactions on Mathematical Software (TOMS),* vol. 8, no. 1, pp. 43-71, 1982.

[118] A. B. F. Ale, "Hybrid Fluorescence Molecular Tomography and X-ray CT: Methods and Applications," München, Technische Universität München, Diss., 2012, 2012.

[119] G. Golub, and W. Kahan, "Calculating the singular values and pseudo-inverse of a matrix," *Journal of the Society for Industrial and Applied Mathematics, Series B: Numerical Analysis,* vol. 2, no. 2, pp. 205-224, 1965.

[120] G. H. Golub, and C. F. Van Loan, *Matrix computations*: JHU Press, 2012.

[121] V. Ntziachristos, A. Yodh, M. Schnall, and B. Chance, "Concurrent MRI and diffuse optical tomography of breast after indocyanine green enhancement," *Proceedings of the National Academy of Sciences,* vol. 97, no. 6, pp. 2767-2772, 2000.

[122] P. Mohajerani, "Robust Methods and Algorithms for Fluorescence Imaging and Tomography," Technische Universität München, 2014.

[123] D. Hyde, R. Schulz, D. Brooks, E. Miller, and V. Ntziachristos, "Performance dependence of hybrid x-ray computed tomography/fluorescence molecular tomography on the optical forward problem," *JOSA A,* vol. 26, no. 4, pp. 919-923, 2009.

[124] R. D. Rudyanto, G. Bastarrika, G. de Biurrun, J. Agorreta, L. M. Montuenga, C. Ortiz-de-Solorzano, and A. Muñoz-Barrutia, "Individual nodule tracking in micro-CT images of a longitudinal lung cancer mouse model," *Medical image analysis,* vol. 17, no. 8, pp. 1095-1105, 2013.

[125] Z. Chen, K. Cheng, Z. Walton, Y. Wang, H. Ebi, T. Shimamura, Y. Liu, T. Tupper, J. Ouyang, and J. Li, "A murine lung cancer co-clinical trial identifies genetic modifiers of therapeutic response," *Nature,* vol. 483, no. 7391, pp. 613-617, 2012.

[126] M. Aoyama, Q. Li, S. Katsuragawa, F. Li, S. Sone, and K. Doi, "Computerized scheme for determination of the likelihood measure of malignancy for pulmonary nodules on low-dose CT images," *Medical Physics,* vol. 30, no. 3, pp. 387-394, 2003.

[127] K. H. Barck, H. Bou-Reslan, U. Rastogi, T. Sakhuja, J. E. Long, R. Molina, A. Lima, P. Hamilton, M. R. Junttila, and L. Johnson, "Quantification of Tumor Burden in a Genetically Engineered Mouse Model of Lung Cancer by Micro-CT and Automated Analysis," *Translational oncology,* vol. 8, no. 2, pp. 126-135, 2015.

[128] L. Song, D. Coppola, S. Livingston, W. D. Cress, and E. B. Haura, "Mcl-1 regulates survival and sensitivity to diverse apoptotic stimuli in human non-small cell lung cancer cells," *Cancer biology & therapy,* vol. 4, no. 3, pp. 267-276, 2005.

[129] C. Tse, A. R. Shoemaker, J. Adickes, M. G. Anderson, J. Chen, S. Jin, E. F. Johnson, K. C. Marsh, M. J. Mitten, and P. Nimmer, "ABT-263: a potent and orally bioavailable Bcl-2 family inhibitor," *Cancer research,* vol. 68, no. 9, pp. 3421-3428, 2008.

[130] J. Leverson, H. Zhang, J. Chen, S. Tahir, D. Phillips, J. Xue, P. Nimmer, S. Jin, M. Smith, and Y. Xiao, "Potent and selective small-molecule MCL-1 inhibitors demonstrate on-target cancer cell killing activity as single agents and in combination with ABT-263 (navitoclax)," *Cell death & disease,* vol. 6, no. 1, pp. e1590, 2015.

[131] E. L. Jackson, N. Willis, K. Mercer, R. T. Bronson, D. Crowley, R. Montoya, T. Jacks, and D. A. Tuveson, "Analysis of lung tumor initiation and progression using conditional expression of oncogenic K-ras," *Genes & development,* vol. 15, no. 24, pp. 3243-3248, 2001.

[132] A. Sarantopoulos, G. Themelis, and V. Ntziachristos, "Imaging the bio-distribution of fluorescent probes using multispectral epi-illumination cryoslicing imaging," *Molecular imaging and biology,* vol. 13, no. 5, pp. 874-885, 2011.

[133] W. W. Busse, and R. F. Lemanske, Jr., "Asthma," *N Engl J Med,* vol. 344, no. 5, pp. 350-62, Feb 1, 2001.

[134] R. M. Locksley, "Asthma and allergic inflammation," *Cell,* vol. 140, no. 6, pp. 777-783, 2010.

[135] P. J. Barnes, "Immunology of asthma and chronic obstructive pulmonary disease," *Nature Reviews Immunology,* vol. 8, no. 3, pp. 183-192, 2008.

[136] J. V. Fahy, D. B. Corry, and H. A. Boushey, "Airway inflammation and remodeling in asthma," *Current opinion in pulmonary medicine,* vol. 6, no. 1, pp. 15-20, 2000.

[137] P. C. Fulkerson, C. A. Fischetti, and M. E. Rothenberg, "Eosinophils and CCR3 regulate interleukin-13 transgene-induced pulmonary remodeling," *The American journal of pathology,* vol. 169, no. 6, pp. 2117-2126, 2006.

[138] T. Zheng, Z. Zhu, Z. Wang, R. J. Homer, B. Ma, R. J. Riese Jr, H. A. Chapman Jr, S. D. Shapiro, and J. A. Elias, "Inducible targeting of IL-13 to the adult lung causes matrix metalloproteinase–and cathepsin-dependent emphysema," *Journal of Clinical Investigation,* vol. 106, no. 9, pp. 1081, 2000.

[139] H. Korideck, and J. D. Peterson, "Noninvasive quantitative tomography of the therapeutic response to dexamethasone in ovalbumin-induced murine asthma," *Journal of Pharmacology and Experimental Therapeutics,* vol. 329, no. 3, pp. 882-889, 2009.

[140] C. Bergeron, M. K. Tulic, and Q. Hamid, "Airway remodelling in asthma: from benchside to clinical practice," *Canadian respiratory journal: journal of the Canadian Thoracic Society,* vol. 17, no. 4, pp. e85, 2010.

[141] K. Górska, R. Krenke, J. Kosciuch, P. Korczynski, M. Zukowska, J. Domagala-Kulawik, M. Maskey-Warzechowska, and R. Chazan, "Relationship between airway inflammation and remodeling in patients with asthma and chronic obstructive pulmonary disease," *Eur J Med Res,* vol. 14, no. Suppl 4, pp. 90-96, 2009.

[142] V. Lagente, and E. Boichot, *Matrix metalloproteinases in tissue remodelling and inflammation*: Springer Science & Business Media, 2008.

[143] V. Lagente, B. Manoury, S. Nenan, C. Le Quement, C. Martin-Chouly, and E. Boichot, "Role of matrix metalloproteinases in the development of airway inflammation and remodeling," *Brazilian Journal of Medical and Biological Research,* vol. 38, no. 10, pp. 1521-1530, 2005.

[144] J. J. Atkinson, and R. M. Senior, "Matrix metalloproteinase-9 in lung remodeling," *Am J Respir Cell Mol Biol,* vol. 28, no. 1, pp. 12-24, Jan, 2003.

[145] A. T. Nials, and S. Uddin, "Mouse models of allergic asthma: acute and chronic allergen challenge," *Dis Model Mech,* vol. 1, no. 4-5, pp. 213-20, Nov-Dec, 2008.

[146] F. K. Swirski, D. Sajic, C. S. Robbins, B. U. Gajewska, M. Jordana, and M. R. Stampfli, "Chronic exposure to innocuous antigen in sensitized mice leads to suppressed airway eosinophilia that is reversed by granulocyte macrophage colony-stimulating factor," *J Immunol,* vol. 169, no. 7, pp. 3499-506, Oct 1, 2002.

[147] N. Goplen, M. Z. Karim, Q. Liang, M. M. Gorska, S. Rozario, L. Guo, and R. Alam, "Combined sensitization of mice to extracts of dust mite, ragweed, and Aspergillus species breaks through tolerance and establishes chronic features of asthma," *Journal of Allergy and Clinical Immunology,* vol. 123, no. 4, pp. 925-932. e11, 2009.

[148] K. Jannasch, J. Missbach-Guentner, and F. Alves, "Using in vivo imaging for asthma," *Drug Discovery Today: Disease Models,* vol. 6, no. 4, pp. 129-135, 2010.

[149] M. R. Miller, J. Hankinson, V. Brusasco, F. Burgos, R. Casaburi, A. Coates, R. Crapo, P. Enright, C. Van der Grinten, and P. Gustafsson, "Standardisation of spirometry," *Eur Respir J,* vol. 26, no. 2, pp. 319-38, 2005.

[150] A. Schneider, L. Gindner, L. Tilemann, T. Schermer, G.-J. Dinant, F. J. Meyer, and J. Szecsenyi, "Diagnostic accuracy of spirometry in primary care," *BMC pulmonary medicine,* vol. 9, no. 1, pp. 31, 2009.

[151] M. Lederlin, A. Ozier, G. Dournes, O. Ousova, P.-O. Girodet, H. Begueret, R. Marthan, M. Montaudon, F. Laurent, and P. Berger, "In vivo micro-CT assessment of airway remodeling in a flexible OVA-sensitized murine model of asthma," *PloS one,* vol. 7, no. 10, pp. e48493, 2012.

[152] S. H. Paik, W. K. Kim, J. S. Park, C. S. Park, and G. Y. Jin, "A Quantitative Study of Airway Changes on Micro-CT in a Mouse Asthma Model: Comparison With Histopathological Findings," *Allergy Asthma Immunol Res,* vol. 6, no. 1, pp. 75-82, Jan, 2014.

[153] M. Lederlin, A. Ozier, M. Montaudon, H. Begueret, O. Ousova, R. Marthan, P. Berger, and F. Laurent, "Airway remodeling in a mouse asthma model assessed by in-vivo respiratory-gated micro-computed tomography," *European radiology,* vol. 20, no. 1, pp. 128-137, 2010.

[154] X. Artaechevarria, D. Blanco, D. Perez-Martin, G. de Biurrun, L. M. Montuenga, J. P. de Torres, J. J. Zulueta, G. Bastarrika, A. Munoz-Barrutia, and C. Ortiz-de-Solorzano, "Longitudinal study of a mouse model of chronic pulmonary inflammation using breath hold gated micro-CT," *Eur Radiol,* vol. 20, no. 11, pp. 2600-8, Nov, 2010.

[155] H. Jones, P. Marino, B. Shakur, and N. Morrell, "In vivo assessment of lung inflammatory cell activity in patients with COPD and asthma," *European Respiratory Journal,* vol. 21, no. 4, pp. 567-573, 2003.

[156] S. R. Cherry, and S. S. Gambhir, "Use of positron emission tomography in animal research," *ILAR journal,* vol. 42, no. 3, pp. 219-232, 2001.

[157] V. Cortez-Retamozo, F. K. Swirski, P. Waterman, H. Yuan, J. L. Figueiredo, A. P. Newton, R. Upadhyay, C. Vinegoni, R. Kohler, and J. Blois, "Real-time assessment of inflammation and treatment response in a mouse model of allergic airway inflammation," *The Journal of clinical investigation,* vol. 118, no. 12, pp. 4058, 2008.

[158] H. Korideck, and J. D. Peterson, "Noninvasive, in vivo quantification of asthma severity using fluorescence molecular tomography," *Nature Methods| Application Notes*, 2008.

[159] R. L. Barbour, H. L. Graber, J. Chang, S.-L. S. Barbour, P. C. Koo, and R. Aronson, "MRI-guided optical tomography: prospects and computation for a new

imaging method," *Computing in Science and Engineering,* vol. 2, no. 4, pp. 63-77, 1995.

[160]   S. R. Arridge, and J. C. Hebden, "Optical imaging in medicine: II. Modelling and reconstruction," *Physics in Medicine and Biology,* vol. 42, no. 5, pp. 841, 1997.

[161]   P. Mohajerani, S. Tzoumas, A. Rosenthal, and V. Ntziachristos, "Optical and Optoacoustic Model-Based Tomography: Theory and current challenges for deep tissue imaging of optical contrast," *Signal Processing Magazine, IEEE,* vol. 32, no. 1, pp. 88-100, 2015.

[162]   Y. Lin, H. Yan, O. Nalcioglu, and G. Gulsen, "Quantitative fluorescence tomography with functional and structural a priori information," *Applied optics,* vol. 48, no. 7, pp. 1328-1336, 2009.

[163]   P. Mohajerani, A. Hipp, M. Willner, M. Marschner, M. Trajkovic-Arsic, X. Ma, N. C. Burton, U. Klemm, K. Radrich, V. Ermolayev, S. Tzoumas, J. T. Siveke, M. Bech, F. Pfeiffer, and V. Ntziachristos, "FMT-PCCT: hybrid fluorescence molecular tomography-x-ray phase-contrast CT imaging of mouse models," *IEEE Trans Med Imaging,* vol. 33, no. 7, pp. 1434-46, Jul, 2014.

[164]   B. R. Troen, "The role of cathepsin K in normal bone resorption," *Drug News Perspect,* vol. 17, no. 1, pp. 19-28, 2004.

[165]   R. J. Myerburg, A. Interian, R. M. Mitrani, K. M. Kessler, and A. Castellanos, "Frequency of sudden cardiac death and profiles of risk," *The American journal of cardiology,* vol. 80, no. 5, pp. 10F-19F, 1997.

[166]   C. J. Murray, and A. D. Lopez, "Global mortality, disability, and the contribution of risk factors: Global Burden of Disease Study," *The Lancet,* vol. 349, no. 9063, pp. 1436-1442, 1997.

[167]   A. Tuttolomondo, D. Di Raimondo, R. Pecoraro, V. Arnao, A. Pinto, and G. Licata, "Atherosclerosis as an inflammatory disease," *Current pharmaceutical design,* vol. 18, no. 28, pp. 4266-4288, 2012.

[168]   E. Galkina, and K. Ley, "Immune and inflammatory mechanisms of atherosclerosis," *Annual review of immunology,* vol. 27, pp. 165, 2009.

[169]   C. Tarin, B. Lavin, M. Gomez, M. Saura, A. Diez-Juan, and C. Zaragoza, "The extracellular matrix metalloproteinase inducer EMMPRIN is a target of nitric oxide in myocardial ischemia/reperfusion," *Free Radical Biology and Medicine,* vol. 51, no. 2, pp. 387-395, 2011.

[170] E. L. Kaijzel, P. M. van Heijningen, P. A. Wielopolski, M. Vermeij, G. A. Koning, W. A. van Cappellen, I. Que, A. Chan, J. Dijkstra, and N. W. Ramnath, "Multimodality imaging reveals a gradual increase in matrix metalloproteinase activity at aneurysmal lesions in live fibulin-4 mice," *Circulation: Cardiovascular Imaging,* vol. 3, no. 5, pp. 567-577, 2010.

[171] J.-o. Deguchi, M. Aikawa, C.-H. Tung, E. Aikawa, D.-E. Kim, V. Ntziachristos, R. Weissleder, and P. Libby, "Inflammation in Atherosclerosis Visualizing Matrix Metalloproteinase Action in Macrophages In Vivo," *Circulation,* vol. 114, no. 1, pp. 55-62, 2006.

[172] L. Rodriguez-Menocal, Y. Wei, S. M. Pham, M. St-Pierre, S. Li, K. Webster, P. Goldschmidt-Clermont, and R. I. Vazquez-Padron, "A novel mouse model of in-stent restenosis," *Atherosclerosis,* vol. 209, no. 2, pp. 359-366, 2010.

[173] M. Nahrendorf, P. Waterman, G. Thurber, K. Groves, M. Rajopadhye, P. Panizzi, B. Marinelli, E. Aikawa, M. J. Pittet, and F. K. Swirski, "Hybrid in vivo FMT-CT imaging of protease activity in atherosclerosis with customized nanosensors," *Arteriosclerosis, thrombosis, and vascular biology,* vol. 29, no. 10, pp. 1444-1451, 2009.

[174] J. Chen, C.-H. Tung, U. Mahmood, V. Ntziachristos, R. Gyurko, M. C. Fishman, P. L. Huang, and R. Weissleder, "In vivo imaging of proteolytic activity in atherosclerosis," *Circulation,* vol. 105, no. 23, pp. 2766-2771, 2002.

[175] S.-A. Lin, M. Patel, D. Suresch, B. Connolly, B. Bao, K. Groves, M. Rajopadhye, J. D. Peterson, M. Klimas, and C. Sur, "Quantitative longitudinal imaging of vascular inflammation and treatment by ezetimibe in apoE mice by FMT using new optical imaging biomarkers of cathepsin activity and integrin," *International journal of molecular imaging,* vol. 2012, 2012.

[176] M. Van Leeuwen, M. J. Gijbels, A. Duijvestijn, M. Smook, M. J. van de Gaar, P. Heeringa, M. P. de Winther, and J. W. C. Tervaert, "Accumulation of myeloperoxidase-positive neutrophils in atherosclerotic lesions in LDLR–/– mice," *Arteriosclerosis, thrombosis, and vascular biology,* vol. 28, no. 1, pp. 84-89, 2008.

[177] A. Zernecke, I. Bot, Y. Djalali-Talab, E. Shagdarsuren, K. Bidzhekov, S. Meiler, R. Krohn, A. Schober, M. Sperandio, and O. Soehnlein, "Protective role of CXC receptor 4/CXC ligand 12 unveils the importance of neutrophils in atherosclerosis," *Circulation research,* vol. 102, no. 2, pp. 209-217, 2008.

[178] M. Drechsler, R. T. Megens, M. van Zandvoort, C. Weber, and O. Soehnlein, "Hyperlipidemia-triggered neutrophilia promotes early atherosclerosis," *Circulation,* vol. 122, no. 18, pp. 1837-1845, 2010.

[179] O. Soehnlein, C. Weber, and L. Lindbom, "Neutrophil granule proteins tune monocytic cell function," *Trends in immunology,* vol. 30, no. 11, pp. 538-546, 2009.

[180] C. Nathan, "Neutrophils and immunity: challenges and opportunities," *Nature Reviews Immunology,* vol. 6, no. 3, pp. 173-182, 2006.

[181] G. S. Getz, and C. A. Reardon, "Animal models of atherosclerosis," *Arterioscler Thromb Vasc Biol,* vol. 32, no. 5, pp. 1104-15, May, 2012.

[182] V. Andrés, and B. Dorado, "Methods in Mouse Atherosclerosis."

[183] A. Ale, V. Ermolayev, N. C. Deliolanis, and V. Ntziachristos, "Fluorescence background subtraction technique for hybrid fluorescence molecular tomography/x-ray computed tomography imaging of a mouse model of early stage lung cancer," *Journal of biomedical optics,* vol. 18, no. 5, pp. 056006-056006, 2013.

[184] M. Gao, G. Lewis, G. M. Turner, A. Soubret, and V. Ntziachristos, "Effects of background fluorescence in fluorescence molecular tomography," *Applied optics,* vol. 44, no. 26, pp. 5468-5474, 2005.

[185] J. Chang, H. Graber, and R. Barbour, "Improved reconstruction algorithm for luminescence optical tomography when background lumiphore is present," *Applied optics,* vol. 37, no. 16, pp. 3547-3552, 1998.

[186] N. C. Deliolanis, T. Wurdinger, L. Pike, B. A. Tannous, X. O. Breakefield, R. Weissleder, and V. Ntziachristos, "In vivo tomographic imaging of red-shifted fluorescent proteins," *Biomedical optics express,* vol. 2, no. 4, pp. 887-900, 2011.

[187] A. Soubret, and V. Ntziachristos, "Fluorescence molecular tomography in the presence of background fluorescence," *Physics in medicine and biology,* vol. 51, no. 16, pp. 3983, 2006.

[188] R. M. Levenson, D. T. Lynch, H. Kobayashi, J. M. Backer, and M. V. Backer, "Multiplexing with multispectral imaging: from mice to microscopy," *ILAR journal,* vol. 49, no. 1, pp. 78-88, 2008.

[189] K. M. Tichauer, R. W. Holt, F. El-Ghussein, S. C. Davis, K. S. Samkoe, J. R. Gunn, F. Leblond, and B. W. Pogue, "Dual-tracer background subtraction approach

for fluorescent molecular tomography," *Journal of biomedical optics,* vol. 18, no. 1, pp. 016003-016003, 2013.

[190]   J. R. Mansfield, K. W. Gossage, C. C. Hoyt, and R. M. Levenson, "Autofluorescence removal, multiplexing, and automated analysis methods for in-vivo fluorescence imaging," *Journal of biomedical optics,* vol. 10, no. 4, pp. 041207-041207-9, 2005.

[191]   F. Liu, X. Liu, B. Zhang, and J. Bai, "Extraction of target fluorescence signal from in vivo background signal using image subtraction algorithm," *International Journal of Automation and Computing,* vol. 9, no. 3, pp. 232-236, 2012.

[192]   R. L. Siegel, K. D. Miller, and A. Jemal, "Cancer statistics, 2015," *CA: a cancer journal for clinicians,* vol. 65, no. 1, pp. 5-29, 2015.

[193]   M. Beasley, F. Thunnissen, P. S. Hasleton, M. Barbareschi, B. Pugatch, K. Geisinger, E. Brambilla, A. Gazdar, and W. Travis, "World Health Organization classification of tumours: pathology and genetics of tumours of the lung, pleura, thymus and heart," 2004.

[194]   R. Siegel, D. Naishadham, and A. Jemal, "Cancer statistics, 2012," *CA: a cancer journal for clinicians,* vol. 62, no. 1, pp. 10-29, 2012.

[195]   G. P. Kalemkerian, W. Akerley, P. Bogner, H. Borghaei, L. Q. Chow, R. J. Downey, L. Gandhi, A. K. P. Ganti, R. Govindan, and J. C. Grecula, "Small cell lung cancer," *Journal of the National Comprehensive Cancer Network,* vol. 11, no. 1, pp. 78-98, 2013.

[196]   J. P. van Meerbeeck, D. A. Fennell, and D. K. De Ruysscher, "Small-cell lung cancer," *The Lancet,* vol. 378, no. 9804, pp. 1741-1755, 2011.

[197]   E. A. Semenova, R. Nagel, and A. Berns, "Origins, genetic landscape, and emerging therapies of small cell lung cancer," *Genes Dev,* vol. 29, no. 14, pp. 1447-62, 2015.

[198]   P. Goldstraw, D. Ball, J. R. Jett, T. Le Chevalier, E. Lim, A. G. Nicholson, and F. A. Shepherd, "Non-small-cell lung cancer," *The Lancet,* vol. 378, no. 9804, pp. 1727-1740, 2011.

[199]   D. S. Ettinger, W. Akerley, G. Bepler, M. G. Blum, A. Chang, R. T. Cheney, L. R. Chirieac, T. A. D'Amico, T. L. Demmy, and A. K. P. Ganti, "Non–small cell lung cancer," *Journal of the national comprehensive cancer network,* vol. 8, no. 7, pp. 740-801, 2010.

[200]   W. D. Travis, "Pathology of lung cancer," *Clinics in chest medicine,* vol. 23, no. 1, pp. 65-81, 2002.

[201]   S. Zöchbauer-Müller, A. F. Gazdar, and J. D. Minna, "Molecular pathogenesis of lung cancer," *Annual Review of Physiology,* vol. 64, no. 1, pp. 681-708, 2002.

[202]   J. R. Molina, P. Yang, S. D. Cassivi, S. E. Schild, and A. A. Adjei, "Non-small cell lung cancer: epidemiology, risk factors, treatment, and survivorship." pp. 584-594.

[203]   R. Meuwissen, and A. Berns, "Mouse models for human lung cancer," *Genes & development,* vol. 19, no. 6, pp. 643-664, 2005.

[204]   A. Kellar, C. Egan, and D. Morris, "Preclinical Murine Models for Lung Cancer: Clinical Trial Applications," *BioMed research international,* vol. 2015, 2015.

[205]   R. Perez-Soler, "The role of erlotinib (Tarceva, OSI 774) in the treatment of non-small cell lung cancer," *Clinical cancer research,* vol. 10, no. 12, pp. 4238s-4240s, 2004.

[206]   A. Papageorgiou, P. Stravoravdi, D. Sahpazidou, K. Natsis, E. Chrysogelou, and T. Toliou, "Effect of navelbine on inhibition of tumor growth, cellular differentiation and estrogen receptor status on Lewis lung carcinoma," *Chemotherapy,* vol. 46, no. 3, pp. 188-194, 2000.

[207]   C. Scaringi, G. Minniti, P. Caporello, and R. M. Enrici, "Integrin inhibitor cilengitide for the treatment of glioblastoma: a brief overview of current clinical results," *Anticancer research,* vol. 32, no. 10, pp. 4213-4223, 2012.

[208]   T. A. Haas, and E. F. Plow, "Integrin-ligarid interactions: a year in review," *Current opinion in cell biology,* vol. 6, no. 5, pp. 656-662, 1994.

[209]   Z. Liu, F. Wang, and X. Chen, "Integrin $\alpha v \beta 3$‐targeted cancer therapy," *Drug development research,* vol. 69, no. 6, pp. 329-339, 2008.

[210]   P. A. Burke, S. J. DeNardo, L. A. Miers, K. R. Lamborn, S. Matzku, and G. L. DeNardo, "Cilengitide targeting of αvβ3 integrin receptor synergizes with radioimmunotherapy to increase efficacy and apoptosis in breast cancer xenografts," *Cancer research,* vol. 62, no. 15, pp. 4263-4272, 2002.

[211]   J. Vermorken, J. Guigay, R. Mesia, J. Trigo, U. Keilholz, A. Kerber, U. Bethe, M. Picard, and T. Brummendorf, "Phase I/II trial of cilengitide with cetuximab, cisplatin and 5-fluorouracil in recurrent and/or metastatic squamous cell cancer of the head and neck: findings of the phase I part," *British journal of cancer,* vol. 104, no. 11, pp. 1691-1696, 2011.

[212] D. A. Reardon, L. B. Nabors, R. Stupp, and T. Mikkelsen, "Cilengitide: an integrin-targeting arginine–glycine–aspartic acid peptide with promising activity for glioblastoma multiforme," *Expert opinion on investigational drugs,* vol. 17, no. 8, pp. 1225-1235, 2008.

[213] P. Leblond, S. Meignan, F. Le Tinier, U. Bethe, and A. Lansiaux, "The inhibitor of integrins Cilengitide: a new active drug in neuro-oncology," *Bulletin du cancer,* vol. 98, no. 9, pp. 1083-1090, 2011.

[214] P. Carmeliet, "VEGF as a key mediator of angiogenesis in cancer," *Oncology,* vol. 69, no. Suppl. 3, pp. 4-10, 2005.

[215] N. Ferrara, K. J. Hillan, H.-P. Gerber, and W. Novotny, "Discovery and development of bevacizumab, an anti-VEGF antibody for treating cancer," *Nature reviews Drug discovery,* vol. 3, no. 5, pp. 391-400, 2004.

[216] J. Holash, S. Wiegand, and G. Yancopoulos, "New model of tumor angiogenesis: dynamic balance between vessel regression and growth mediated by angiopoietins and VEGF," *Oncogene,* vol. 18, no. 38, 1999.

[217] N. Ferrara, "VEGF and the quest for tumour angiogenesis factors," *Nature Reviews Cancer,* vol. 2, no. 10, pp. 795-803, 2002.

[218] T. Shih, and C. Lindley, "Bevacizumab: an angiogenesis inhibitor for the treatment of solid malignancies," *Clinical therapeutics,* vol. 28, no. 11, pp. 1779-1802, 2006.

[219] B. I. Rini, "Vascular endothelial growth factor–Targeted therapy in renal cell carcinoma: current status and future directions," *Clinical Cancer Research,* vol. 13, no. 4, pp. 1098-1106, 2007.

[220] P. Roberts, and C. Der, "Targeting the Raf-MEK-ERK mitogen-activated protein kinase cascade for the treatment of cancer," *Oncogene,* vol. 26, no. 22, pp. 3291-3310, 2007.

[221] D. Wang, S. A. Boerner, J. D. Winkler, and P. M. LoRusso, "Clinical experience of MEK inhibitors in cancer therapy," *Biochimica et Biophysica Acta (BBA)-Molecular Cell Research,* vol. 1773, no. 8, pp. 1248-1255, 2007.

[222] E. E. Graves, J. P. Culver, J. Ripoll, R. Weissleder, and V. Ntziachristos, "Singular-value analysis and optimization of experimental parameters in fluorescence molecular tomography," *JOSA A,* vol. 21, no. 2, pp. 231-241, 2004.

[223] A. Jin, B. Yazici, A. Ale, and V. Ntziachristos, "Preconditioning of the fluorescence diffuse optical tomography sensing matrix based on compressive sensing," *Optics letters,* vol. 37, no. 20, pp. 4326-4328, 2012.

[224] X. Wang, B. Zhang, X. Cao, F. Liu, J. Luo, and J. Bai, "Acceleration of early-photon fluorescence molecular tomography with graphics processing units," *Computational and mathematical methods in medicine,* vol. 2013, 2013.

[225] J. Prakash, V. Chandrasekharan, V. Upendra, and P. K. Yalavarthy, "Accelerating frequency-domain diffuse optical tomographic image reconstruction using graphics processing units," *Journal of biomedical optics,* vol. 15, no. 6, pp. 066009-066009-9, 2010.

List of publications

1. **X. Ma**, J. Prakash, F. Ruscitti, S. Glasl, F. F. Stellari, G. Villetti, and V. Ntziachristos, "Assessment of asthmatic inflammation using hybrid fluorescence molecular tomography–x-ray computed tomography," *Journal of Biomedical Optics,* vol. 21, no. 1, pp. 015009-015009, 2016.

2. P. Mohajerani, A. Hipp, M. Willner, M. Marschner, M. Trajkovic-Arsic, **X. Ma**, N. C. Burton, U. Klemm, K. Radrich, V. Ermolayev, S. Tzoumas, J. T. Siveke, M. Bech, F. Pfeiffer, and V. Ntziachristos, "FMT-PCCT: hybrid fluorescence molecular tomography-x-ray phase-contrast CT imaging of mouse models," *IEEE Trans Med Imaging,* vol. 33, no. 7, pp. 1434-46, Jul, 2014.

3. M. Trajkovic-Arsic, P. Mohajerani, A. Sarantopoulos, E. Kalideris, K. Steiger, I. Esposito, **X. Ma**, G. Themelis, N. Burton, and C. W. Michalski, "Multimodal molecular imaging of integrin αvβ3 for in vivo detection of pancreatic cancer," *Journal of Nuclear Medicine,* vol. 55, no. 3, pp. 446-451, 2014.

4. M. T. Berninger, P. Mohajerani, M. Kimm, S. Masius, **X. Ma**, M. Wildgruber, B. Haller, M. Anton, A. B. Imhoff, V. Ntziachristo, and T. D. Henning, "Fluorescence Molecular Tomography of DiR-labeled mesenchymal stem cell implants for osteochondral defect repair in rabbit knees". Submitted.

5. A. Glinzer, **X. Ma**, J. Prakash, M. Kimm, F. Lohöfer, K. Kosanke, J. Pelisek, M. Thon, H. Echstein, M. Gee, V. Ntziachristos, A. Zernecke, and M. Wildgruber, "Targeting elastase for molecular imaging of early atherosclerotic lesions". Submitted.

6. M. Wildgruber, **X. Ma**, V. P. Van, M. Kimm, J. Prakash, H. Kessler, K. Kosanke, K. Radrich, M. Aichler, E. J. Rummeny, A. K. Walch, M. Eisenblätter, R. Braren, and V. Ntziachristos, "Hybrid Fluorescence Molecular Tomography/X-ray Computed Tomography for imaging of integrin expression in Non-Small Cell Lung Cancer". To be submitted.

List of Abbreviations

3D   three-dimensional

ART   algebraic reconstruction technique

BHR   Bronchial hyper-responsiveness

BICGSTAB   biconjugate gradient stabilized

BLT   bioluminescence tomography

CCD   charge coupled device

CG   conjugate gradient

CGS   conjugate gradient squared

COPD   chronic obstructive pulmonary disease

CVD   cardiovascular diseases

CW   continuous wave

DA   diffusion approximation

DE   diffusion equation

DOF	depth of field
DP	discrepancy principle
DRA	dust mites, ragweed, and aspergillus species
DW	diffusion-weighted
ECM	extracellular matrix
EM	electromagnetic
FEM	finite element method
^{18}F-FDG	fluodeoxyglucose
FMT	fluorescence molecular tomography
FPs	fluorescence proteins
FRI	fluorescence reflectance imaging
GBM	glioblastoma
GCV	generalized cross validation method
HFD	high-fat diet
HMGU	Helmholtz Zentrum München
IBMI	Biological and Medical Imaging
ICG	Indocyanine Green
LLC	Lewis lung carcinoma
LSQR	least squares QR
MAPK	Mitogen-activated protein kinase
Mcl-1	myeloid cell leukemia 1
MEK	MAPK/ERK kinase
MMPs	matrix metalloproteinases
MRI	magnetic resonance imaging

ND   neutral density

NIR   near-infrared

NSCLC   non-small cell lung cancer

OA   Optoacoustic

OCT   optical coherence tomography

O.C.T.   optimal cutting temperature medium

PBS   phosphate-buffered saline

PET   positron emission tomography

QD   Quantum Dots

RF   radio frequency

ROI   Region of Interest

RTE   radiative transfer equation

SCLC   small cell lung cancer

SNR   signal-to-noise ratio

SIRT   simultaneous iterative reconstruction technique

SPECT   single-photon emission computed tomography

US   ultrasound

VEGFR   vascular endothelial growth factor receptor

XCT   X-ray computed tomography

Acknowledgements